SEMARAK ILMU PUBLISHING

CFD Letters

Journal homepage:
https://semarakilmu.com.my/journals/index.php/CFD_Letters/index
ISSN: 2180-1363

Effect of Quarter Circle Ribs Radius and Its Location in a Suddenly Expanded Flow at Sonic Mach Number

Ambareen Khan[1], Fharukh Ahmed Ghasi Mahaboobali[2], Nur Husnina Muhamad Zuraidi[3], Sher Afghan Khan[3,*], Mohd. Azan Mohammad Sapardi[3], Khizar Ahmed Pathan[4], Javed Shoukat Shaikh[5]

[1] Centre for Instructional Technology and Multimedia, Universiti Sains Malaysia, 11700 Gelugor, Pulau Pinang, Malaysia
[2] Government Engineering College Gangavathi Koppal, Gangavathi, Karnataka 583227, India
[3] Department of Mechanical & Aerospace Engineering, Faculty of Engineering, International Islamic University Malaysia, 53100 Kuala Lumpur, Malaysia
[4] Department of Mechanical Engineering, CSMSS Chh. Shahu College of Engineering, Aurangabad, Maharashtra 431011, India
[5] Department of Mathematics, Faculty of Science and Technology, JSPM University, Pune, Maharashtra 412207, India

ARTICLE INFO

Article history:
Received 11 April 2025
Received in revised form 12 May 2025
Accepted 10 June 2025
Available online 15 July 2025

Keywords:
Sonic; shock waves; base pressure; Mach; ribs; passive control

ABSTRACT

A sudden increase in area and flow expansion is typical in the automotive and defence industries. The flow becomes divided at the base, creating low-pressure recirculation at the blunt base of the fuselage, missiles, projectiles, and aircraft bombs, which causes the base drag to increase noticeably. This paper addresses how this low base pressure at the base can be controlled. This investigation aims to maintain the separated recirculation flow via a passive control technique, such as quarter-circle ribs, where the shape varies with the variation in the rib radius. The impact of ribs on the base flow as a passive flow control mechanism on base pressure at critical Mach number is explored. Quarter-circular-shaped ribs manage the flow field into an abruptly enlarged duct from the sonic nozzle. Several variables were examined in the study, including the effects of rib orientations, rib placements, rib diameters, duct lengths, and rib locations. The ribs are arranged around the circumference of the duct. The flow from the converging nozzle at the sonic Mach number expands suddenly. Numerical research was conducted on ribs at various foundation wall positions. The area ratio is 6.25, and the rib radii considered are 1 to 5 mm, in increments of 1 mm. The NPR ranges that are simulated are 1.5 to 5. As per the results, a taller rib with a higher NPR tends to increase base pressure, while a smaller rib with a lower NPR effectively decreases base pressure. The simulation was performed on a duct with a 25 mm diameter, where the NPRs were both over- and under-expanded. Here, the ribs range in radius from 3 mm to 5 mm and have an aspect ratio of 1. They raise the NPR from 1.5 to 5 and are placed at 0.5, 1 D, 1.5 D, 2 D, and 3 D from the foundation wall. The results suggest that the position and size of the ribs may also play a considerable part in regulating the base pressure.

* *Corresponding author.*
E-mail address: sakhan@iium.edu (Sher Afghan Khan)

https://doi.org/10.37934/cfdl.18.1.87147

1. Introduction

Turbulence has been a mystery since the inception of fluid science. Since we cannot avoid turbulence in the natural and engineered flows surrounding us, we must understand it. Understanding turbulence is essential for controlling the drag associated with turbulent flows. When fluids are mixed or an increase in skin friction drag is required, there are flows where turbulence is desired. In engineering flows, however, turbulence is undesirable and should be controlled to minimize energy input. Significant financial and ecological consequences are associated with turbulent drag in engineering and real-world flows involving the use of fossil fuels through various processes.

The flow exits from a nozzle into a larger area, and due to this sudden increase in the region, the flow separates at the exit through the dividing streamline and attaches to the enlarged duct wall. The flow field of a suddenly expanded flow is shown in Figure 1(a) and 1(b). Figure 1 illustrates that the shear layer exiting the nozzle becomes separated and reattaches to the duct wall. The point at which the shear layer is reattached is known as the reattachment point, and the distance from the separation point to the reattachment point is referred to as the reattachment length. From the reattachment point again, the boundary layer will grow.

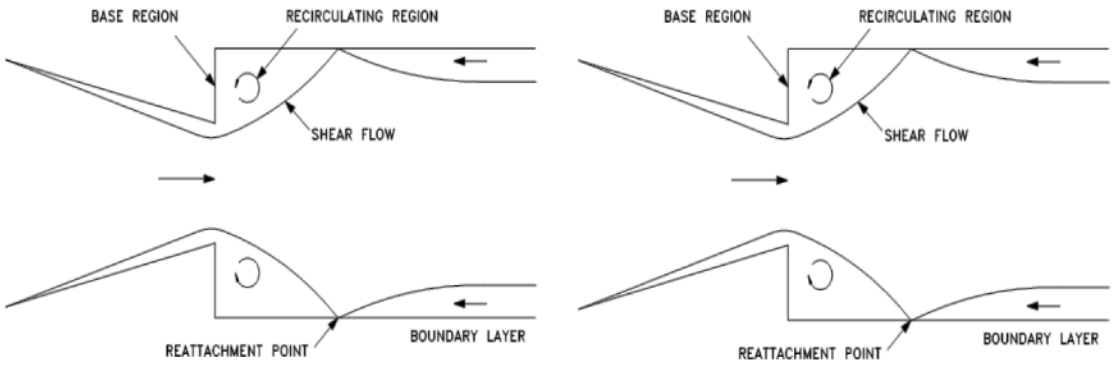

(a) (b)

Fig. 1. A view of the suddenly expanded flow field at sonic Mach number

While scanning the literature, the base drag is as high as seventy percent of the total drag. Hence, even a slight increase in the base pressure will result in a considerable decrease in base drag and an increase in the range of rockets, missiles, shells, and aircraft bombs. That will result in significant savings in fossil fuels and reduced global warming. Reducing turbulent drag will also help mitigate global warming by lowering CO2 emissions from the burning of fossil fuels. Since near-wall turbulent structures significantly contribute to drag production, efforts should be made to minimize these organized near-wall structures. Passive and active control methods are the two main categories into which the techniques used to alter these near-wall structures can be roughly separated. Although it is simple to use passive techniques like riblets, Gurney flaps, bleed, splitter plates, and super-hydrophobic surfaces, the drag reduction attained is relatively small. Conversely, a significant reduction in skin friction drag can be achieved using active control approaches. However, searching for innovative active control approaches is alluring, even if implementing active control techniques can be challenging and involves feedback loops.

Nozzle flow-accelerating devices are widely used in various industries and consumer goods, including fuel injectors, water jets, cutting machines, and paint sprays. A converging nozzle accelerates subsonic fluid flow to sonic velocities, such as those that do not exceed or equal the speed

of sound (Mach number, M ≤ 1). At the same time, CD nozzles accelerate gases to supersonic Mach numbers. They are used in rockets, missiles, and aircraft. Moreover, the shear layer can divide the base flow into two major zones. The viscous layer will form powerful vortices, which will boost the total drag force. The total drag force comprises skin friction, wave drag, and base drag. Consequently, the base pressure influences the base drag. These two parameters are inversely proportional; for example, the base drag decreases when the base pressure rises and vice versa. When the base drag of a bluff body is reduced to a desirable value, the device's efficiency also increases. Therefore, the flow control method is used to manage the flow in the duct. First is the dynamic control method, which consists of the puffing and suction methods. This method can be adjusted to switch on or off when needed, which is much more beneficial but requires additional effort and expense. Next, the passive control method consists of ribs, cavities, splitter plates, and boat tailing, among others. This study disrupts the base flow, which can be adjusted to manipulate the passive control devices.

2. Literature Review

The base pressure control in suddenly expanded flows has been extensively studied due to its direct impact on base drag reduction, constituting a significant portion of the total aerodynamic resistance in high-speed aerospace applications. Flow control strategies are broadly classified into active and passive techniques. Active control methods, such as microjets, have effectively enhanced base pressure by altering the flow field near the recirculation zone; however, they require external energy input, which complicates their implementation in real-world aerospace systems where energy efficiency is a priority [1]. While active control techniques enable on-demand flow regulation, their dependence on external energy renders them less practical for many aerospace applications. In contrast, passive control mechanisms such as splitter plates and ribs modify the aerodynamic flow without requiring additional energy, making them more viable for practical use. E. Rathakrishnan [2] demonstrated that splitter plates reduce base drag by changing the recirculation zone. Still, their effectiveness depends on placement and aspect ratio, which may not always be adaptable to various aerodynamic configurations.

E. Rathakrishnan [3,4] researched the use of ribs as passive control devices in suddenly expanded flows, demonstrating that these structures generate secondary vortices that interact with the primary flow, thereby enhancing base pressure and reducing drag. These studies form the foundational work on rib-based passive control, but they primarily consider simple rib geometries without examining the influence of corrugation. The present study builds upon these findings by introducing corrugated ribs, which further manipulate the flow structure and improve pressure recovery. Vijayaraja et al. [5] highlighted the significance of rib geometry in determining the effectiveness of passive flow control, while Sethuraman et al. [6,7] emphasized the role of rib height and placement in minimizing the recirculation zone. Although these studies provided valuable insights, they did not explore how different rib geometries affect flow oscillations and shock-boundary layer interactions. The present study extends this research by systematically analyzing how corrugated ribs influence base pressure fluctuations, offering a more comprehensive understanding of their aerodynamic impact.

Despite previous research on passive control methods, certain limitations remain unaddressed. Khan et al. [8–12] discussed various rib designs but did not quantify their effects on vortex shedding, shock standoff distance, or transient pressure fluctuations. These gaps are addressed in the current study, which conducts a detailed computational and experimental analysis of the role of corrugated ribs in regulating base pressure. CFD method has proven to be an essential tool in studying base

pressure control mechanisms [10,11]. Ambareen et al. [12,13] utilized the k-epsilon turbulence model to analyze the consequence of ribs on base pressure, confirming that CFD simulations can accurately capture the flow dynamics in suddenly expanded flows. However, their study did not focus on corrugated ribs or validate the numerical results with experimental data.

The impact of rib geometry on base pressure has also been explored through the finite volume method (FVM), as demonstrated by Ambareen et al. [14]. While this study established the capability of FVM in simulating complex flow patterns, it did not investigate the aerodynamic trade-offs associated with different rib configurations. The present research provides an intense analysis by comparing multiple rib geometries and evaluating their effects on pressure recovery, turbulence intensity, and overall aerodynamic efficiency. Beyond rib-based passive control, studies on forward-facing cavities have shown their potential to reduce drag and mitigate aerodynamic heating [15]. Heubner and Utreja [16] investigated the influence of forward-facing cavities in hypersonic flow, demonstrating that they alter shock structures and reduce aerodynamic heating. While their findings contribute to the broader field of flow control, they did not consider passive rib configurations, which could offer similar benefits without compromising structural integrity.

Lorite et al. [17] explored optimized rear cavity designs for drag reduction, revealing that cavity geometry is crucial in minimizing aerodynamic resistance. Sanmiguel [18] investigated the drag reduction produced by combining multi-cavity at the recirculation zone of a bluff body. However, their study focused on blunt-based bodies rather than forward-facing geometries or ribs, which are more relevant to the present investigation. Their findings suggest that optimizing geometric features can yield significant aerodynamic benefits, aligning with the study's objective to refine rib design for superior performance in suddenly expanded flows. Further studies by M. Kavimandan et al. [19] and Saravanan et al. [20] investigated the aerothermodynamic effects of forward-facing cavities, highlighting their potential to reduce thermal loads in high-speed aerospace applications. While their research aligns with the broader goal of enhancing aerodynamic performance, it does not directly address passive rib-based control methods.

Beyond the extensively studied passive control techniques, other innovative approaches have also been explored recently. B. Sudarshan [21] investigated the cavity's effect in the flow direction through a competing high-pressure jet combination at a Mach M = 6. S. Mohandas et al. [22] investigated wave drag reduction on blunt bodies utilizing spikes with diverse apex geometries, demonstrating that spikes effectively alter shock formation and reduce aerodynamic drag. However, their study primarily focused on external flow aerodynamics, whereas the present research examines internal flow modification through the use of corrugated ribs. Engblom et al. [23] conducted numerical studies and tests on forward-facing cavity flows at Mach numbers M> 5, providing insights into the complex flow behavior at extreme Mach numbers. While their study provided foundational knowledge on cavity-induced pressure regulation, it did not explore passive control methods, such as ribs, which can be integrated into similar aerodynamic designs.

Huang et al. [24] conducted a parametric investigation into the reduction of heat flux and base drag using forward-facing cavities on blunt bodies. Their findings emphasized that cavity geometry is crucial in controlling aerodynamic heating and pressure fluctuations. This aligns with the present study's objective of optimizing geometric configurations for drag reduction. However, while their research examined cavity-induced drag reduction, the current study investigates the impact of rib configurations on base pressure control, addressing a gap in the literature by exploring how rib-induced vortices influence the recirculation region. Finally, Santos [25] analyzed the aerothermodynamics of

rounded leading edges in hypersonic flow, accounting for real gas effects, with a focus on heat transfer and aerodynamic behavior under extreme conditions. While his work is crucial for understanding shockwave behavior and surface heating, it did not specifically address passive flow control mechanisms for drag reduction.

Khan et al. [26,27] studied the effect of the base cavity and dimple cavities on the base flows at low Mach numbers. Sajli et al. [28] numerically investigated the flow field of a non-circular cylinder at low speeds. Khan et al. [29-30] studied the effect of expansion level, as well as the favorable pressure gradient, in a suddenly expanded flow at supersonic speeds using microjets. Results show that the control in the form of tiny jets is effective when the nozzles are under-expanded. These results reiterate that whether active or passive control methods become effective depends on the nozzles flowing under the influence of a favorable pressure gradient.

However, while the review highlights the potential of flow control techniques, it does not extensively focus on the role of ribs, particularly corrugated ribs, in mitigating base drag. This limitation highlights the need for the present study, which systematically examines the impact of corrugated ribs on base pressure enhancement at Mach unity.

The current research introduces several novel aspects of base pressure regulation. Firstly, employing corrugated ribs as a passive control mechanism remains an underexplored area, with limited studies available in the literature. This work systematically investigates the impact of rib height and placement on base pressure, providing valuable insights into the optimal design of corrugated ribs for enhancing base pressure. Secondly, this study employs advanced computational fluid dynamics (CFD) techniques, including the k-epsilon model, to account for turbulence and the finite volume method (FVM) to simulate the complex flow dynamics associated with corrugated ribs. The validation of CFD results against experimental data further enhances the credibility of this research. Lastly, the study highlights the potential environmental and energy implications of base pressure control, demonstrating that corrugated ribs could contribute to the development of more energy-efficient aerospace vehicles. By addressing the shortcomings of previous studies, the present research offers significant advancements in passive control techniques for supersonic and hypersonic flow applications.

As discussed in the preceding literature review, high-speed flows that adopt active and passive regulation appear to serve multiple purposes. In earlier studies, researchers focused on wind tunnel tests. Interestingly, every item in the collection is entirely experimental, utilizing cavities, ribs, or microjets. Nevertheless, no computational research has been conducted on passive base pressure management to determine the finer points of flow phenomena that follow flow expansion using ribs. Considering this interest, ribs with varying width-to-height ratios will be employed in this paper as a passive control technique using a computational standard turbulence model. The placement and geometry of the ribs determine the base pressure. So far, researchers have not attempted to control the base pressure using a quarter-circle rib. Hence, this study aims to assess the effectiveness of passive control in the form of a quarter-circle rib with various radii at different positions for different expansion levels, to achieve the mission requirements.

3. Methodology

3.1 Governing Equations

The following hypotheses are taken into consideration:

i. Turbulent flow is considered because of the turbulent viscous dissipation effects.
ii. The fluid's viscosity varies with temperature and is compressible.

iii. At atmospheric pressure, the flow exits the duct.
iv. While scanning the literature, we found that the k-ε turbulence model is the most suitable for internal flow, as it yields reasonably good results compared to other turbulence models. Sutherland's three-coefficient viscosity model is expressed as follows:

$$\mu' = \mu'_0 \left(\frac{T_a}{T_{a,0}} \right)^{3/2} \frac{T_{a,0} + S'}{T_a + S'} \tag{1}$$

The reference viscosity value in kg/m-s is denoted as μ'o, where μ' represents the viscosity. Ta denotes static temperature; K represents the temperature of a standard reference, and S' is the temperature-dependent Sutherland constant. Three-dimensional continuity equation for compressible flow. The equation for mass balance is as follows:

$$\frac{\partial \rho}{\partial t} + \underline{\nabla} \cdot (\rho \underline{V}) = 0 \tag{2}$$

Where the fluid's velocity is denoted by V. The equation for momentum balance is:

$$\frac{\partial}{\partial t}(\rho \underline{V}) + \underline{\nabla} \cdot (\rho \underline{V}\underline{V}) + \underline{\nabla p} = \underline{\nabla} \cdot \left[2\mu (\underline{\nabla V})_0^S \right] + \underline{\nabla} \cdot (\tau_{=\mathrm{Re}}) \tag{3}$$

where $(\underline{\nabla V})_0^S = (\underline{\nabla V})^S - \frac{1}{3}(\underline{\nabla} \cdot \underline{V})\underline{I}$, $(\underline{\nabla V})^S = \frac{\underline{\nabla V} + \underline{\nabla V}^T}{2}$ and $\tau_{=\mathrm{Re}}$ is the turbulent stress tensor.

The formulae for total energy are as follows:

$$\frac{\partial}{\partial t}\left[\rho \left(\frac{1}{2} V^2 + u_{\mathrm{int}} \right) \right] + \underline{\nabla} \left[\rho \left(\frac{1}{2} V^2 + u_{\mathrm{int}} \right) \underline{V} \right] = \underline{\nabla} \left(\lambda \underline{\nabla} T - p\underline{V} + 2\mu \underline{V} \cdot (\underline{\nabla V})_0^S + \underline{V} \cdot (\tau_{=\mathrm{Re}}) \right) \tag{4}$$

where u_{int} is the internal energy and λ is the thermal conductivity.

Many internal flow simulations use the k-epsilon turbulence model due to its affordability, resilience, and sufficient accuracy. The Ansys Fluent program incorporates the k-epsilon (ε) turbulence model used in this research. The K-equation allowed us to calculate the turbulent kinetic energy.

$$\frac{\partial}{\partial t}(\rho k) + \underline{\nabla} \cdot (\rho \underline{V} k) = \underline{\nabla} \cdot \left[\left(\mu + \frac{\mu_t}{\sigma_k} \right) (\underline{\nabla} k) \right] - \rho\varepsilon + M_x \tag{5}$$

The turbulent kinetic energy dissipation rate is denoted by ε, the turbulent Prandtl number is σ-k, and the word Mx is the turbulence generation. Precisely, the dissipation (or (-equation)) is controlled by:

$$\frac{\partial(\rho\varepsilon)}{\partial t} = -\underline{\nabla} \cdot \left(\rho \varepsilon \vec{V} \right) + \underline{\nabla} \cdot \left[\left(\mu + \frac{\mu_T}{\sigma_\varepsilon} \right) \nabla \varepsilon \right] - C_1 f_1 \left(\frac{\varepsilon}{k} \right) M - C_2 f_2 \frac{\varepsilon^2}{k} \tag{6}$$

where $\mu_t = \rho f_\mu C_\mu k^2/\varepsilon$ denotes turbulent viscosity, and the arbitrary constants are denoted as $\overline{C_\mu} = 0.09$, $\overline{C_1} = 1.44$, $\overline{C_2} = 1.92$, $\overline{f_\mu} = 1$, $\sigma_k = 1.0$ and $\sigma_\varepsilon = 1.3$.

3.2 Validation of the Experimental Results

ANSYS Workbench, a computational fluid dynamics (CFD) program that uses fluid flow (or fluent) analysis systems, was utilized throughout the procedure. The model was created using a design modeler. In Figure 2, the converging nozzle abruptly grew into a five-ribbed duct. The convergent nozzle's enlarged circular duct dimensions are reported in Rathakrishnan's [1] experimental setup. The L/D ratio, which extends from 1 to 6, determines the duct length, L.

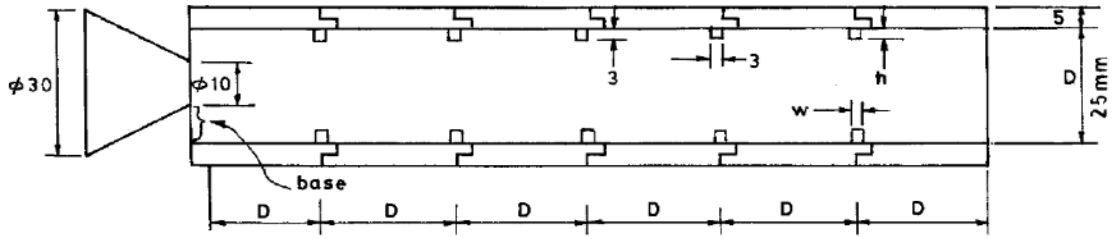

Fig. 2. A view of the duct used in the study by Rathakrishnan [1]

Table 1
The geometries of the converging nozzle model for Rathakrishnan's [1] setup

Parameters	Dimensions
Nozzle inlet diameter	30 mm
Nozzle outlet diameter	10 mm
Duct diameter	25 mm
Duct length	Varies from 1D to 6D
Converging length	20 mm
Rib width	3 mm
Rib height	Varies from 1mm to 3mm

3.3 The Boundary Condition Set

As mentioned in the first assumption, the overall setup's time was set to steady. The nozzle is axisymmetric. Density-based solvers were taken into consideration for this simulation. That is as a result of the compressible flow. The energy equation was selected for the model because the flow is compressible and contains heat transfer. Next, we have the previously mentioned third premise, which states that turbulent flow is a velocity. Consequently, the k-ε (two-equation) model was selected. Realisable was chosen for the k-epsilon model. The optimal gas was contemplated as the fluid for the materials. According to the fourth premise, fluid viscosity depends on temperature. Sutherland's law was used for the viscosity. The other characteristics, including thermal conductivity, density, and specific heat, stayed the same.

A duct with annular rectangular cavities was created when each component of the convergent-divergent axisymmetric nozzle abruptly expanded, as previously named during the geometry building process. As seen in Table 2, the zone was described according to the chosen geometry.

Table 2
The boundary conditions, zone name and geometry affected

Zone Name	Geometry Affected
Inlet	Duct inlet
Axis	X-axis
Outlet	Duct outlet
Base Wall	Base Wall
Wall	Convergent nozzle wall, duct wall
Rib	Rib wall

3.4 Validation of Previous Work

According to Rathakrishnan [1], the prior work was performed at aspect ratios of 3:3, 3:2 and 3:1; an area ratio of 6.25; L/D ranging from 1 to 6; pressure ratios of 1.141, 1.295, 1.550, 1.707 and 2.458; and nozzle exit Mach numbers of 0.44, 0.62, 0.82, 0.91 and 1.0. However, in a prior publication by Rathakrishnan [1], the result from Figure 3(b) with Nozzle Pressure Ratio (NPR) (P_{01}/P_a) 2.458 and models with control in the form of ribs with 3:2 and 3:3 aspect ratios were chosen to be compared to the current work. The simulation is supported by Rathakrishnan's [1] experimental work, which used five ribs positioned at equidistant intervals in the duct, as illustrated in Figure 3(a). The results of base pressure fluctuation with an NPR of 2.458 and L/D ranging from 2 to 6 are obtained. The study is repeated to validate the numerical results of a model with control over different rib aspect ratios.

Figure 3(a) demonstrates the current and earlier studies' base pressure ratio data curves [31]. The experimental values were denoted by dotted lines, while the simulation results obtained using ANSYS Fluent were represented by straight lines. The present numerical analysis exhibited a percentage discrepancy of less than 10% compared to the previous experimental study. Consequently, the current work met the criteria for acceptability. The curves exhibited a consistent pattern, with each point closely following the next. As a result, based on the table and graph described before, the validation of the current work was successful.

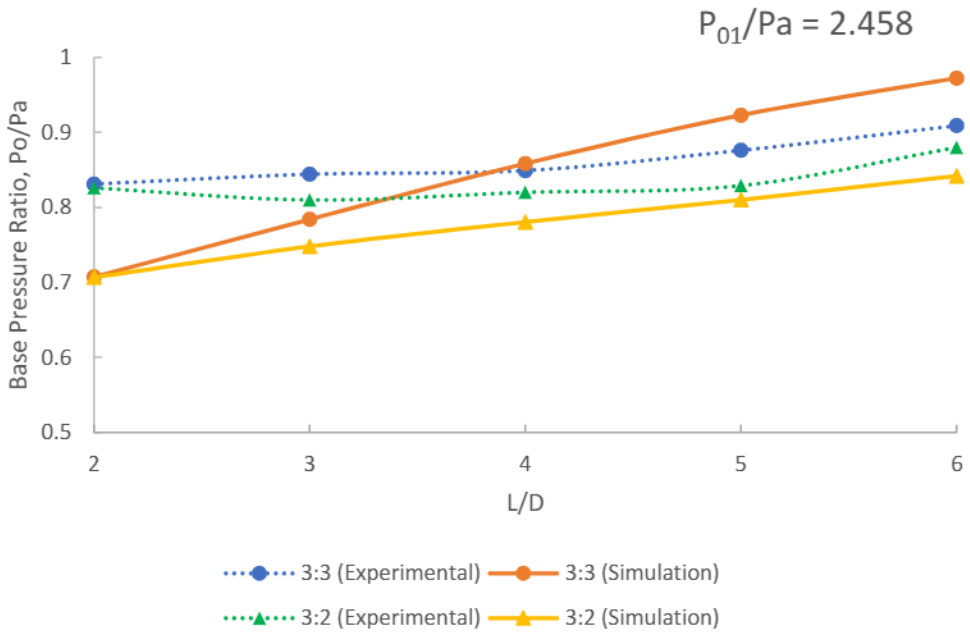

Fig. 3. (a) Validation of previous work by Rathakrishnan [31]

3.5 The Mesh Generation

3.5.1 Meshing and boundary conditions

A crucial part of the CFD process is meshing. By choosing the free-face mesh type, the 2D model is of the structured mesh type in this case. Elements were assigned sizes according to the length of each line (edge) when the constructed structured mesh type was used. The lines were utilized to apply the element size, and elements with identical forms were created using face meshing. The mesh independence check is done. Figure 3(b) below shows the mesh's element type and size tested during the mesh independence check.

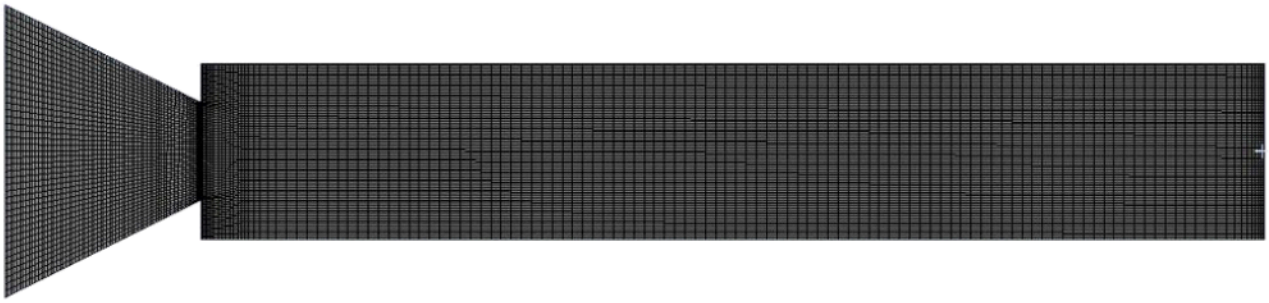

(i)

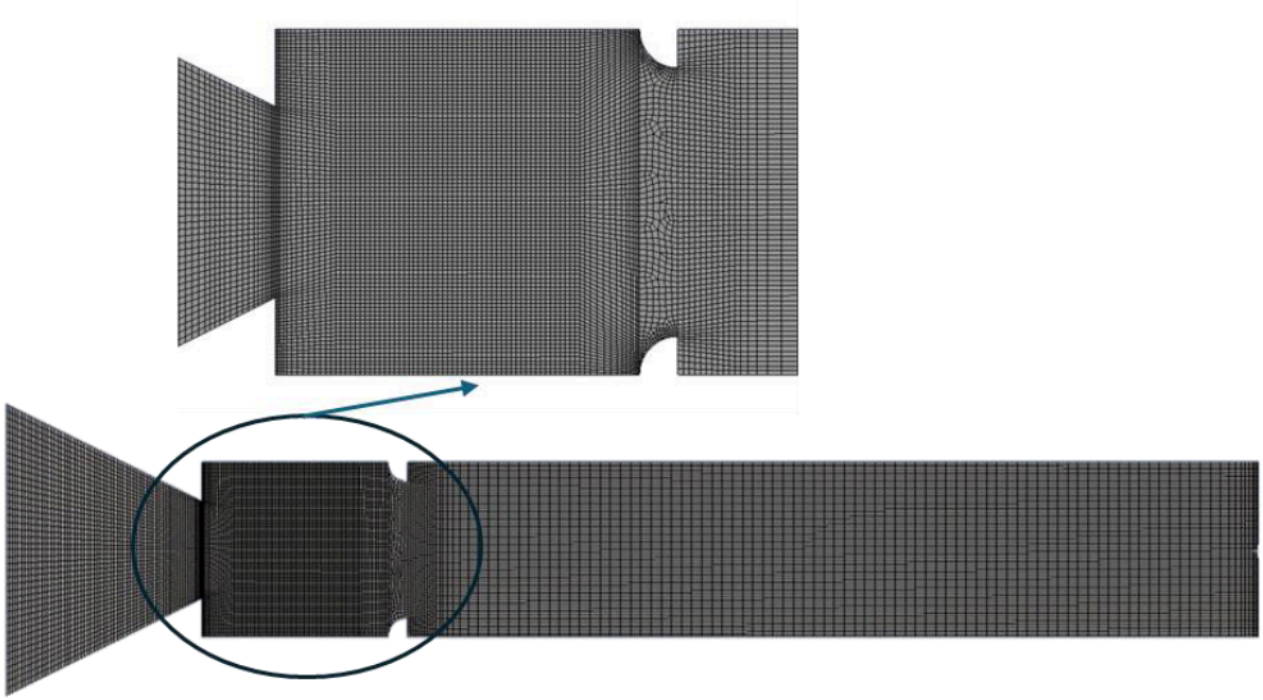

(ii)

Fig. 3. (b) Mesh model (i) Without ribs (ii) With ribs

3.6 Assumptions and Fluid Properties

Assumptions are made to replicate the flow activities in the precise physical environment. Appropriate mathematical and numerical models are selected to simplify the governing equations.

To solve the governing equations simultaneously, numerical modeling requires choosing the appropriate mathematical models, including the governing equations, boundary conditions, mesh quality, and numerical method. Despite its limitations in accurately representing physical

phenomena, the computational method has been trusted for decades and offers sufficient insight into flow behaviour. As a result, this calls for careful consideration of elements that closely resemble the flow behaviour. This study pinpoints the presumptions that jeopardize the precise physical state. The following are the presumptions and characteristics covered in this study:

i. The flow is assumed to be a steady 2D flow because the geometry is symmetric.
ii. The density of the air is variable.
iii. Since turbulent flow significantly impacts turbulent viscous dissipation at a given flow velocity, it is considered.
iv. The viscosity of the fluid is dependent on temperature.
v. At the standard atmospheric pressure, the flows leave the duct. At normal ambient pressure, the flows leave the duct.

Since the flow via the nozzle is considered turbulent, the compressible flow field is represented by the k-epsilon standard model. The subsequent equations most appropriately characterize the turbulent flow.

3.7 Mesh Independence Study

Table 3 presents data from a mesh independence study, a crucial step in computational simulations that ensures the results remain consistent regardless of the mesh refinement level. The element sizes range from the coarsest to the finest, with corresponding node and element counts for each mesh configuration. As the mesh becomes finer, the number of nodes and elements increases significantly, from 2424 nodes and 2595 elements in the coarsest mesh to 1,502,421 nodes and 1,499,178 elements in the finest mesh.

Table 3
Mesh independence study

Element size	Coarsest	Coarse	Medium 1	Medium 2	Fine	Finer	Finest
Nodes	2595	2649	8778	17046	127086	382505	1502421
Elements	2414	12464	8504	16682	126142	380868	1499178

This study aims to determine the optimal mesh size for accurate simulations without unnecessary computational expense. The table shows a notable increase in nodes and elements as the mesh is refined. The coarsest mesh has relatively few nodes and elements, resulting in a lower computational cost but potentially lower accuracy. Conversely, the finest mesh offers the highest resolution at the expense of significant computational resources. The medium and fine meshes provide intermediate levels of refinement, offering a balance between accuracy and efficiency.

Based on the trends in node and element numbers, the finest mesh is likely to produce the most accurate results (Figure 4). However, continuing to refine the mesh beyond a certain point may offer diminishing returns in terms of accuracy while significantly increasing computational time. A critical assessment of this table would suggest that the "Fine" or "Finer" mesh configurations may represent the best balance between accuracy and computational efficiency. These configurations substantially increase the number of nodes and elements compared to the medium meshes, without reaching the computational expense of the finest mesh. If the simulation results do not change significantly between the fine and finest meshes, further refinement of the finest mesh is unnecessary, as it would only increase computational time without providing any added benefit. Thus, the fine or finer mesh sizes are likely the best choices for further simulation.

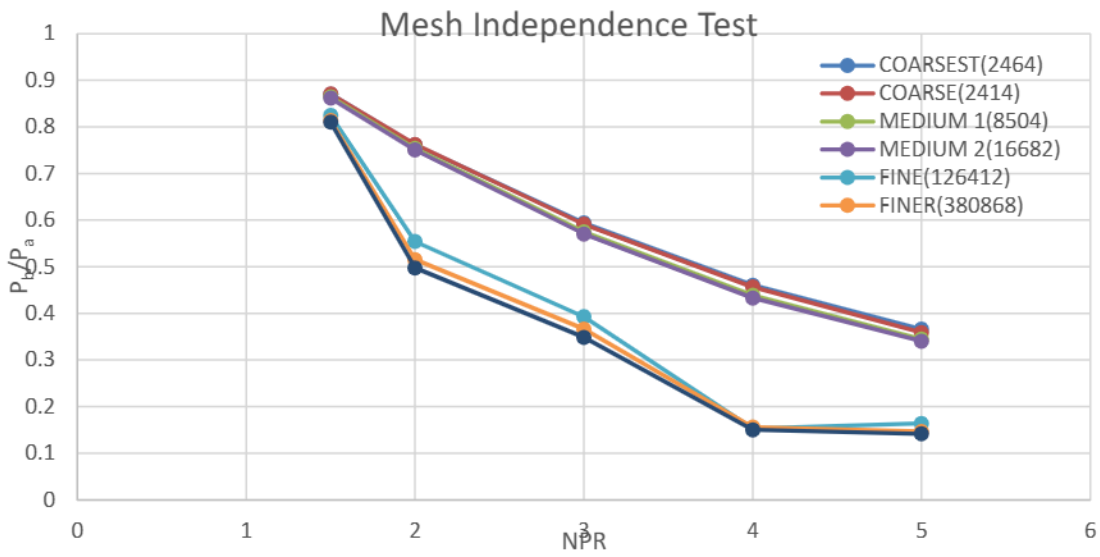

Fig. 4. Results of mesh independence check

In this work, the geometry model without control, featuring a converging nozzle with a plain duct, will serve as the reference to measure the effectiveness of passive control and flow development in detail due to the presence of ribs.

Next, a passive control is added to the duct to manipulate the flow development inside, as shown in Figures 5(a) and 5(b). At two orientations, the rib shape is changed to a quarter-circle shape.

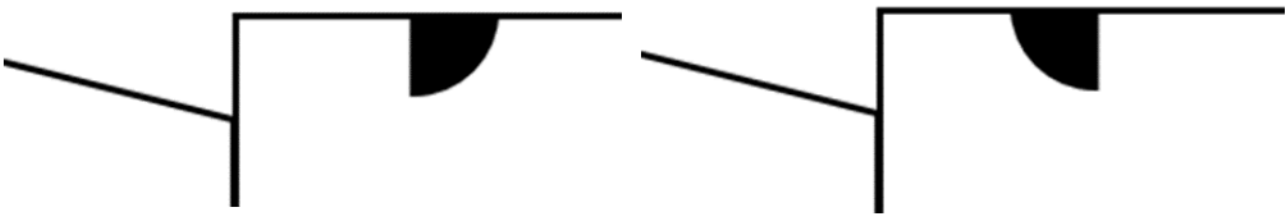

(a) (b)

Fig. 5. A view of the nozzle and duct assembly with Ribs orientation

The width-to-height ratios of the ribs are kept fixed at one, but the dimensions are varied. The rib's dimensions were:

Table 4
The rib's dimensions are based on the aspect ratio

Rib Aspect Ratio	Width (mm)	Height (mm)
1	1	1
	2	2
	3	3
	4	4
	5	5

The nozzle diameter-to-duct diameter ratio is known as the area ratio. Here is how to calculate the duct diameter:

$$Area\ ratio = \left(\frac{d_d}{d_n}\right)^2 = \left(\frac{D}{10}\right)^2 = 6.25 \quad (7)$$

In this work, the duct diameter is maintained at 25 mm. The base pressure wall altered rib placements from 0.5D to 3D. The rib positions were determined using the following Eq. (8):

Cavity Location, $CL = xD - \frac{w}{2}$ (8)

So, the rib locations are as follows:

Table 5
The locations of the rib

Rib Width (mm)	Rib Location (dimensionless)	Rib Location (mm)
1mm	0.5D	12mm
	1D	25.5mm
	1.5D	37mm
	2D	49.5mm
	3D	74.5mm
2mm	0.5D	11.5mm
	1D	25mm
	1.5D	36.5mm
	2D	49mm
	3D	74mm
3mm	0.5D	11mm
	1D	24.5mm
	1.5D	36mm
	2D	48.5mm
	3D	73.5mm
4mm	0.5D	10.5mm
	1D	24mm
	1.5D	35.5mm
	2D	48mm
	3D	73mm
5mm	0.5D	10mm
	1D	23.5mm
	1.5D	35mm
	2D	47.5mm
	3D	72.5mm

The other parameters manipulated in this project are shown in Table 6 below.

Table 6
The manipulated parameters

Nozzle Pressure Ratio (NPR)	1.5, 2, 3, 4 and 5
Duct Length (mm)	1D, 2D, 3D, 4D, 5D and 6D

To summarize, the dimensions of the current work were changed accordingly.

Table 7
The present work dimensions

Mach number	Sonic
Area Ratio	6.25
Convergent angle (θc)	26.6˚
Nozzle inlet diameter	30mm
Nozzle outlet diameter	10mm
Convergent length, lc	20mm
Duct diameter, D	25mm
Duct length, L	Varies from 25mm to 150mm

4. Results and Discussions

This research investigates the impact of quarter-circle ribs on the base flow and the subsequent development of the larger duct. When the rib's straight portion faces the base region, a nomenclature is assigned. The other side of the ribs is named orientation 2 when the base recirculation region faces the curved surface. Numerical simulations were conducted for both orientations.

During the simulations, the ribs were oriented in two different directions. The first was when the straight side of the rib was towards the base region, and the second was when the curved part faced the base recirculation zone.

In addition, the larger duct diameter of 25 mm and the noticeably high area ratio of 6.25 should be noted when analyzing the data. When the flow exits the nozzle, it expands freely. It reattaches to the enlarged duct at a location different from the ideal one for an intense vortex at the base, due to the additional relief provided to the flow. Because of this procedure, the impact of NPR on base pressure becomes negligible in large areas.

Before delving into the base pressure findings resulting from the ribs, it would be more beneficial to comprehend the flow mechanics involved in the shear layer exhaustion process in a larger duct. When Mach M < 1, the boundary layer divides and reattaches itself to the duct as it exits the tip. The divided region will have one or more vortices, since the initial vortex will be close to the base and reasonably strong. We designate the centre vortex as this vortex. This device, which functions as a pump, will move fluids from the base region to the primary jet on the edge of the shear layer. Due to this forcing action, a low-pressure zone will exist in the recirculation area. Pushing action, however, is too irregular given that this vortex spread is recognized as cyclical. This irregular pattern results in discrepancies in the base pressure. It is discovered that these changes in base pressure are negligible.

We consider mean base pressure values in our data analysis. The vortex cyclicity may cause the entire flow pattern in the enlarged image to fluctuate. Under specific geometrical and inertia conditions, these oscillations can become extremely severe. The area ratio, Mach number, reattachment length, and degree of expansion are the primary factors that affect the strength of the core vortex at the base, which fluctuates.

4.1 Base Pressure Vs. Nozzle Pressure Ratio for Rib Location 1d and Rib Orientation 1

Figure 6 shows the rib orientation 1.

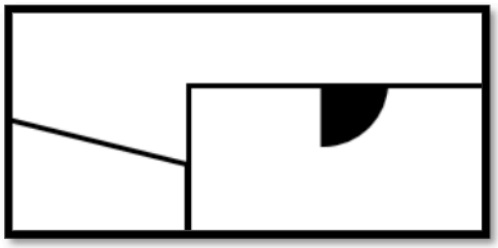

Fig. 6. Rib orientation 1

Figures 7(a) to 7(e) show base pressure results for various duct lengths and rib radius with and without control as a function of NPR. As the introductory remarks mention, the results for duct size L = 2D are presented in Figure 7(a). Despite the flow being significantly under-expanded, the falling trend persists because of the enormous area ratio in the absence of control. In these conditions, applying passive controls as a quarter-circle with a radius of 1 to 3 mm causes the base pressure to decrease up to NPR = 3 and increase to NPR greater than 3.5.

On the other hand, the base pressure rises significantly when the rib's radius is 4 or 5 mm. The highest rise in base pressure for a 5 mm radius is 40% greater than the back pressure, while the base pressure approaches the ambient pressure with a 4 mm rib radius. The surrounding pressure will influence the duct flow, and the L/D ratio is two.

The base pressure resulting from the duct length 3D is shown in Figure 7(b). The results for rib radius 4 mm and 5 mm are the same for duct length 2D. However, there is a change in the trends for lower rib radii of 1 to 3 mm due to increased duct length. A decreasing trend is reversed at NPR = 2.5, and the base pressure increases for the remaining NPRs.

The same results are seen in Figure 7(c) for L = 4D, where there are again control marks in a decline of base pressure for rib radius 1 mm and 2 mm; however, for rib radius 3 mm, control results in a growth of base pressure for NPR = 4 & above. There is no alteration in the pressure at the base region for rib radii 4 mm and 5 mm. They are identical, as observed for lower duct lengths. The changes in lower rib radii may be due to the changes in the vortex and shock wave strengths.

For a duct length of 5D, the findings of this study are presented in Figure 7(d). Once again, the results for larger rib radii are the same as those seen earlier. However, for rib radii of 1 mm and 2 mm, the control leads to a marginal increase in base pressure values, and from NPR = 2.5, a decreasing trend is observed for reaming NPRs. However, the rib radius, 3mm from NPR, shows a slight rise in base pressure from 2.5 onwards. These trends in the results are attributed to the duct's wave structure, and the atmosphere's effect is minimal.

For the duct length of 150 mm, the findings of the base pressure are displayed in Figure 7(e) for various rib radii. As shown in earlier figures, base pressure values are identical for radii 4 mm and 5 mm, except for rib radii 1mm, 2 mm, and 3 mm. For this duct length, when the rib radius is 2 mm, there is an increase in pressure from NPR = 3. From the above discussion, we may conclude that there are no definite trends in the results; hence, one needs to analyze on a case-by-case basis.

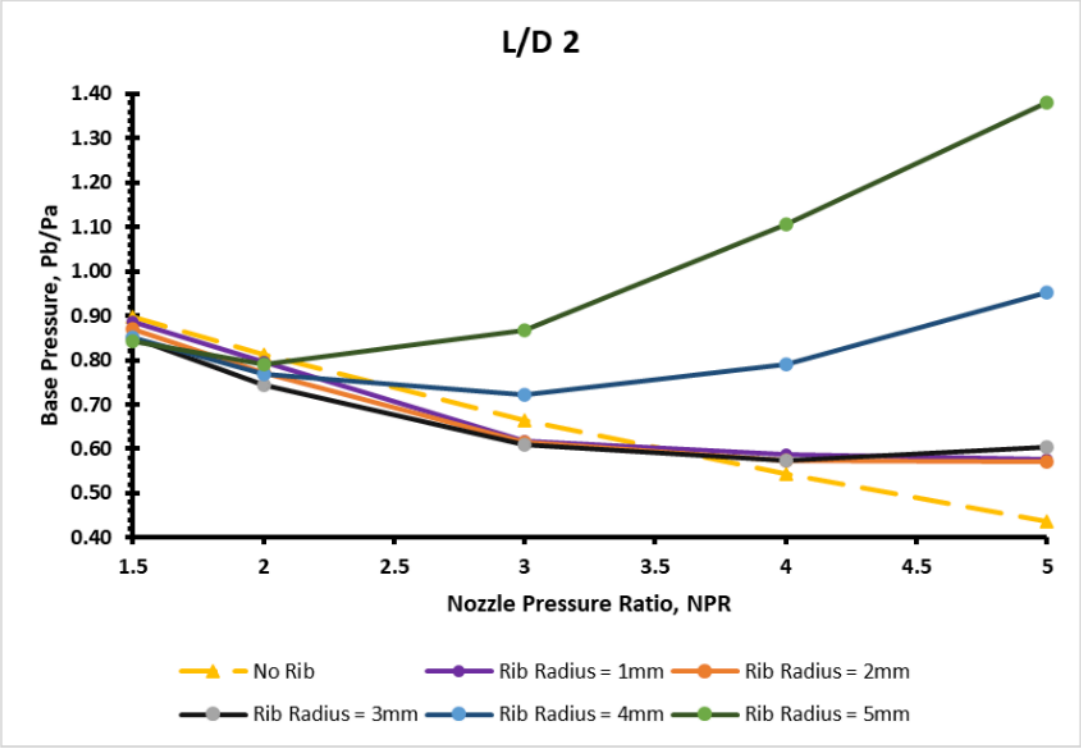
L/D 2
Base Pressure, Pb/Pa
1.40
1.30
1.20
1.10
1.00
0.90
0.80
0.70
0.60
0.50
0.40
1.5
2
2.5
3
3.5
4
4.5
5
Nozzle Pressure Ratio, NPR
No Rib
Rib Radius = 1mm
Rib Radius = 2mm
Rib Radius = 3mm
Rib Radius = 4mm
Rib Radius = 5mm

(a)

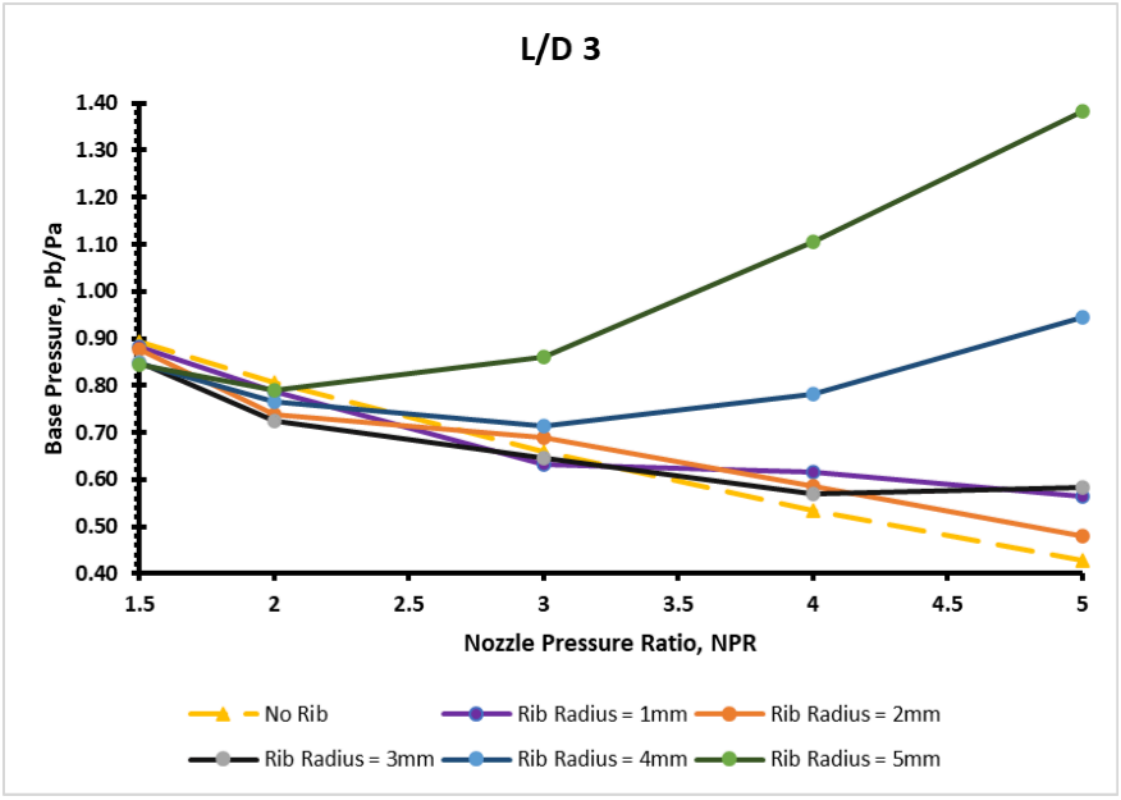
L/D 3
Base Pressure, Pb/Pa
1.40
1.30
1.20
1.10
1.00
0.90
0.80
0.70
0.60
0.50
0.40
1.5
2
2.5
3
3.5
4
4.5
5
Nozzle Pressure Ratio, NPR
No Rib
Rib Radius = 1mm
Rib Radius = 2mm
Rib Radius = 3mm
Rib Radius = 4mm
Rib Radius = 5mm

(b)

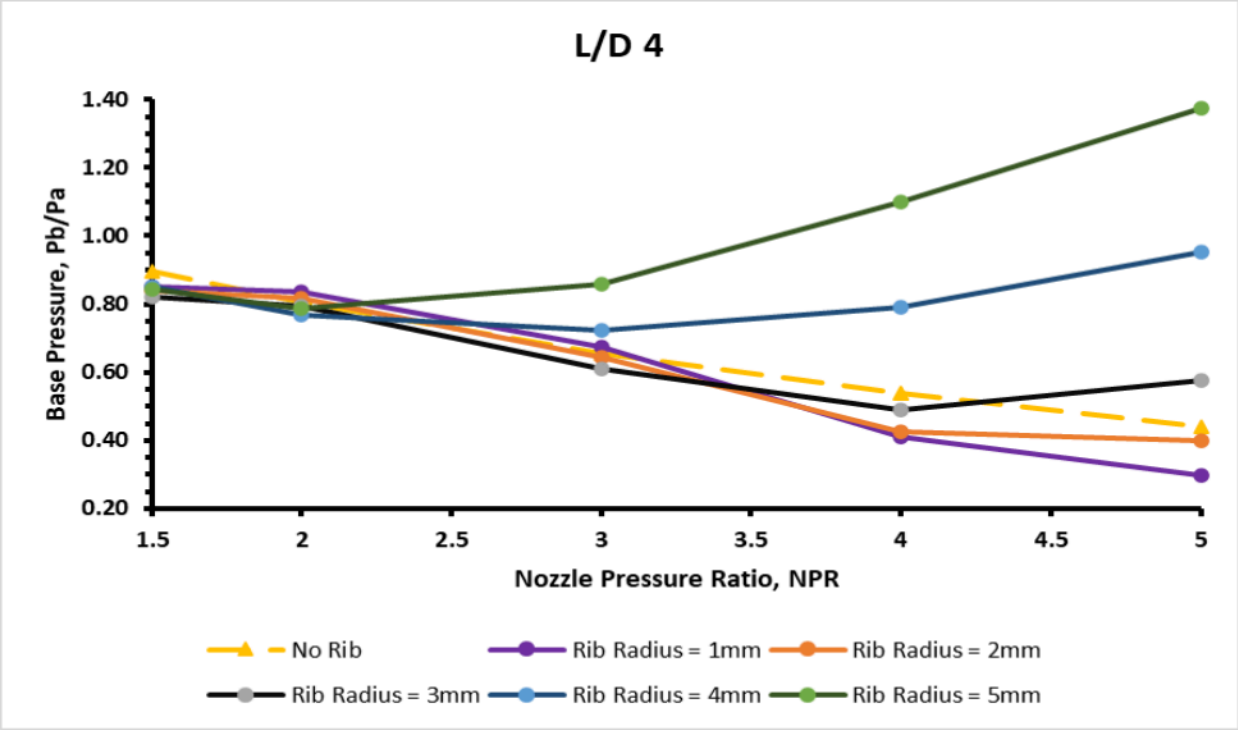
L/D 4
Base Pressure, Pb/Pa
1.40
1.20
1.00
0.80
0.60
0.40
0.20
1.5
2
2.5
3
3.5
4
4.5
5
Nozzle Pressure Ratio, NPR
No Rib
Rib Radius = 1mm
Rib Radius = 2mm
Rib Radius = 3mm
Rib Radius = 4mm
Rib Radius = 5mm

(c)

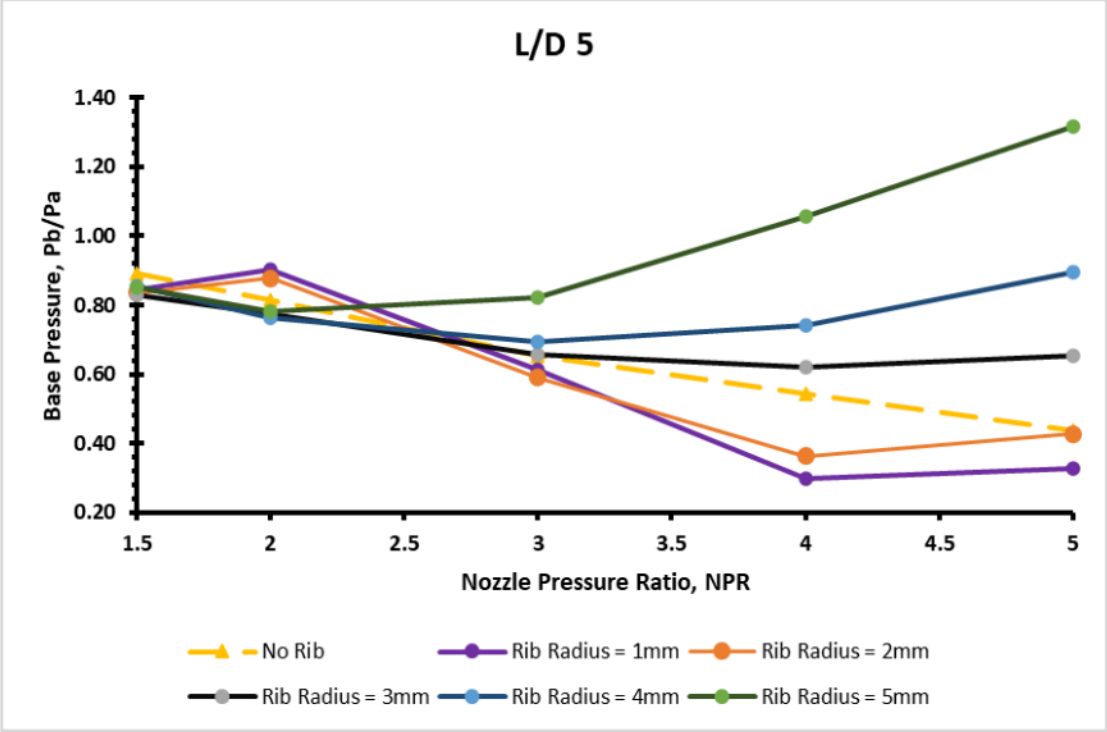
L/D 5
Base Pressure, Pb/Pa
1.40
1.20
1.00
0.80
0.60
0.40
0.20
1.5
2
2.5
3
3.5
4
4.5
5
Nozzle Pressure Ratio, NPR
No Rib
Rib Radius = 1mm
Rib Radius = 2mm
Rib Radius = 3mm
Rib Radius = 4mm
Rib Radius = 5mm

(d)

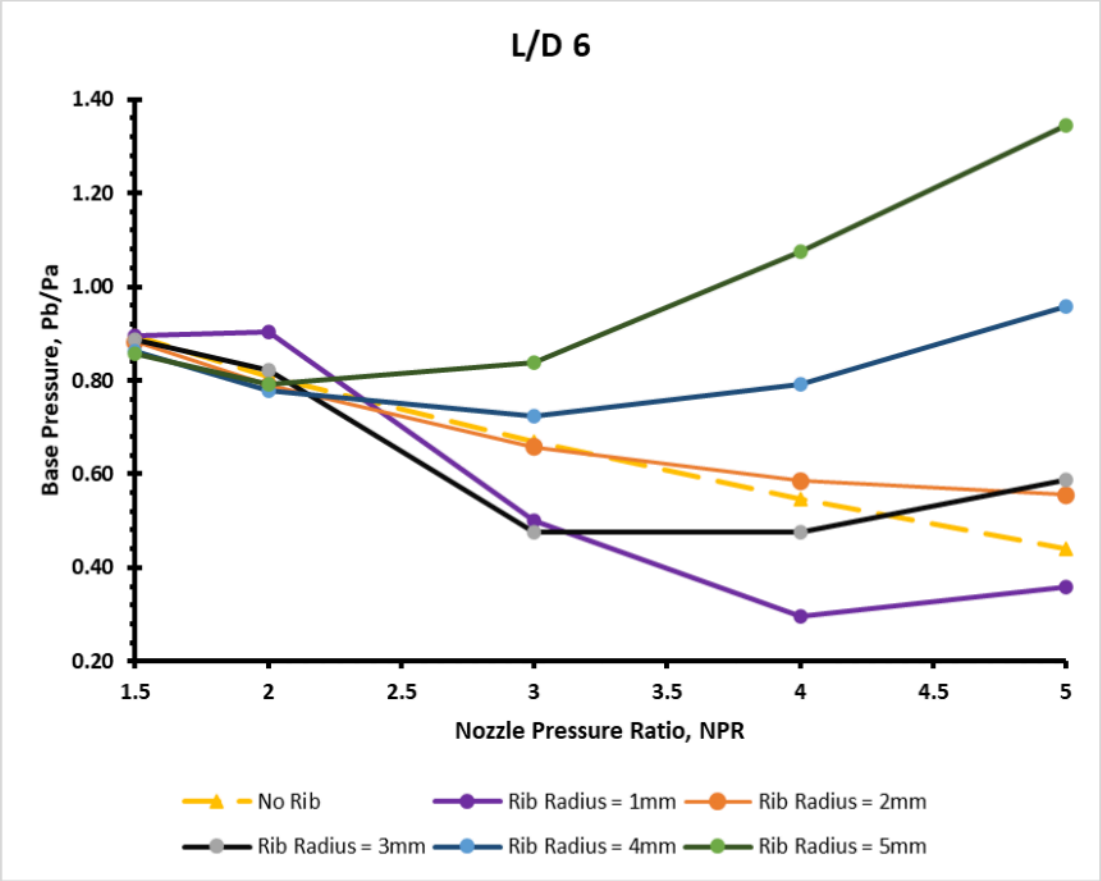

(e)

Fig. 7. Base pressure vs. NPR for various rib sizes when located at 1D

4.2 Base Pressure vs. NPR for Rib Location 1d and Rib Orientation 2

Figure 8 shows rib orientation 2.

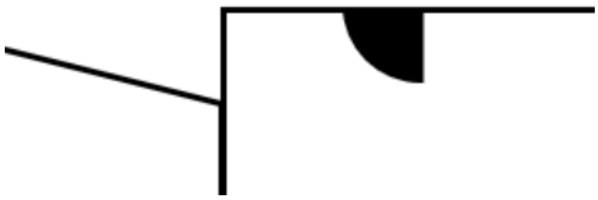

Fig. 8. Rib orientation 2

Base pressure results for rib orientation 2 for various duct lengths and rib radius as nozzle pressure ratios are exhibited in Figures 9(a) to 9(e). In orientation, the shear layer sees a curved part of the rib where the slope changes slowly. This section discusses the results of orientation 1 for various rib radii and locations.

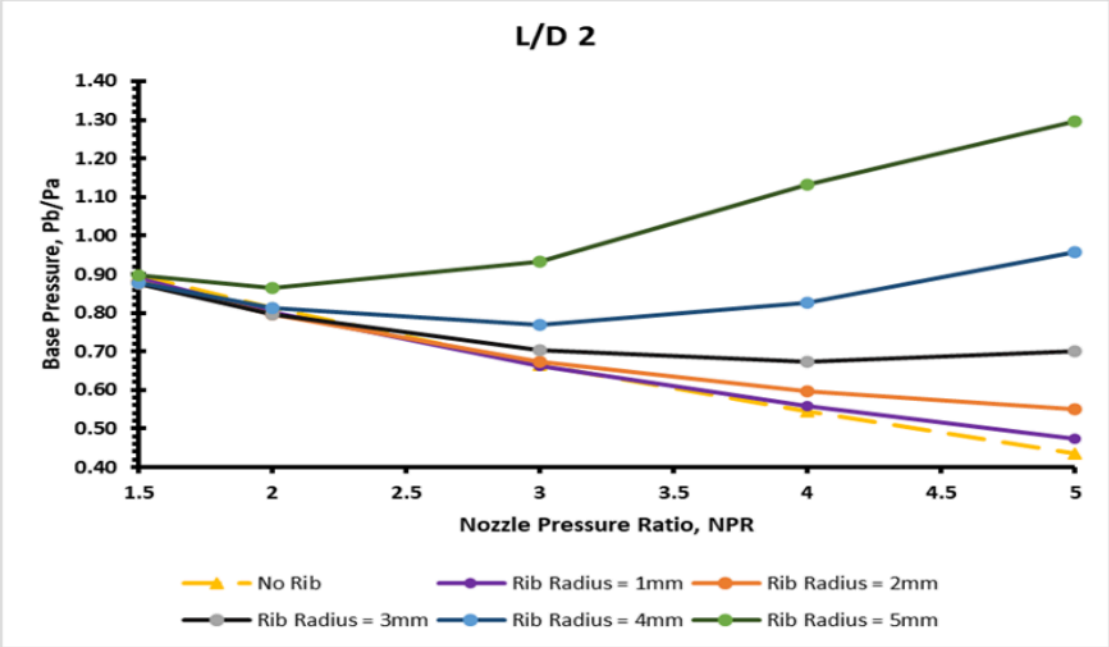
L/D 2
Base Pressure, Pb/Pa
1.40
1.30
1.20
1.10
1.00
0.90
0.80
0.70
0.60
0.50
0.40
1.5
2
2.5
3
3.5
4
4.5
5
Nozzle Pressure Ratio, NPR
No Rib
Rib Radius = 1mm
Rib Radius = 2mm
Rib Radius = 3mm
Rib Radius = 4mm
Rib Radius = 5mm

(a)

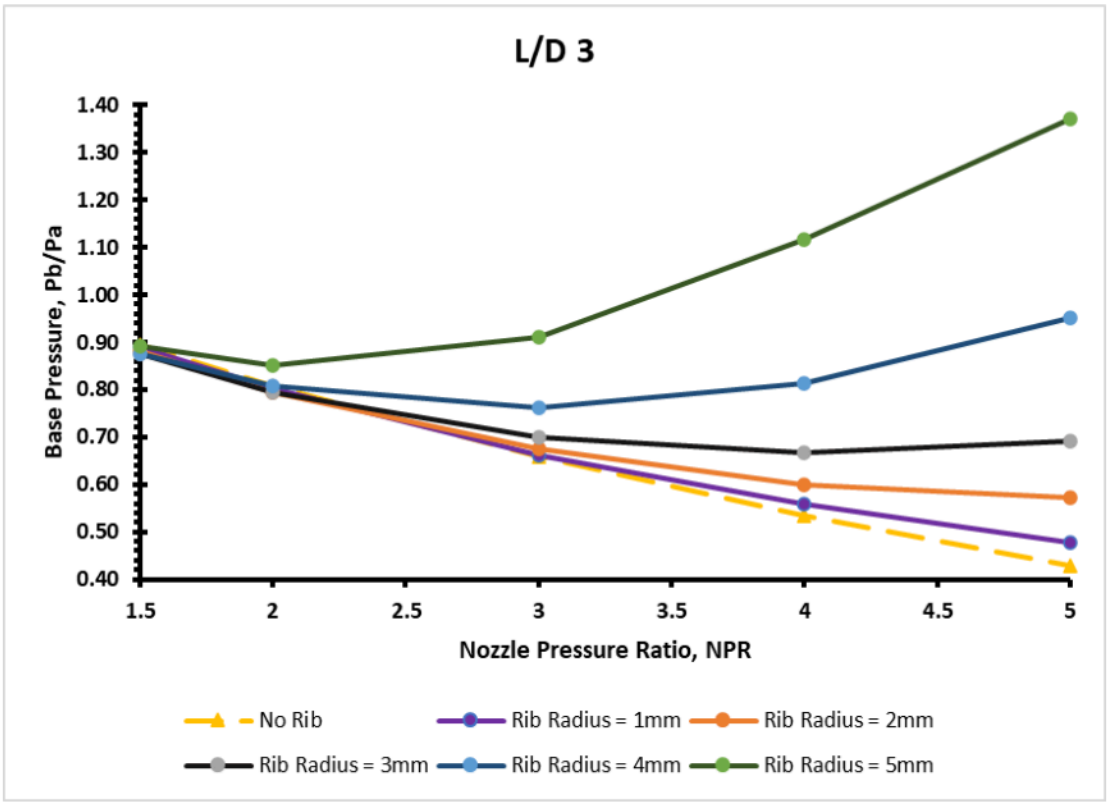
L/D 3
Base Pressure, Pb/Pa
1.40
1.30
1.20
1.10
1.00
0.90
0.80
0.70
0.60
0.50
0.40
1.5
2
2.5
3
3.5
4
4.5
5
Nozzle Pressure Ratio, NPR
No Rib
Rib Radius = 1mm
Rib Radius = 2mm
Rib Radius = 3mm
Rib Radius = 4mm
Rib Radius = 5mm

(b)

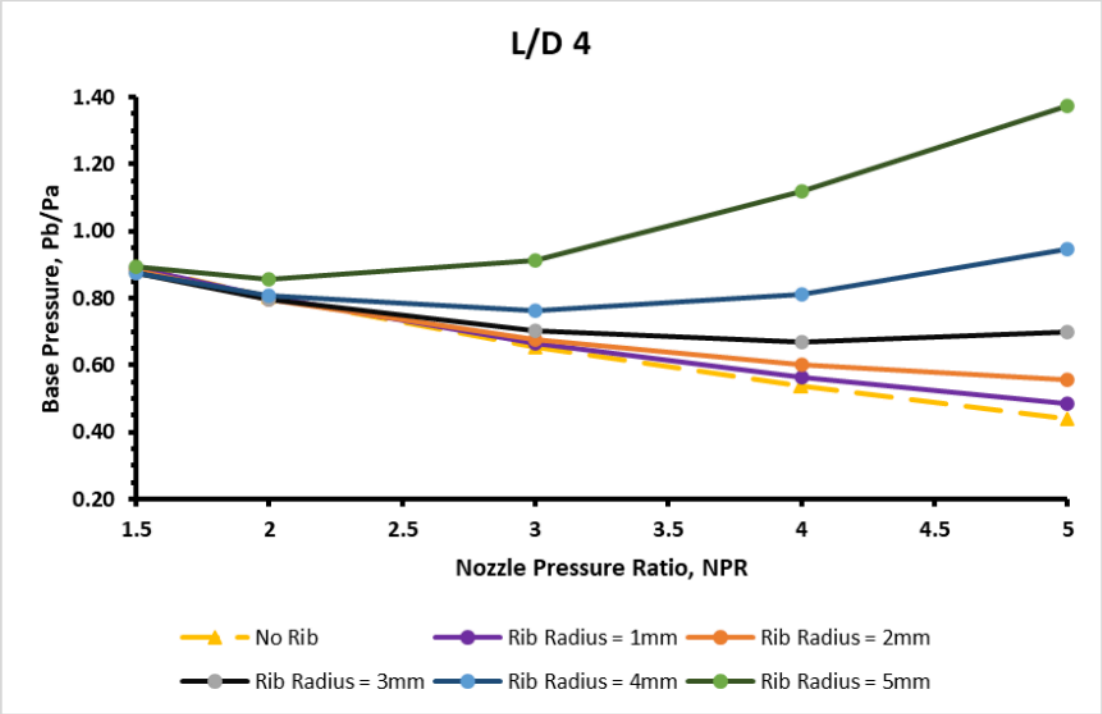
L/D 4
Base Pressure, Pb/Pa
1.40
1.20
1.00
0.80
0.60
0.40
0.20
1.5
2
2.5
3
3.5
4
4.5
5
Nozzle Pressure Ratio, NPR
No Rib
Rib Radius = 1mm
Rib Radius = 2mm
Rib Radius = 3mm
Rib Radius = 4mm
Rib Radius = 5mm

(c)

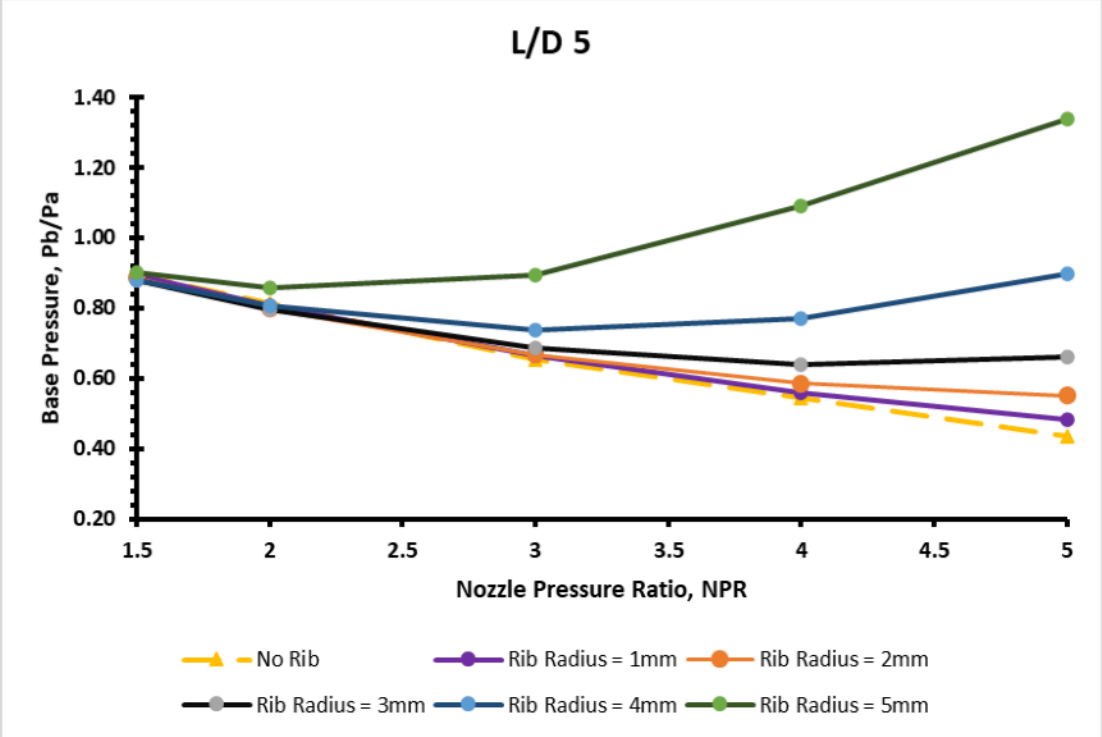
L/D 5
Base Pressure, Pb/Pa
1.40
1.20
1.00
0.80
0.60
0.40
0.20
1.5
2
2.5
3
3.5
4
4.5
5
Nozzle Pressure Ratio, NPR
No Rib
Rib Radius = 1mm
Rib Radius = 2mm
Rib Radius = 3mm
Rib Radius = 4mm
Rib Radius = 5mm

(d)

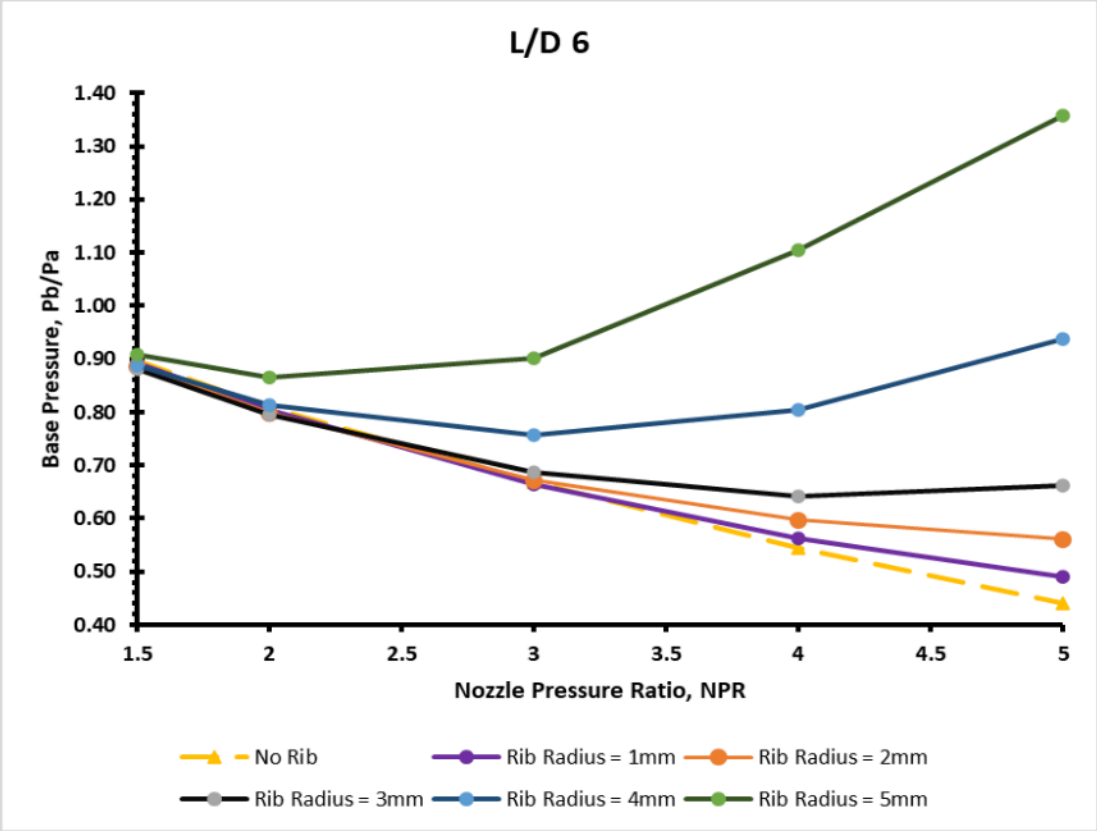

(e)

Fig. 9. Base pressure vs. NPR for various rib radii when rib location 1D

Figure 9(a) shows results for duct length 2D as a function of NPR for the same range of the rib radius. The maximum gain in base pressure for orientation one is not achieved when the viscous layer interacts with the curved surface, where the slope changes gradually, and vortex strength is also modest. These results were expected. For lower rib radius in the 1 mm to 3 mm range, the control impact is visible from NPR = 2.5, 3, and 4, respectively.

Figures 9(b) and 9(c) show similar base pressure results for alteration with NPR for numerous rib radii for duct lengths 3D, 4D, 5D, and 6D. There is no change in the results due to the smoothness of the ribs, which will result in Mach wave formation where the wave may be close to being isentropic, and this process will be limited in the vicinity of the ribs.

4.3 Base Pressure Vs. Nozzle Pressure Ratio for Rib Orientation 1 at Different Rib Size and Locations

Figure 10 shows rib orientation 1. In this section, the base pressure results are presented for orientation 1, where the flow exits the nozzle and faces the straight part of the rib. It is a quarter of a circle, where one side is straight and is given the nomenclature of orientation 1, whereas the curved part facing the flow is named orientation 2.

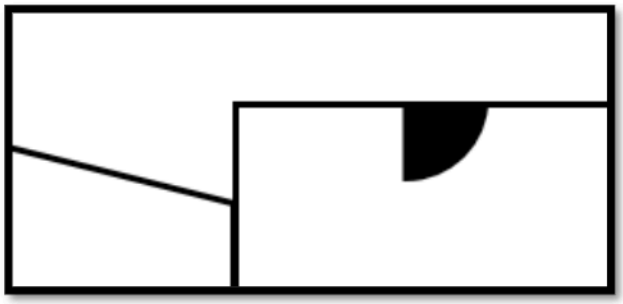

Fig. 10. Rib orientation 1

The base pressure deviation with various expansion levels for duct length 1D is illustrated in Figure 11(a) for different rib radii, ranging from 3 to 5 mm, located at 0.5D, with and without control. For this minimum duct length without control case, the base pressure behavior differs from that of the other duct sizes, and it is related to the duct size and the impact of ambient pressure. In the presence of the ribs, the decreasing behavior in the base pressure is reversed at NPRs 2, 3, and 4 for rib radii of 3, 4, and 5 mm. Another factor affecting the flow is the location of the passive control near the nozzle exit. The dividing streamline has not stabilized for this location and is trying to settle down.

Figure 11(b) shows base pressure variation with NPR for 0.5D and 1D rib positions for rib radii 3, 4, and 5 mm for a duct size of 2D. For a maximum radius of the ribs of 5 mm at locations 0.5D and 1D, the outcome shows that the base pressure is nearly equal to the ambient pressure. However, for 1D rib placement, the base pressure is 30% above atmospheric pressure. Nevertheless, when the rib radius is in the range of 3 mm to 4 mm, the findings show that for the 1D position of the rib, the normalized base pressure values are equal to ambient pressure and 20% less than ambient pressure.

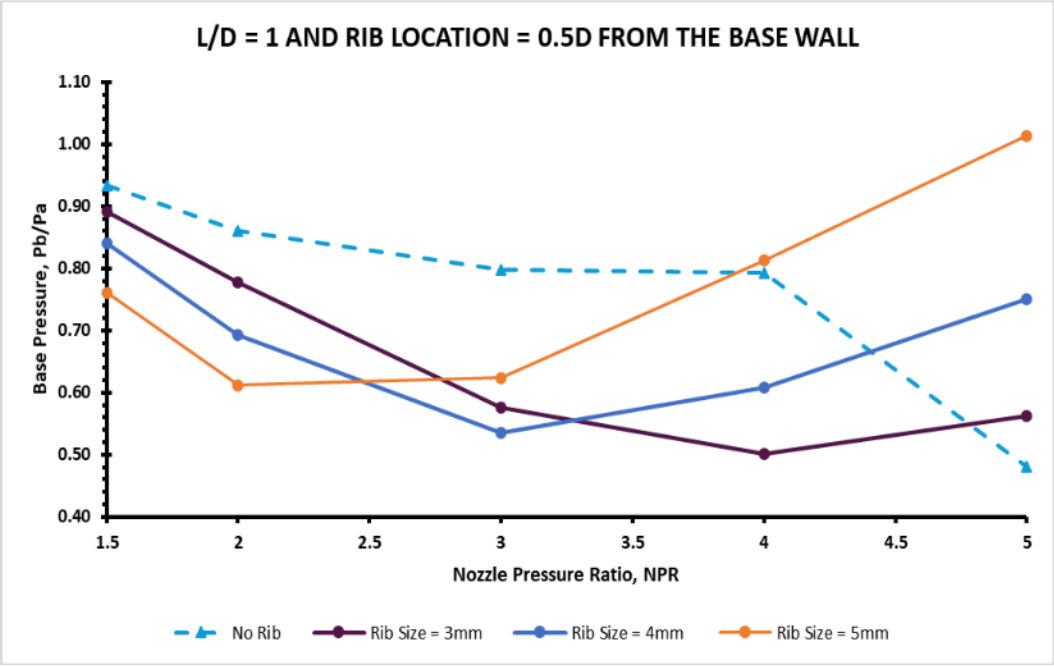

(a)

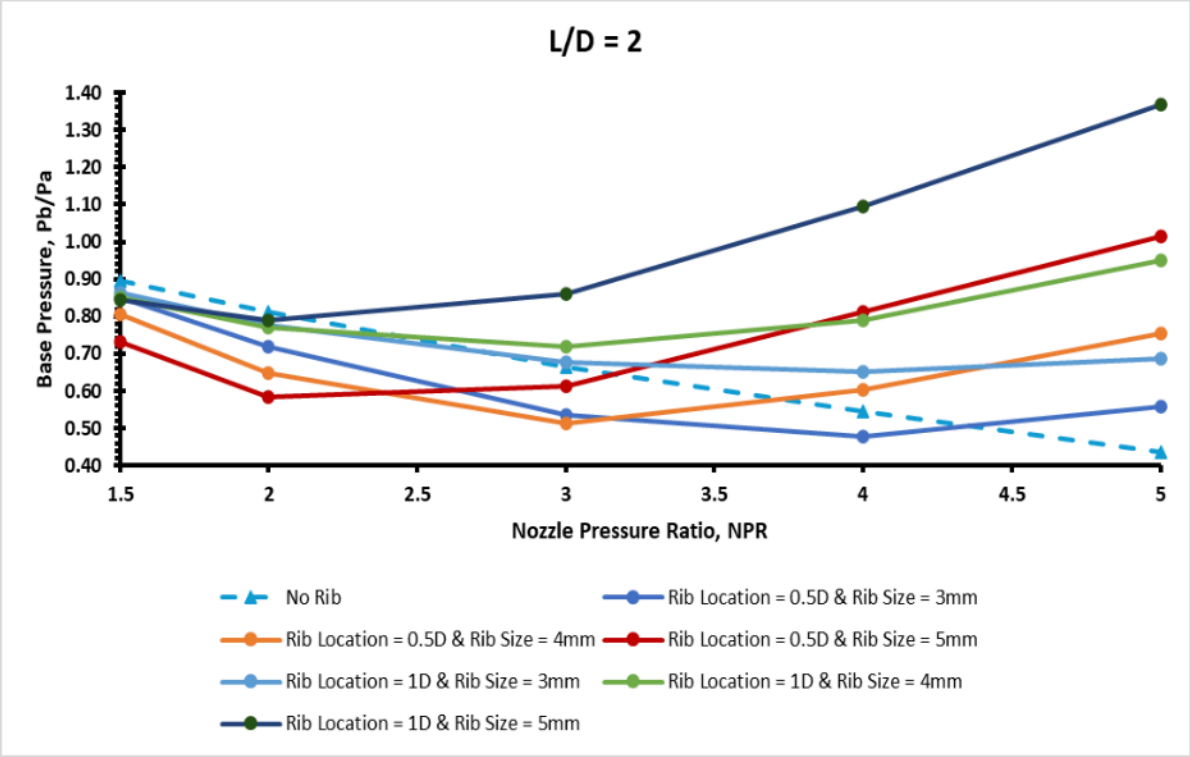

(b)

Fig. 11. Base pressure vs. NPR for various rib sizes and locations for L = 2D

However, for the 0.5D rib location, these values are 20% and 40% less than the freestream pressure. It is observed that the effectiveness of the ribs' control increases as they are placed farther away from the base recirculation region. Still, we cannot derive any convincing conclusions as the duct length is too short, and ambient pressure will play a significant role.

Base Pressure results for a 3 mm radius rib placed at 0.5D to 2D for duct length L = 3D are described in Figure 12(a). It is established that once the rib is placed at 0.5D, which is very close to the base region, the base pressure decreases up to NPR = 4. Afterward, there is a reversal in the trend, followed by a 20% increase in the base pressure. When the rib is located at 1D, the decreasing trend reverses at NPR = 2.5, but further development occurs in the NPR, where Pe/Pa < 1. There is no substantial increase in the base pressure. Likewise, when the ribs were located at 1.5D and 2D, the reduction in the base pressure was marginal. Here is a growth in the base pressure from NPR = 3 and above. This trend is associated with the rib location; at the 0.5D location, they are entirely different and the physics for this trend is that at this location, the viscous layer is just leaving the nozzle and getting divided between the primary jet flow and the separated region, at the same time there is a rib which generates weak waves and vortices and interacts with the strong vortex at the base corner of the recirculation zone. This interaction is so excessive that it decreases the base pressure, but control results in a marginal rise in the base pressure for highly under-expanded nozzle flow. For the other three rib locations, declining trends in the base pressure are reduced considerably.

Base Pressure results for a 4 mm radius rib placed at 0.5D to 2D for a duct size of L = 3D are displayed in Figure 12(b). In this case, all the variables are the same, except there is an increase in the rib radius, and the impact of an increase in the rib radius is visible from the figure. For the 0.5D rib location, the reversal in the decrease occurs at NPR = 3 instead of 4, and the base pressure level has also changed for a rib radius of 4 mm. It is up by 40% instead of 20%, which is essentially double. Similar results are seen for other locations of the ribs. For 1.5D and 2D rib locations at NPR = 5, the

base pressure is 20% higher than the ambient pressure. All these changes are caused by an increased rib radius, which interacts with the base flows.

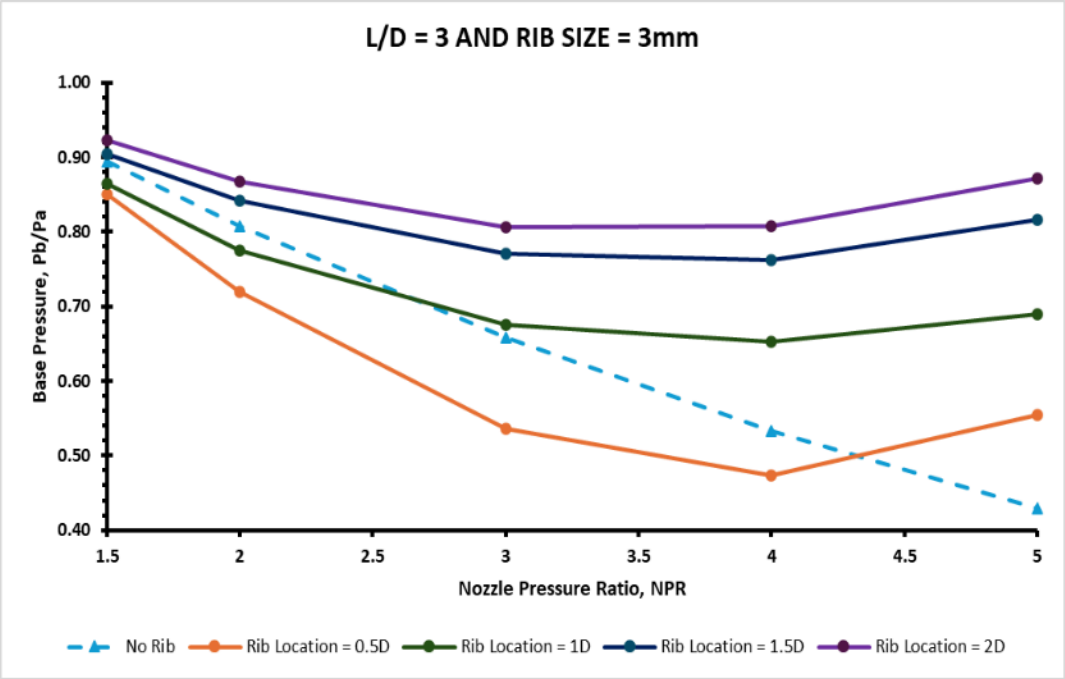

(a)

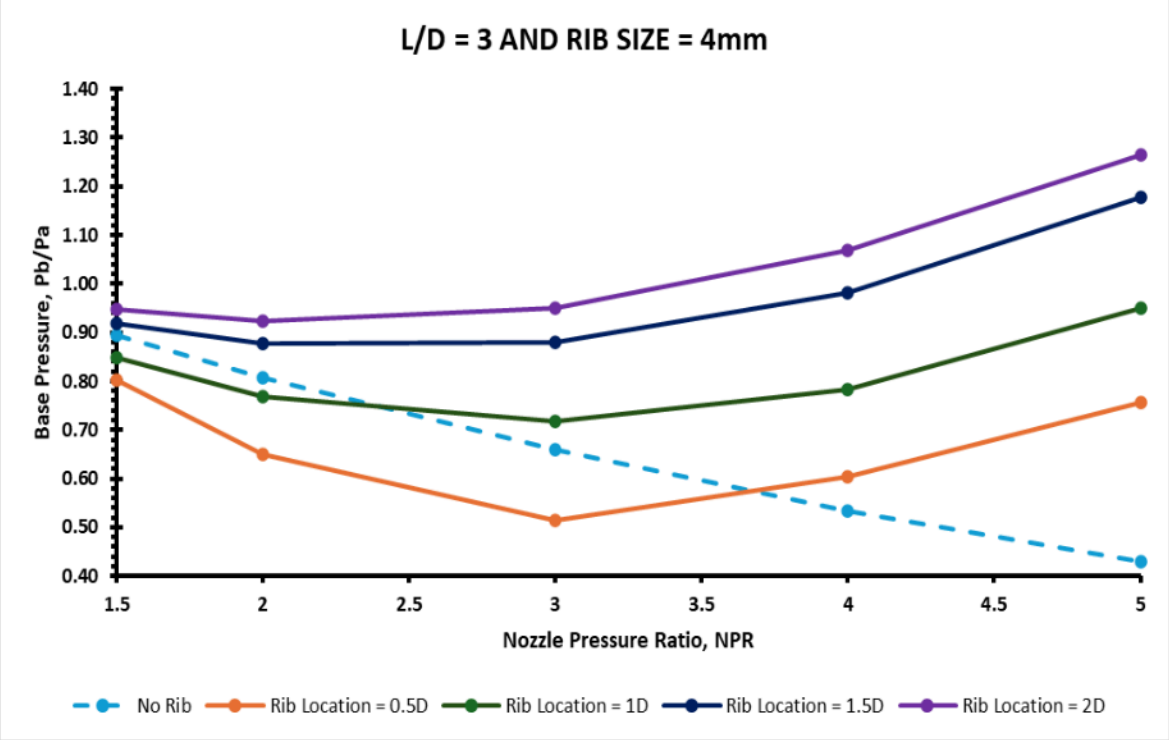

(b)

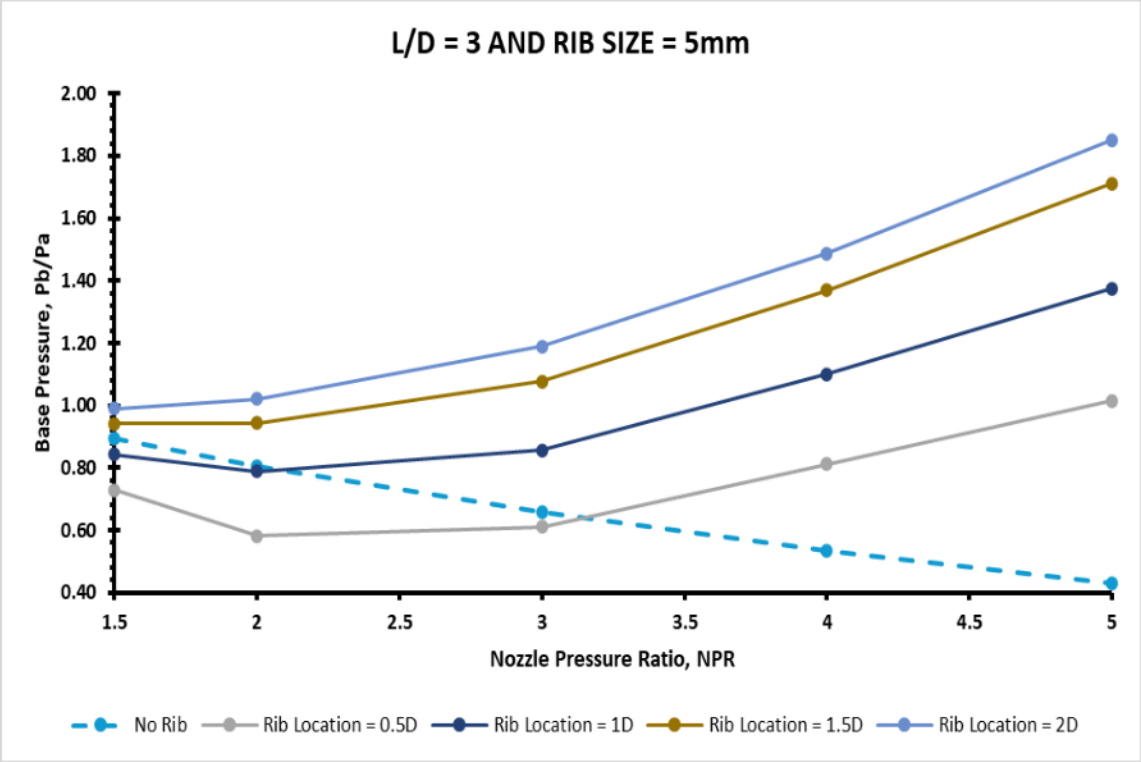

(c)

Fig. 12. Base pressure vs. NPR for various rib locations for duct length L = 3D

For the largest rib radius of 5 mm, the results of this investigation are illustrated in Figure 13 for various levels of expansion and rib locations for the duct dimension 3D. It is found that for 0.5D rib location, with an increase in the rib radius from 3 mm to 5mm, there is a negligible decay in the initial base pressure values; however, the reverse trend remained at NPR = 3, but at higher NPRs, the base pressure is 20% more than free stream pressure. Similarly, for other rib locations, there is a progressive increase in base pressure for all rib placements, and at the highest NPRs, it increases base pressure by 20%, 40%, and 60% more than ambient pressure.

Base pressure results for 3 mm radius ribs for various rib locations for duct size L = 4D are displayed in Figure 13(a). For 0.5D rib location, the results are similar to those for duct length 2D and 3D. For this duct length, the declining trend also reverses at NPR = 4, and the base pressure estimates are nearly identical. For other locations, a reversal in the trend occurs from NPR = 3, as indicated by 1D, 1.5D, 2D, and 3D. For this case, an additional rib position is 3D; for this position, there is a slight growth in the base pressure. Additionally, the highest increase in base pressure for rib locations is 0.5D, 1D, and 1.5D. Then, the growth in base pressure is marginal for both 2D and 3D positions of the ribs over the same range of NPRs.

Figure 13(b) depicts a similar outcome of the base pressure for a 4 mm rib radius at various rib locations for duct length 4D. Only a marginal decrease in the initial amounts of the base pressure and a 20 % rise in the base pressure when NPR = 3.

Figure 13(c) presents base pressure results for a 5 mm radius for rib positions 0.5D to 3D for duct length L = 4D. These results are similar, showing a total growth in base pressure at these rib sizes and locations. However, the degree of the rise in the base pressure is diminished for rib locations 2D and 3D. This may be due to the shape of the rib, its location, interactions with waves formed, and the lower influence of ambient pressure.

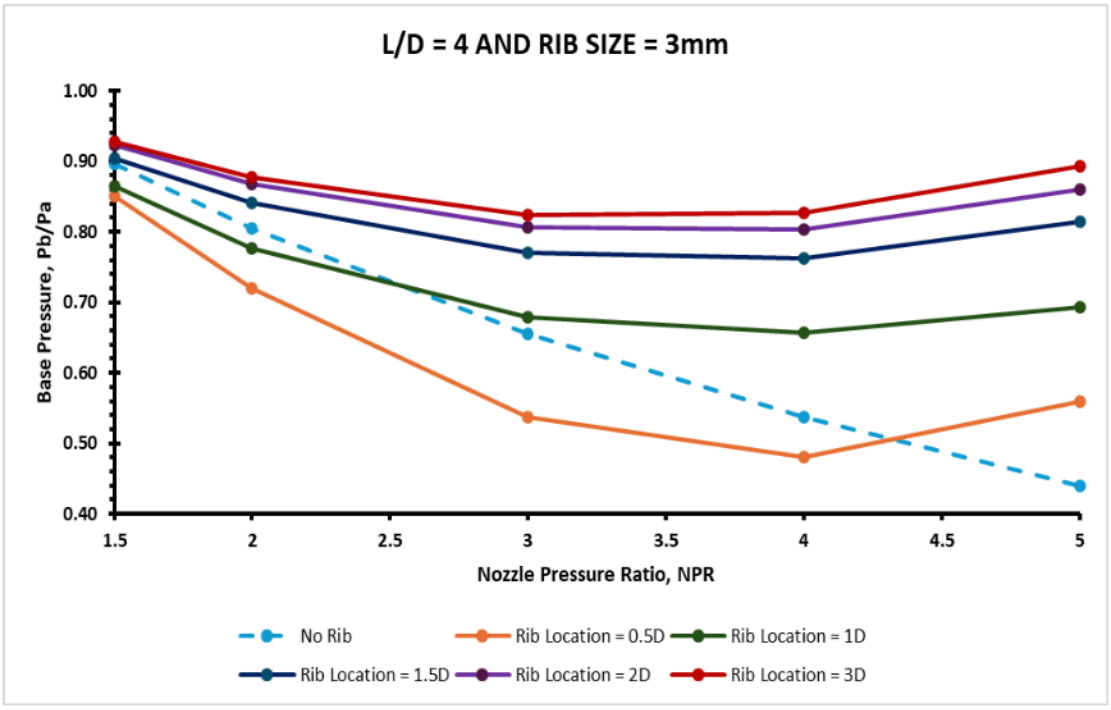
L/D = 4 AND RIB SIZE = 3mm
Base Pressure, Pb/Pa
1.00
0.90
0.80
0.70
0.60
0.50
0.40
1.5
2
2.5
3
3.5
4
4.5
5
Nozzle Pressure Ratio, NPR
No Rib
Rib Location = 0.5D
Rib Location = 1D
Rib Location = 1.5D
Rib Location = 2D
Rib Location = 3D

(a)

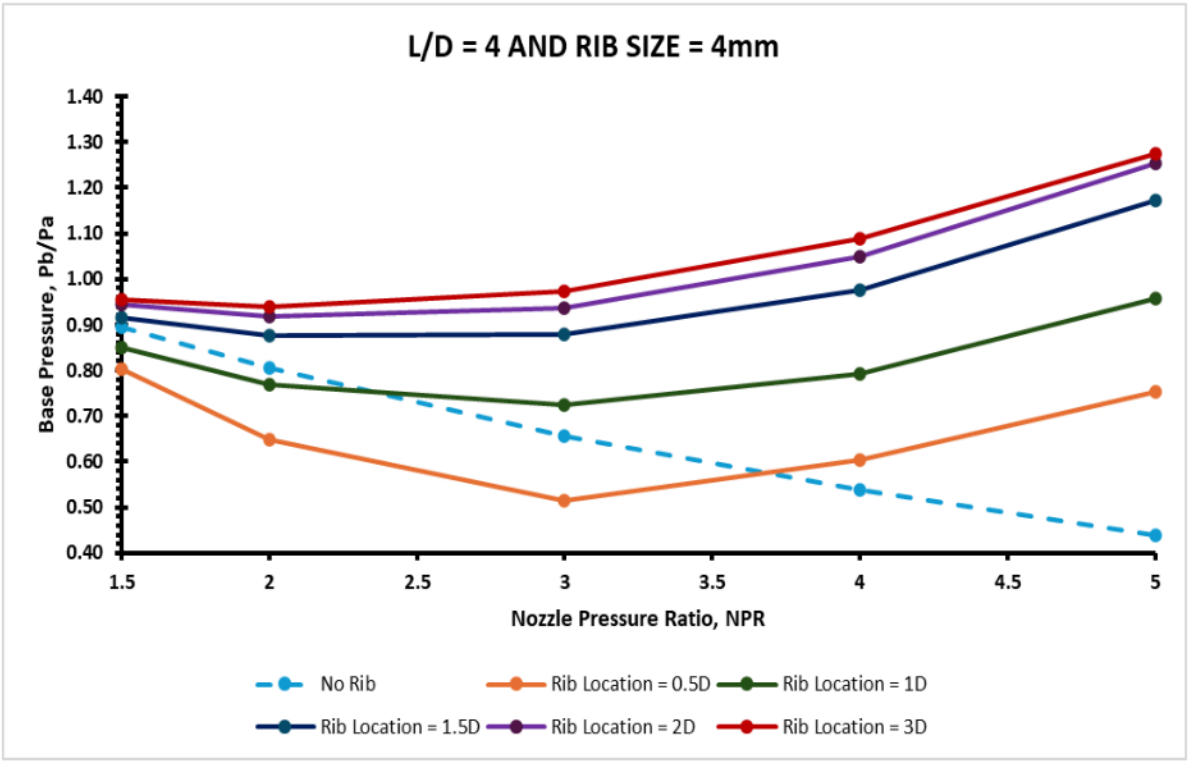
L/D = 4 AND RIB SIZE = 4mm
Base Pressure, Pb/Pa
1.40
1.30
1.20
1.10
1.00
0.90
0.80
0.70
0.60
0.50
0.40
1.5
2
2.5
3
3.5
4
4.5
5
Nozzle Pressure Ratio, NPR
No Rib
Rib Location = 0.5D
Rib Location = 1D
Rib Location = 1.5D
Rib Location = 2D
Rib Location = 3D

(b)

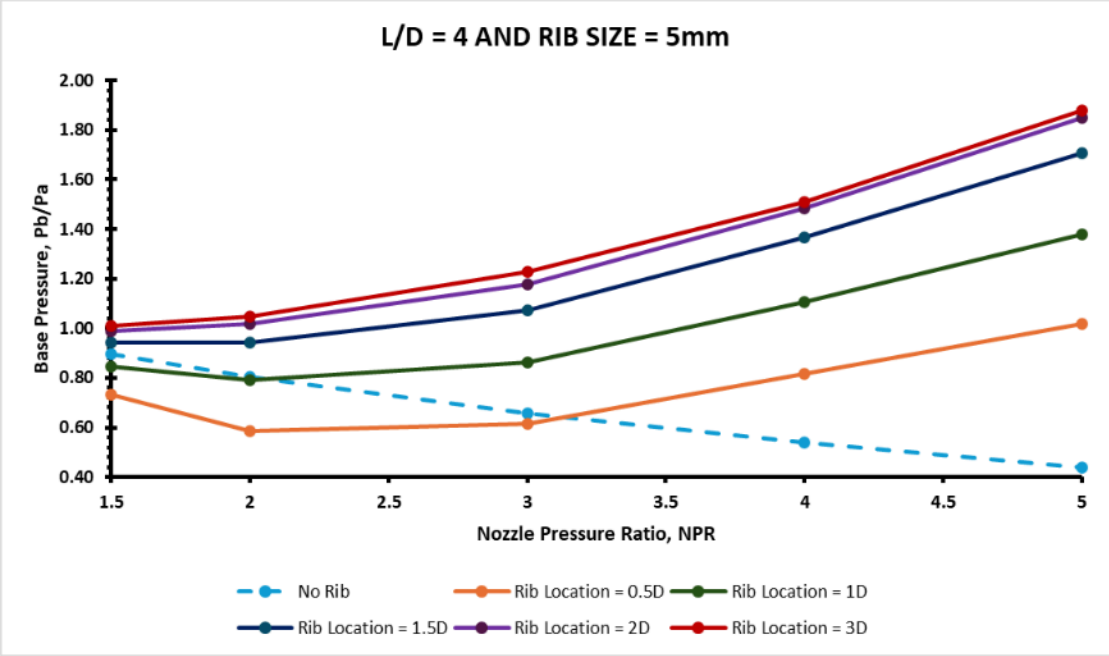

(c)

Fig. 13. Base pressure vs. NPR for various rib locations for duct length L = 4D

Figure 14(a) presents base pressure results for a 3 mm radius for rib settings 0.5D to 3D for duct length L = 5D. These results are comparable to those observed for lower duct lengths. There is a total growth in the base pressure at these rib sizes and locations. However, the degree of the rise in the base pressure is diminished for rib locations 1.5D, 2D, and 3D. That may be due to the shape of the rib, its location, its interactions with waves formed, and the lower influence of ambient pressure.

Figure 14(b) presents the findings of this study for rib radius 4 mm duct length L = 5D for five rib locations. There is an insignificant rise in the base pressure quantities, as the influence of the ambient pressure is reduced due to the increased duct length and the increase in duct dimension.

Figure 14(c) presents the findings of this study for rib radius 5 mm duct length L = 5D for five rib locations. Here, for this case, the rib radius is the extreme of the present findings, with substantial growth in the base pressure; however, the pattern is nearly the same as was seen for the shorter duct segment, namely L = 4D. Due to the increase in duct dimension, there is a minor increase in base pressure, as the influence of back pressure is reduced by the larger duct size of 5D.

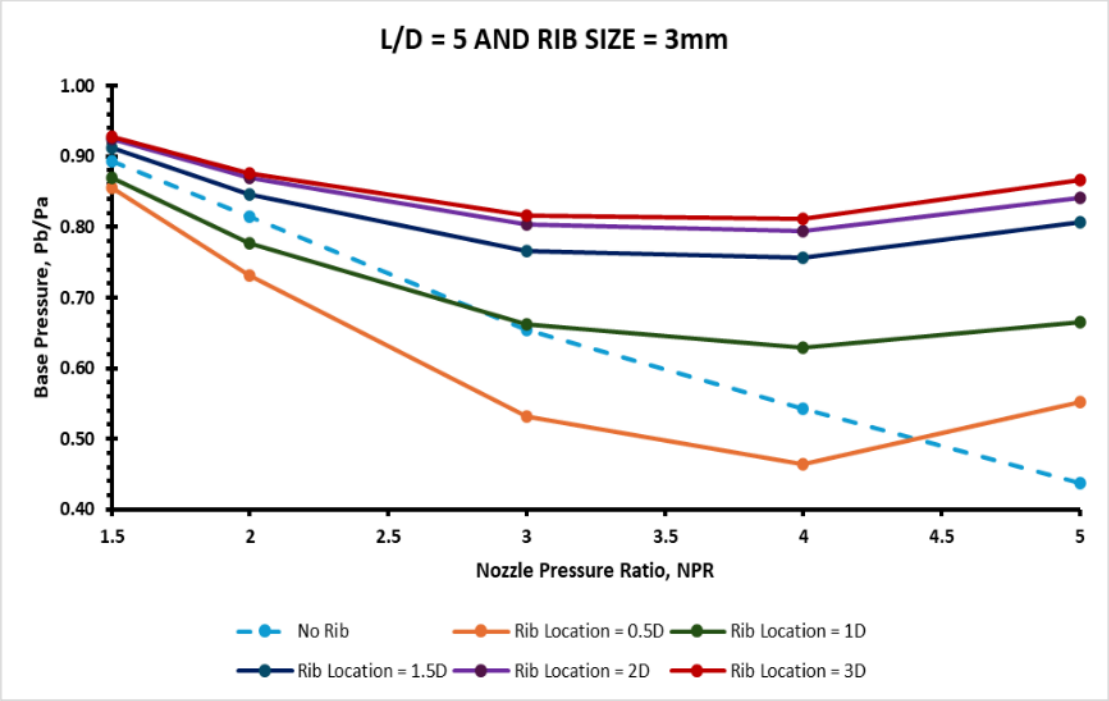
L/D = 5 AND RIB SIZE = 3mm
Base Pressure, Pb/Pa
1.00
0.90
0.80
0.70
0.60
0.50
0.40
1.5
2
2.5
3
3.5
4
4.5
5
Nozzle Pressure Ratio, NPR
No Rib
Rib Location = 0.5D
Rib Location = 1D
Rib Location = 1.5D
Rib Location = 2D
Rib Location = 3D

(a)

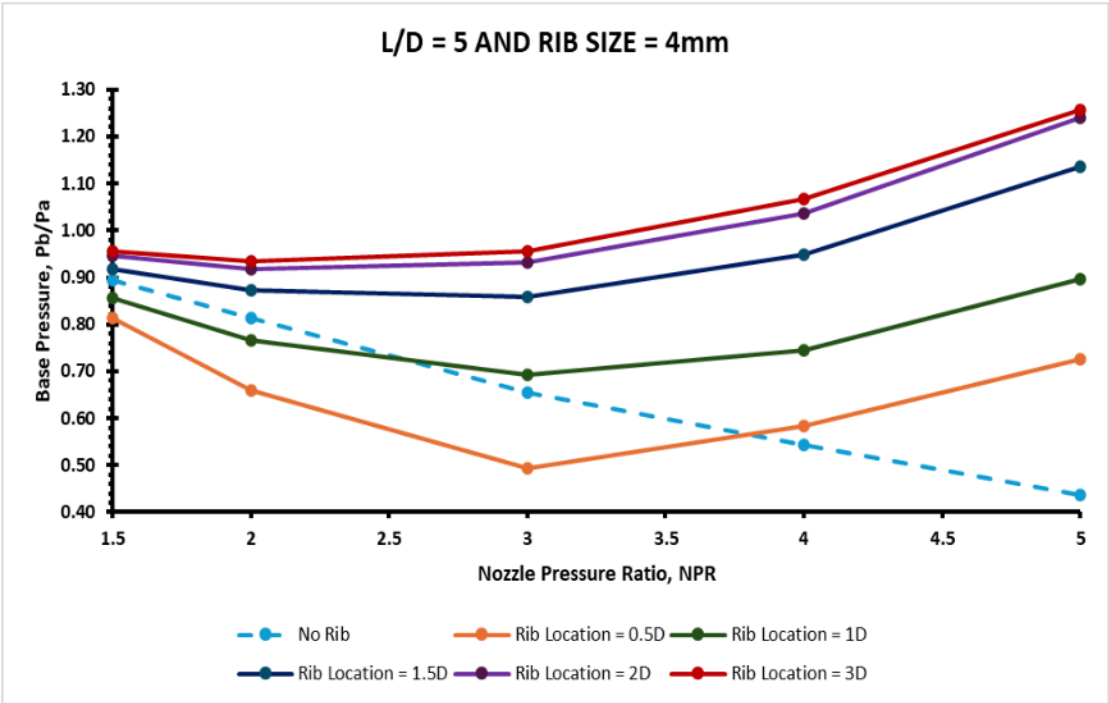
L/D = 5 AND RIB SIZE = 4mm
Base Pressure, Pb/Pa
1.30
1.20
1.10
1.00
0.90
0.80
0.70
0.60
0.50
0.40
1.5
2
2.5
3
3.5
4
4.5
5
Nozzle Pressure Ratio, NPR
No Rib
Rib Location = 0.5D
Rib Location = 1D
Rib Location = 1.5D
Rib Location = 2D
Rib Location = 3D

(b)

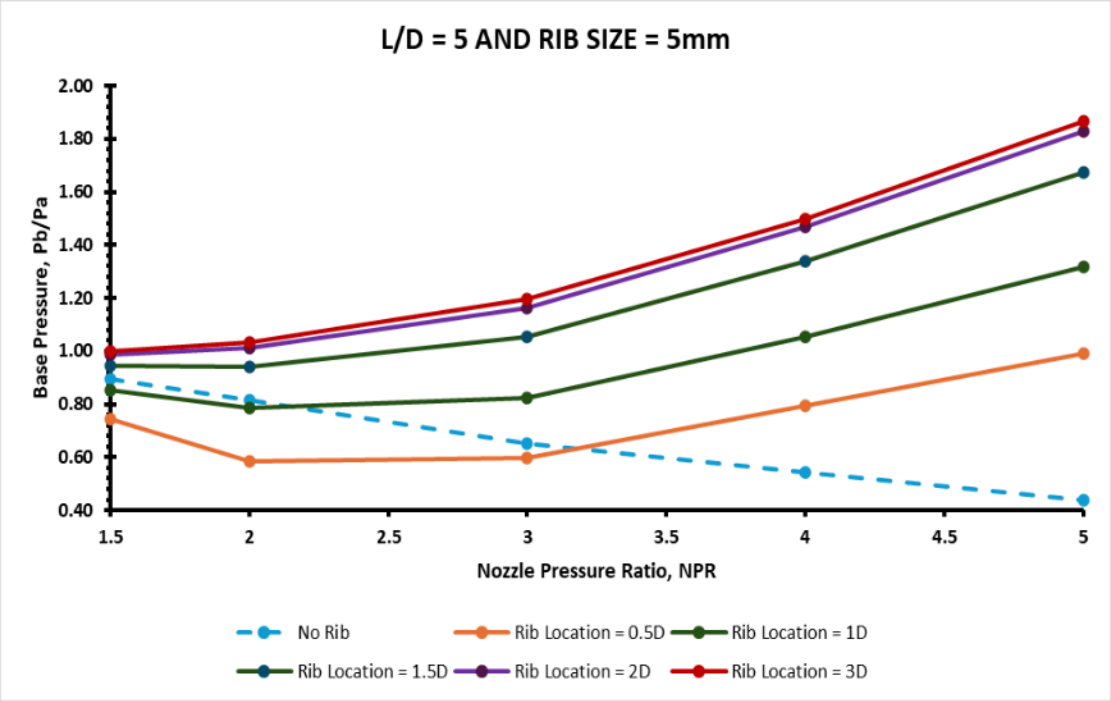

(c)

Fig. 14. Base pressure vs. NPR for various rib locations for duct length L = 5D

Figure 15(a) presents base pressure results for a 3 mm radius for rib positions 0.5D to 3D for duct length L = 6D. These results are similar to those observed for lower duct lengths—a growth in base pressure for all rib sizes and positions. However, the increase in base pressure is diminished for rib positions from 1.5D to 3D. This may be due to the size and shape of the rib, its placement, interactions with waves in the recirculation zone, and the absence of ambient pressure's influence.

Figure 15(b) presents the findings of this study for rib radius 4 mm duct length L = 6D for five rib locations. Due to the maximum duct length, there is an insignificant rise in the base pressure magnitudes, as the influence of ambient pressure is negligible when the duct size is increased.

Figure 15(c) presents the findings of this study for rib radius 5 mm duct length L = 6D for five rib locations. The rib radius is the highest in the current research for this case. A considerable increase in the base pressure is observed; however, the flow behavior remains nearly the same for lower duct sizes, namely L = 4D and 5D. Due to the increase in duct span, there is an insignificant rise in base pressure magnitude, as the influence of ambient pressure is negligible due to the increased duct length of 6D.

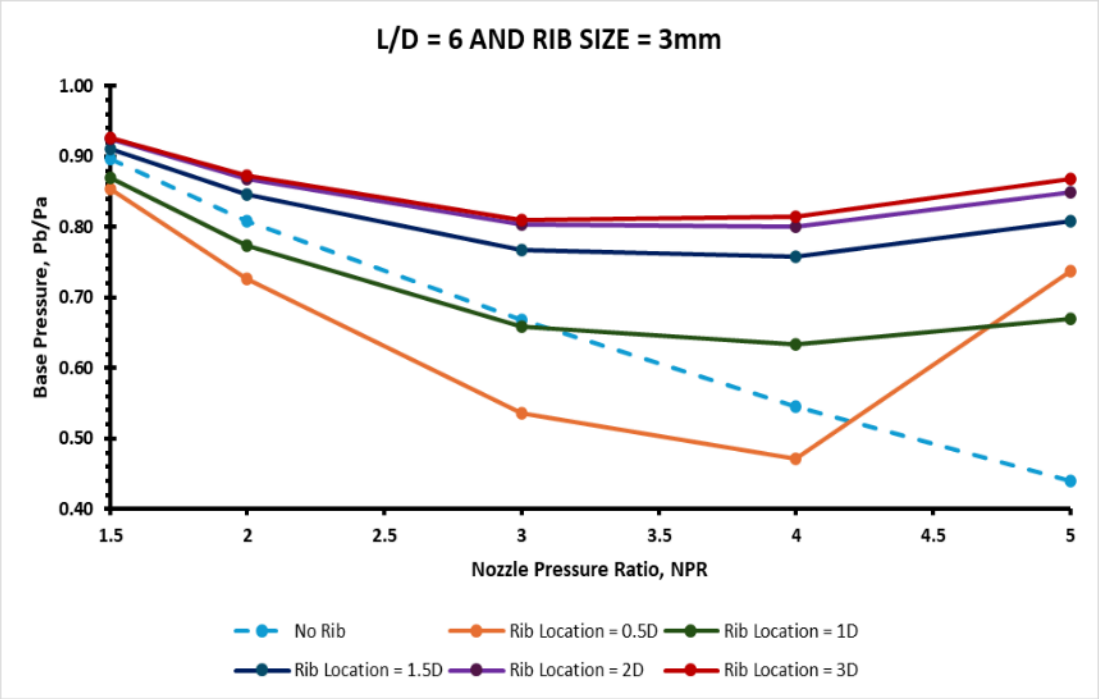
L/D = 6 AND RIB SIZE = 3mm
Base Pressure, Pb/Pa
1.00
0.90
0.80
0.70
0.60
0.50
0.40
1.5
2
2.5
3
3.5
4
4.5
5
Nozzle Pressure Ratio, NPR
No Rib
Rib Location = 0.5D
Rib Location = 1D
Rib Location = 1.5D
Rib Location = 2D
Rib Location = 3D

(a)

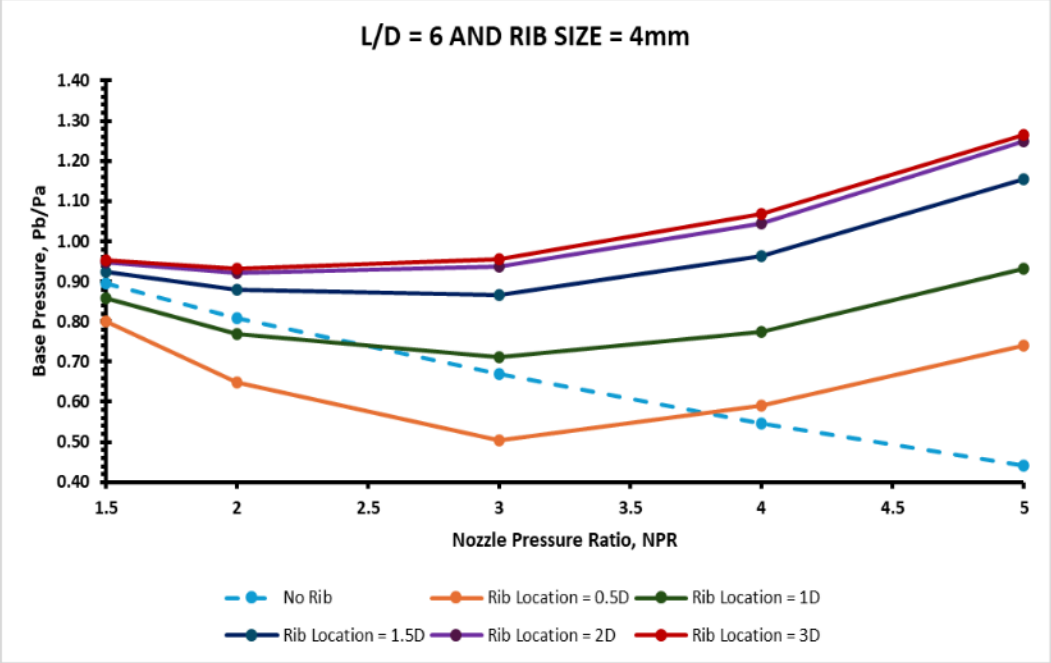
L/D = 6 AND RIB SIZE = 4mm
Base Pressure, Pb/Pa
1.40
1.30
1.20
1.10
1.00
0.90
0.80
0.70
0.60
0.50
0.40
1.5
2
2.5
3
3.5
4
4.5
5
Nozzle Pressure Ratio, NPR
No Rib
Rib Location = 0.5D
Rib Location = 1D
Rib Location = 1.5D
Rib Location = 2D
Rib Location = 3D

(b)

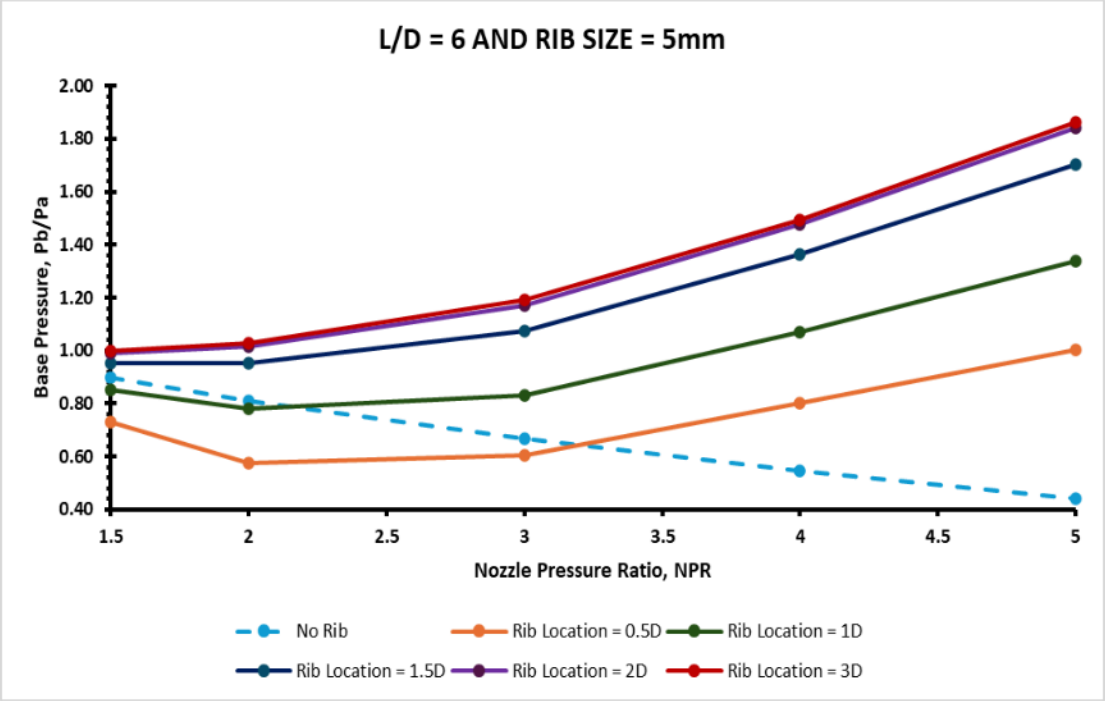

(c)

Fig. 15. Base pressure vs. NPR for various rib locations for duct length L = 6D

4.4 Base Pressure vs. NPR for Rib Orientation 2 at Different Rib Locations

Figure 16 shows rib orientation 2. In this section, the base pressure results are presented for orientation 2, where the flow exits the nozzle and faces the curved part of the rib. It is a quarter of the circle, where one side is straight and is given nomenclature as orientation 1, whereas the curved part facing the flow is named orientation 2. This section discusses the results of orientation 2 for various rib radii and locations.

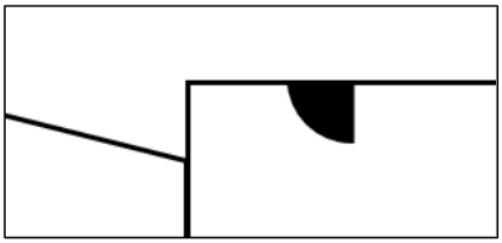

Fig. 16. Rib orientation 2

Figure 17(a) shows base pressure results at various NPRs for rib radius 3 mm, 4 mm, and 5 mm for duct length L = 1D while the rib is at 0.5D. When we compare the results with the reference of orientation 1, it is found that the base pressure pattern remains identical. However, the scale of the base pressure is reduced marginally. This reduction in the base pressure magnitude is attributed to the shape of the rib, which is a quarter circle with a smooth variation in rib height, resulting in a weak vortex and, consequently, reduced base pressure values. For a rib radius of 5 mm, the base pressure attained the ambient pressure values, whereas, for rib radii 3 mm and 4 mm, the base pressure values are 15% and 20%, respectively, less than the free stream pressure.

The base pressure results for the 2D duct segment at 0.5D and 1D rib positions, with rib radii of 3, 4, and 5 mm, are presented in Figure 17(b). The early base pressure is marginally lower than that

of orientation 1 for all rib locations and radii. The figure shows that for a 1D rib location with a 5 mm radius, the base pressure is 30% more than the ambient pressure. Base pressure values for rib radius and location 5 mm, 4mm, and 0.5D and 1D merge at NPR = 4. It is seen that when ribs are placed at 1D, they perform better for the same radius ribs when located at 0.5D. Control effectiveness for rib radii of 3 mm and 4 mm, when placed at 0.5D and a 3 mm radius located at 1D, is nominal, and the control cannot reduce the suction created in the base area. Another cause for this trend is that the duct segment is small, the flow is unattached to the duct, and the flow field of the duct is open to ambient pressure.

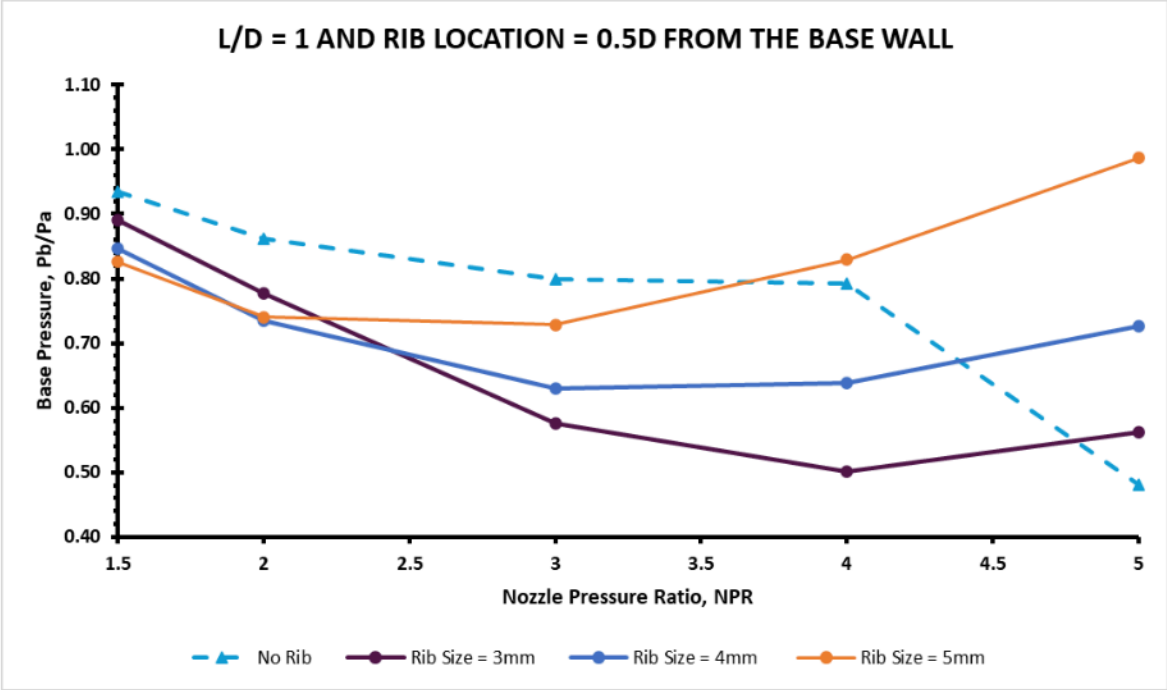

(a)

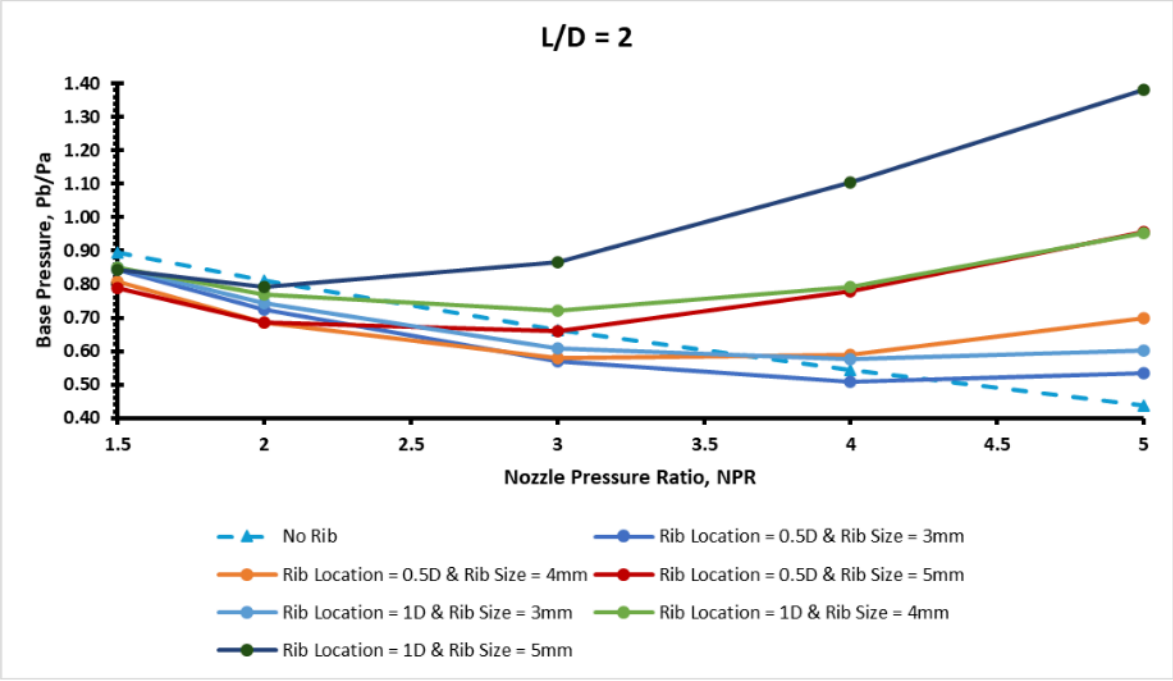

(b)

Fig. 17. Base pressure vs. NPR for various rib locations for duct length L = 2D

Figure 18(a) shows base pressure results for rib radius 3 mm and rib positions 0.5D and 1D for duct length 2D. Since the duct diameter is 25 mm, which is significantly high, passive control is ineffective. Up to NPR = 4, the presence of rib base pressure declines. However, a declining trend in the base pressure is no longer from NPR = 4, where under-expansion is 2 (i.e., Pe/Pa = 2.0).

Figure 18(b) shows base pressure results for rib radius 4 mm and rib positions 0.5D and 1D for duct length 2D. Due to the increase in the rib radius, there is a substantial change in the flow. In the previous case, the decreasing tendency continued to NPR = 4. However, the decline in the base pressure is reversed when the nozzle achieves critical conditions. The base pressure value is equal to the back pressure for a 4 mm rib radius and a 1D rib location, whereas for a 0.5D rib, it is 30% less than the ambient pressure.

Base Pressure results for duct length 2D and rib radius 5 mm at rib placed 0.5D & 1D are illustrated in Figure 18(c). Due to the growth in the rib radius, the base pressure has increased considerably, and for 0.5D and 1D rib locations, the values are 1 and 1.4, respectively.

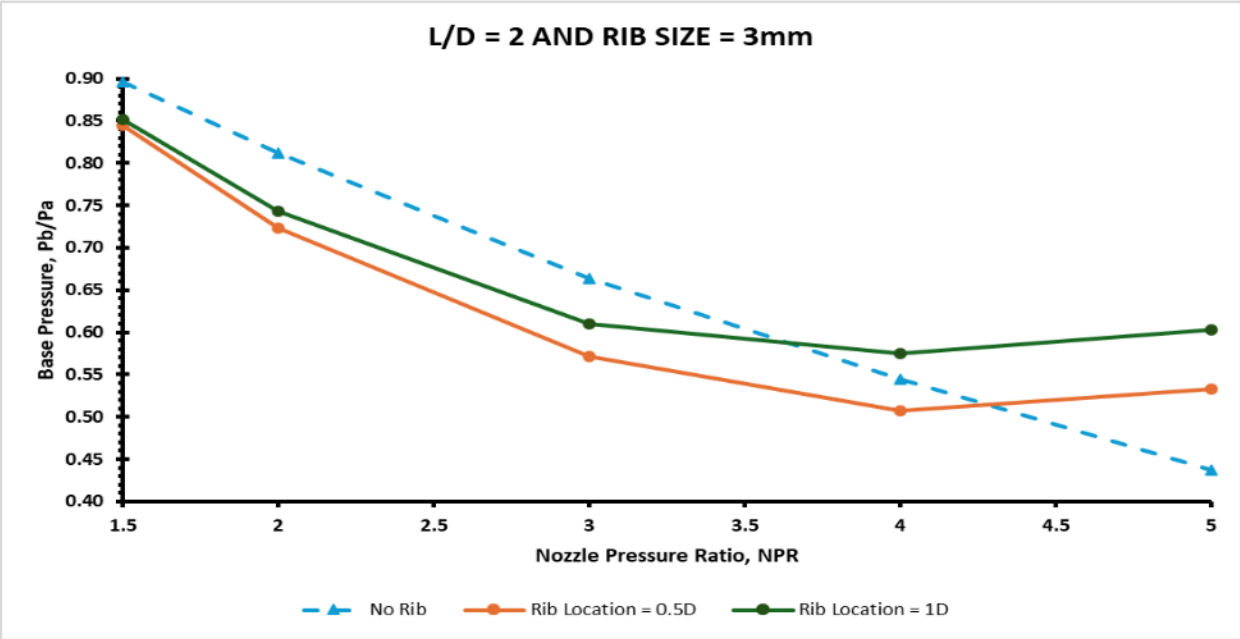

(a)

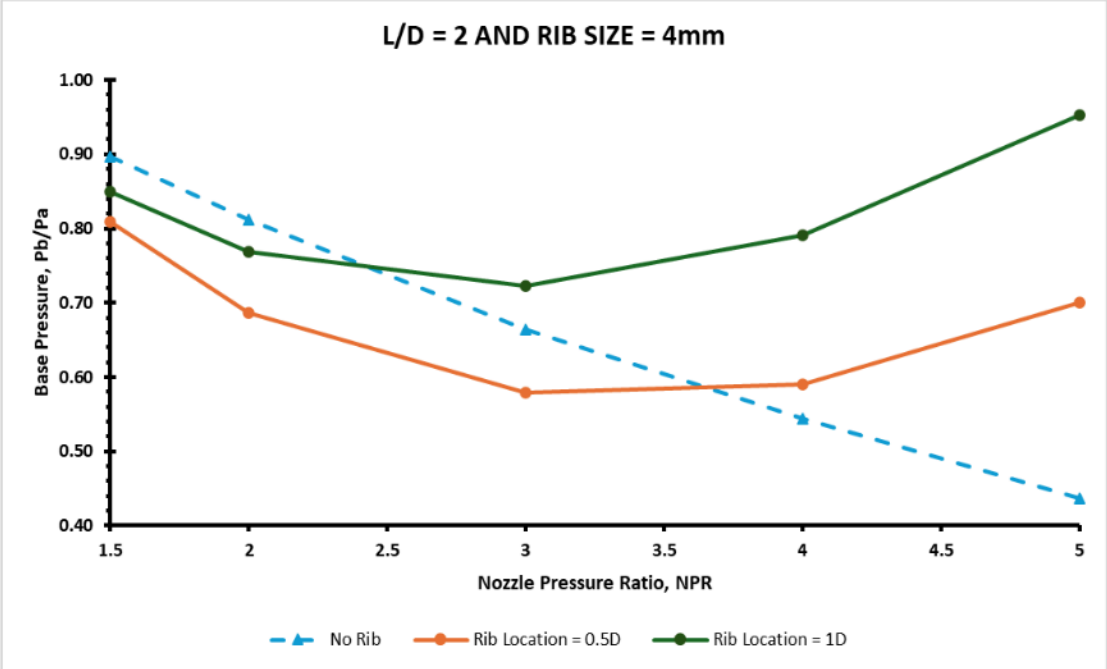

(b)

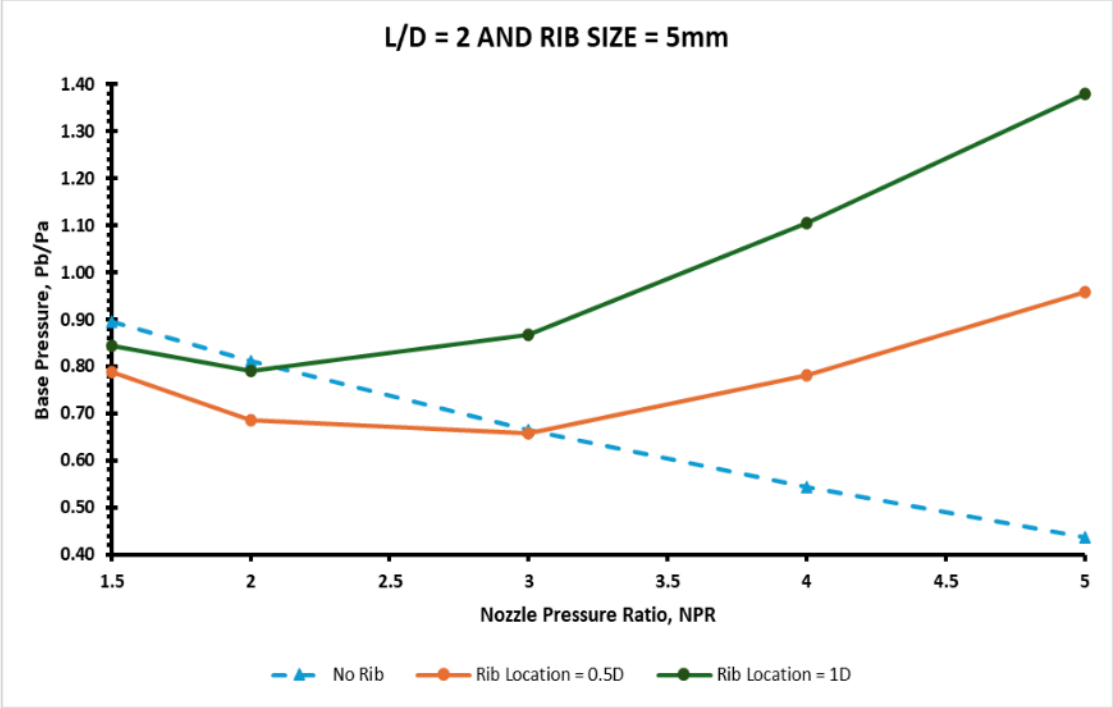

(c)

Fig. 18. Base pressure vs. NPR for various rib locations for duct length L = 2D

Base Pressure results for duct length 3D and rib radius 3 mm at rib settings 0.5D to 2D are shown in Figure 19(a). As discussed earlier, the lowest radius of the rib is 3 mm, which cannot influence the base flow. The trend is similar to the lower duct length.

Figure 19(b) shows the results for a rib radius of 4 mm and various rib locations for a duct length of 3D. The decreasing base pressure phenomenon, which occurs until NPR = 4, is reversed at NPR = 2. However, base pressure values for control locations 0.5D and 1D are still less than those without control values. However, the increasing trends start from NPR = 2.5 and 3.5 for 1D and 0.5D rib

locations. For rib placement of 1.5D and 2D, there is growth in the base pressure, but the difference in the magnitude of these two rib placements is marginal. The main factors that control the base pressure are the rib radius and expansion level. The rib location becomes critical when it is placed near the reattachment point.

When the rib radius is 5 mm and the duct length is 3D, the findings of this study are presented in Figure 19(c) for different rib positions. Only for rib position 0.5D, the control results in a decline in the base pressure. For NPR values of 3 and above, a growth in the base pressure is observed, with values near ambient pressure. For other rib locations, once the nozzle attains critical conditions, there is a progressive rise in base pressure. For the highest NPR at these four locations, the base pressure values are close to atmospheric pressure, with 10%, 40%, and 60% more than atmospheric pressure.

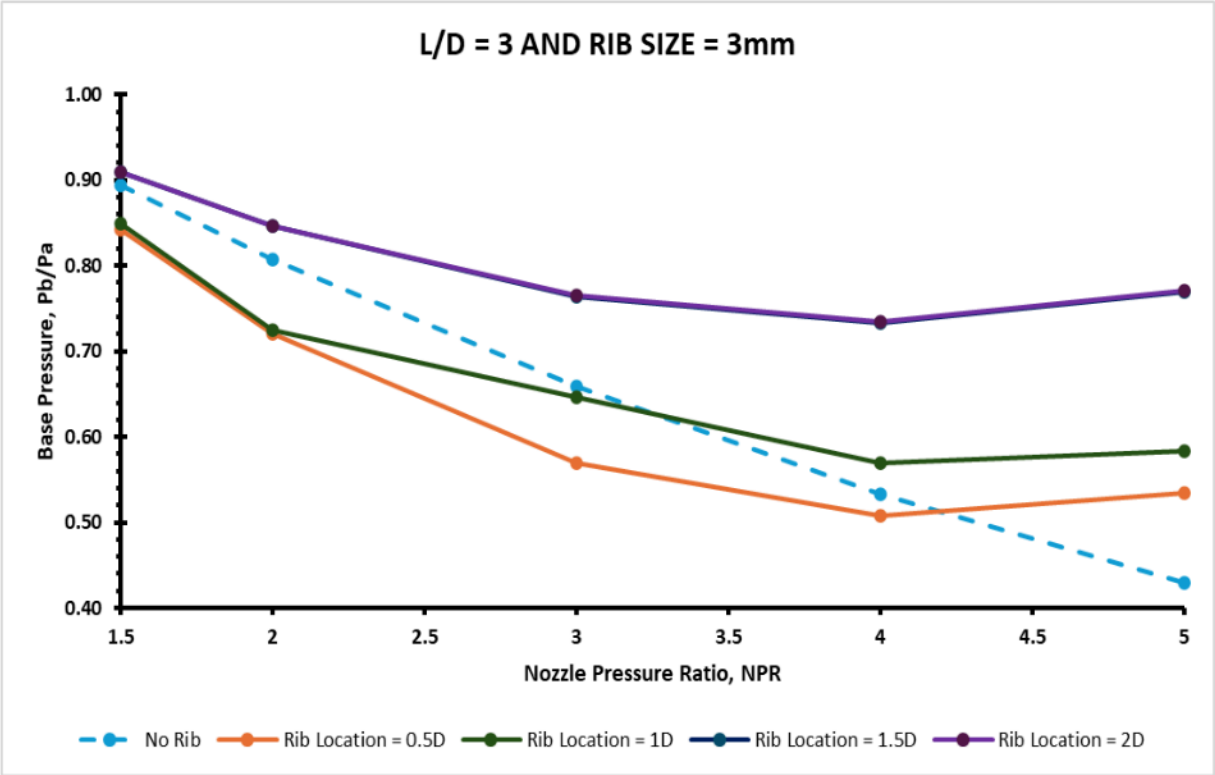

(a)

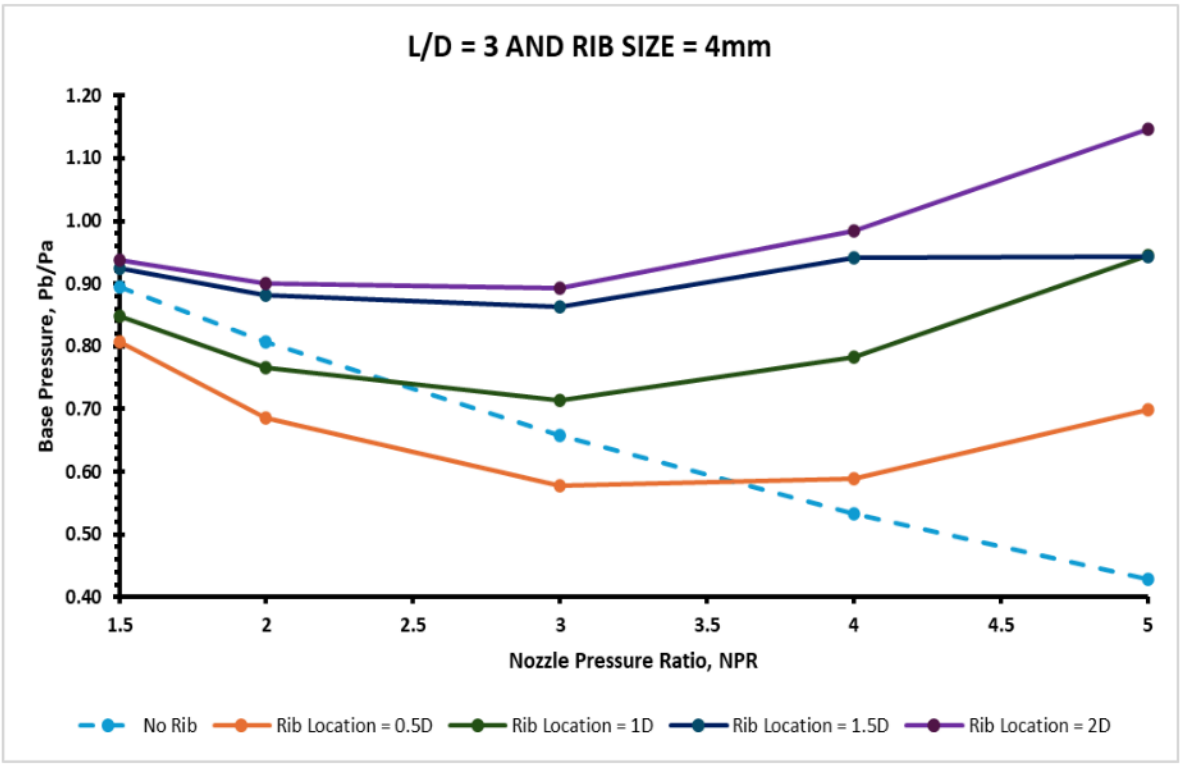

(b)

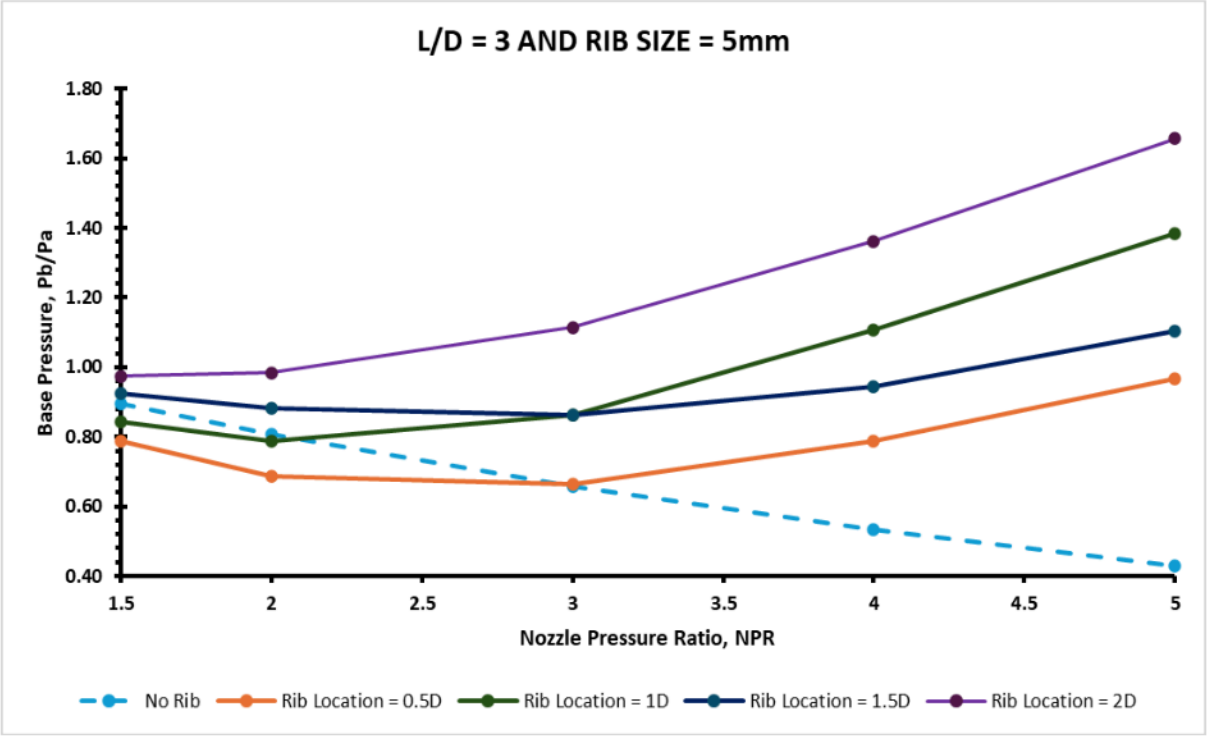

(c)

Fig. 19. Base pressure vs. NPR for various rib locations for duct length L = 3D

Base Pressure results for rib radius of 3 mm and duct length L = 4D are shown in Figure 20(a). For the more significant duct segment of 4D, the decreasing trend has shifted to NPR = 4.2, with insignificant growth in base pressure at NPR = 5. When examining the results for other locations of the ribs, it is found that there is no effect of rib location in this case. There are a few relevant factors:

rib radius and duct length. The ambient pressure's small influence has made the base pressure independent of rib locations.

Base Pressure results for a rib radius = 4 mm and duct length L = 4D are shown in Figure 20(b). At an increased duct dimension of 4D and a rib radius of 4 mm, the decreasing trend has shifted to NPR = 3, and there is a sizable rise in base pressure at NPR = 2 and above. When we examine the results for the other three locations of the ribs, namely 1.5D, 2D, and 3D, it is found that there is no effect of rib location in this case. Whatever gain it has achieved for rib location 1.5D remains unchanged for the other two rib locations. There are a few relevant factors: rib radius and duct length. The ambient pressure's small influence has made the base pressure independent of rib positions.

Base Pressure results for a rib radius of 5 mm and duct length L = 4D are shown in Figure 20(c). At an increased duct segment of 4D and rib radius of 5 mm, the decreasing trend has shifted for NPR = 2, with a significant rise in base pressure when NPR = 2 and above. When we look at the results for the other two locations of the ribs, namely 2D and 3D, it is found that there is no effect on the rib location in this case. Whatever gain it has achieved for rib location 2D does not change for the other rib location of 3D. As the rib radius is 5 mm, there is a declining trend in the base pressure for a rib when placed at 0.5D and NPR = 3 onwards, there is a growth in the base pressure. For the 1D rib position, an increasing trend in base pressure is observed for NPR = 2 and above once the flow from the nozzle reaches critical conditions. However, when we compare the base pressure findings for rib locations 1D and 1.5D, it is evident that the 1D rib location exhibits an uninterrupted rise in base pressure. However, the base pressure values for the 1.5D rib location are less than those for the rib location at 1D. Despite the increasing trend for base pressure for 1.5D rib location, the increased gradient has diminished. There are several relevant factors: rib radius, position, and duct length. For this duct length, the ribs create excessive interactions of waves, shear layer, and vortices, resulting in a pattern in the base pressure.

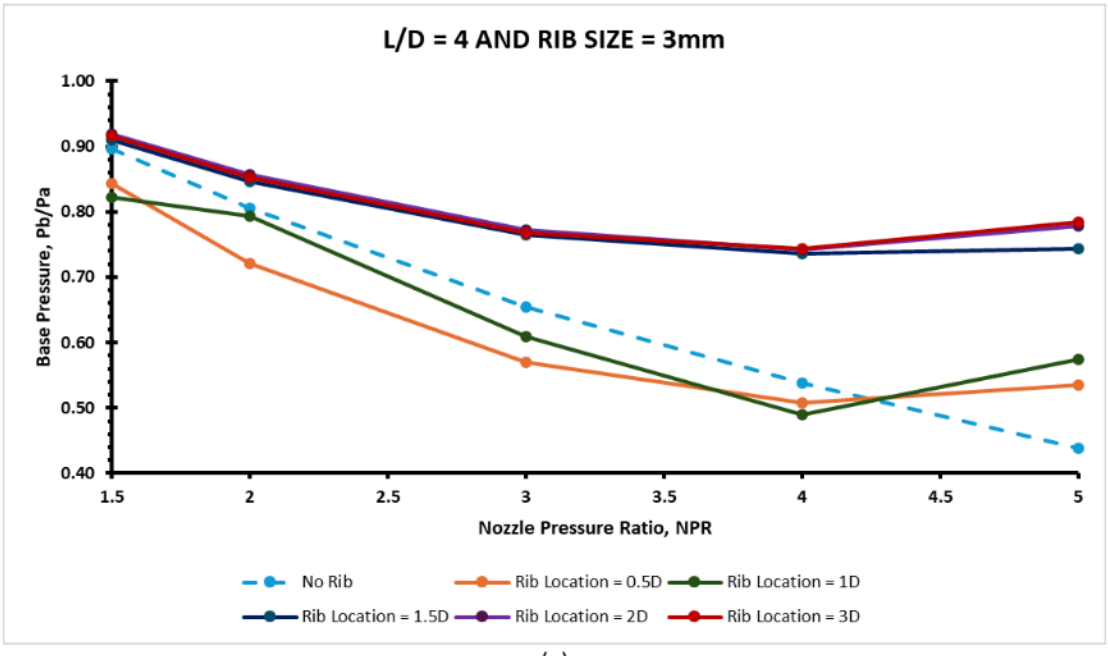

(a)

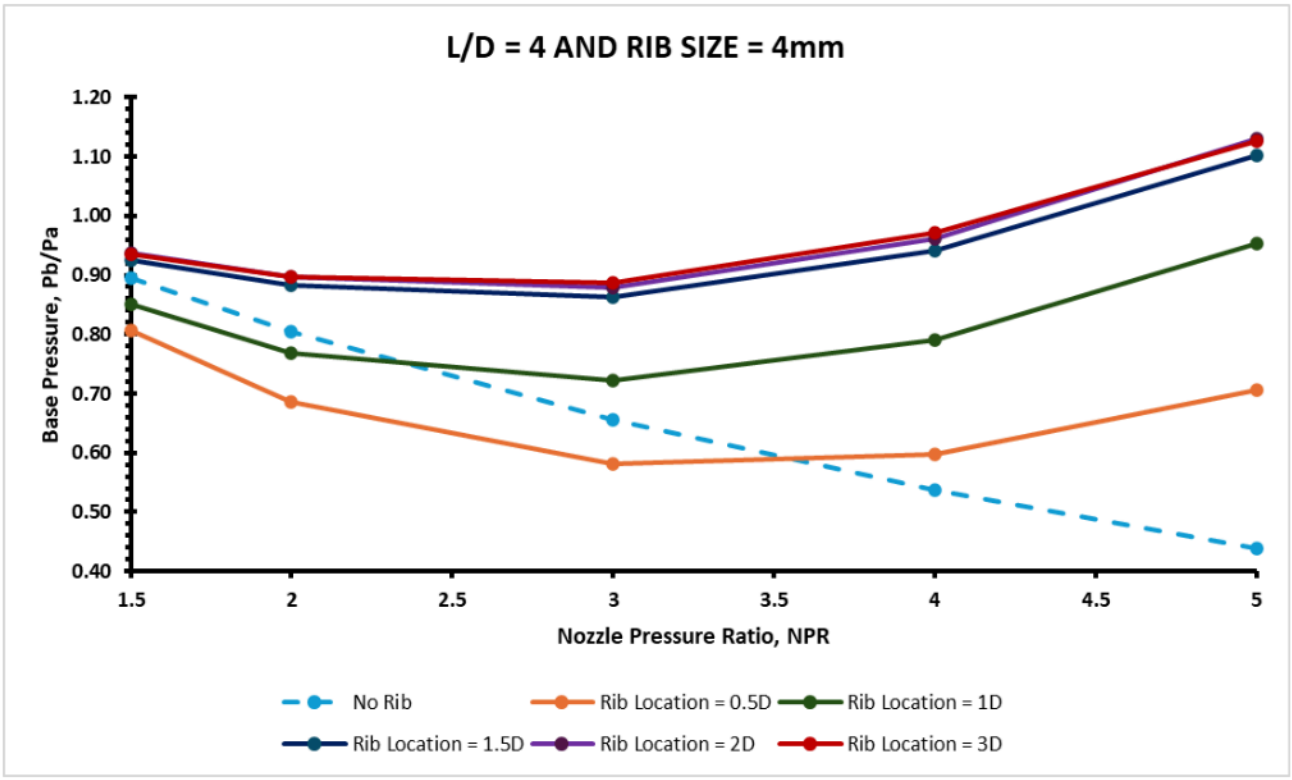

(b)

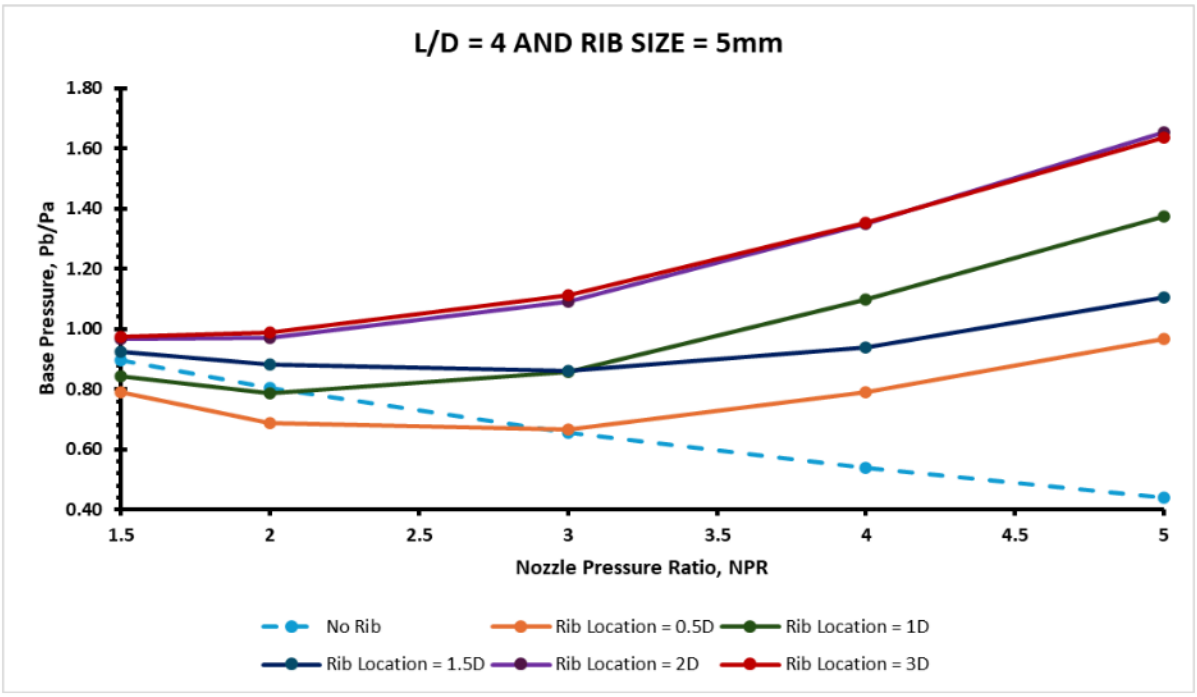

(c)

Fig. 20. Base pressure vs. NPR for various rib locations for duct length L = 4D

Base Pressure results for rib radius of 3 mm and duct length L = 5D are shown in Figure 21(a). Due to the increased duct segment of 5D, the decreasing trend has shifted to NPR = 4.2, representing an insignificant rise in base pressure at NPR = 5. These results are similar to those of duct length L = 4D. When examining the results for other rib locations (i.e., 1.5D, 2D, 3D), it is found that there is no effect of rib location in this case. There is little change in the base pressure, even though the ribs are

placed at 1.5D, 2D, and 3D. Whatever gain is attained at the rib location of 1.5D, there is not much change in the base pressure data. It appears that there is a counter-effect at the rib locations of 2D and 3D—mass from the base and reverse flow from the boundary layer result in such conditions.

Base Pressure results for a rib radius of 4 mm and duct length L = 5D are shown in Figure 21(b). Due to the increased duct length of 5D and rib radius of 4 mm, the decreasing trend has shifted to NPR = 3 for 0.5D rib locations. Base pressure is significantly rising at NPR = 2 and above for ribs located at 1D and 1.5D. When we examine the results for the other two locations of the ribs, namely 2D and 3D, it is found that there is no effect on the rib location in this case. Whatever gain it has achieved for rib location 1.5D remains unchanged for the other two rib locations. The factors responsible for this trend are the rib radius and duct length. The ambient pressure cannot influence the flow inside the duct, nor can the base pressure be independent of rib positions.

Base Pressure results for a rib radius of 5 mm and duct length L = 4D are shown in Figure 21(c). Due to the more significant duct segment of 5D and a rib radius of 5 mm, the decreasing trend has shifted to NPR = 2, resulting in a substantial growth in base pressure for NPR = 2 and higher. When we look at the results for the other two locations of the ribs, namely 2D and 3D, it is observed that there is no effect on the rib location in this case. Whatever gain it has achieved for rib location 2D does not change for the other rib location of 3D. The gain accomplished for rib location 2D remained, and the 3D rib location did not impact the base pressure. As the rib radius is 5 mm, a decreasing trend in the base pressure is observed for a rib when placed at 0.5D. However, at NPR = 3 onwards, a growth in the base pressure is noted. At the 1D rib location, an increasing trend in base pressure is observed from NPR = 2 and above once the flow from the nozzle reaches critical conditions. However, when we compare the base pressure results for rib locations 1D and 1.5D, it is seen that for the 1D rib location, there is a steady rise in the base pressure. However, the base pressure values for the 1.5D rib location are less than those for the rib location at 1D. Despite the increasing trend in the 1.5D rib site base pressure, the gradient has decreased significantly. Several key factors contribute to this pattern in the base pressure, including the rib radius, position, and duct length. The ribs create vortices along this duct length, and the waveforms inside the duct, combined with the shear layer and vortices, result in a specific pattern in the base pressure.

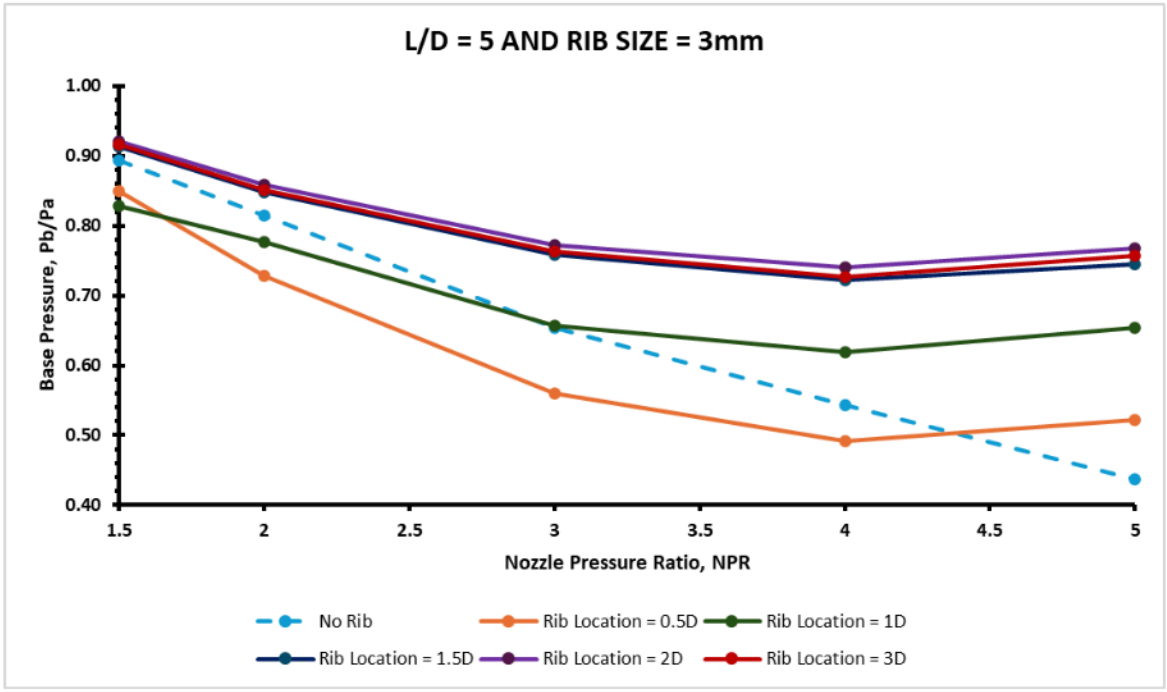

(a)

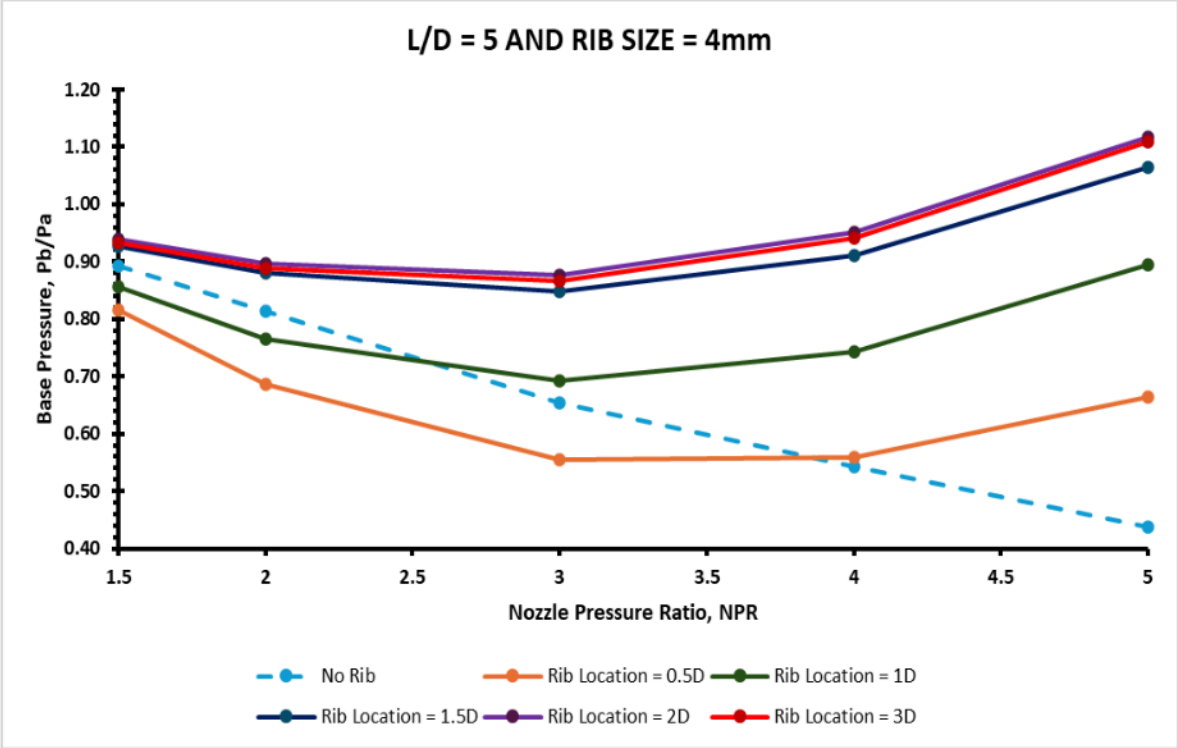

(b)

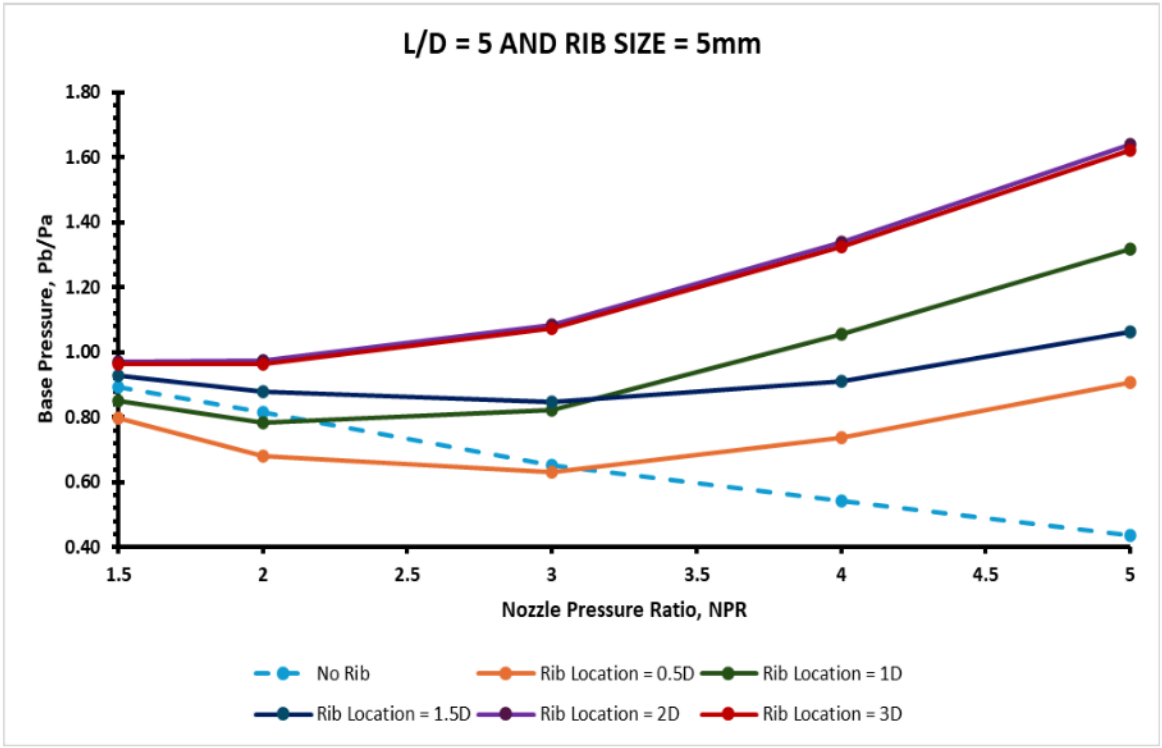

(c)

Fig. 21. Base pressure vs. NPR for various rib locations for duct length L = 5D

Base Pressure results for rib radius of 3 mm and duct length L = 6D are shown in Figure 22(a). Due to the increased duct segment of 6D, the decreasing trend has shifted to NPR = 4 for the 0.5D ribs location, and there is a marginal rise in base pressure at NPR = 5. We observe a peculiar behavior for the rib location of 1D, where there is an abrupt drop in the base pressure. It continues steadily from

NPR = 3 and 4, and later, there is a considerable rise in the base pressure. When we examine the results for other locations of the ribs (i.e., 1.5D, 2D, 3D), it is found that these results are on a similar line to that seen for lower duct length, and there is no effect of rib location in this case. There is no alteration in the base pressure even though the rib locations are changed from 1.5D to 2D and from 2D to 3D. The base pressure values remain almost the same for whatever gain is acquired at the rib location of 1.5D. It appears that there is an opposite flow from the shear layer region at the rib locations of 2D and 3D—mass from the base and reverse flow from the boundary layer contribute to such conditions.

Base Pressure results at a rib radius of 4 mm and duct length L = 6D are shown in Figure 22(b). Due to the increased duct length of 6D and rib radius of 4 mm, the decreasing trend has shifted to NPR = 3 for 0.5D rib locations. Base pressure is significantly rising at NPR = 2 and above for ribs located at 1D and 1.5D. When we examine the results for the other three locations of the ribs, namely 1.5D, 2D, and 3D, it is found that there is no effect on the rib location. Whatever gain it has achieved for rib location 1.5D remains almost intact. The factors responsible for this trend are the rib radius, locations, and duct size. The ambient pressure does not impact the flow inside the enlarged duct, and the base pressure is independent of the rib positions.

Base Pressure results for a rib radius of 5 mm and duct length L = 6D are shown in Figure 22(c). For an increased duct dimension of 6D and a rib radius of 5 mm, the decreasing trend has shifted to NPR = 2, and there is a sizable increase in base pressure at NPR = 2 and above. When we examine the results for the other two locations of the ribs, namely 2D and 3D, it is found that there is no effect on the rib location within this range of parameters. Whatever increase in the base attained for rib location 2D does not change for the rib location of 3D. As the rib radius is 5 mm, a decaying trend in the base pressure is observed for a rib when placed at 0.5D; however, at NPR = 3 onwards, a growth in the base pressure is noted. For 1D rib location, an increasing trend in base pressure is observed from NPR = 2 and above, once the flow from the nozzle attains critical conditions. However, when we compare the base pressure results for rib locations 1D and 1.5D, it is seen that for the 1D rib location, there is a continuous rise in the base pressure. However, the base pressure values for the 1.5D rib location are less than those for the rib location at 1D. These results restate that the stream has attained a steady state and is fully developed. Despite the increasing trend for base pressure for 1.5D rib location, the increased gradient has been reduced. Several key factors contribute to this pattern in the base pressure, including the rib radius, position, and duct length. The ribs create vortices along this duct length, and the waveforms inside the duct, combined with the shear layer and vortices, result in a specific pattern in the base pressure.

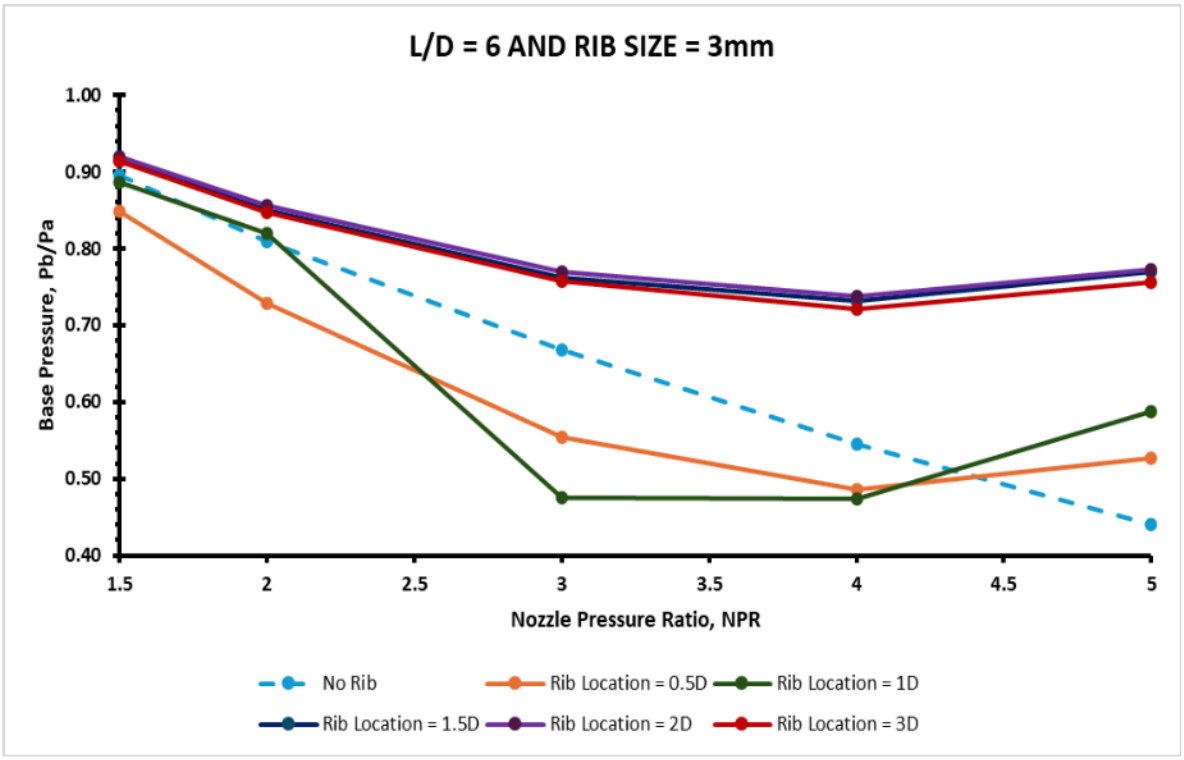
L/D = 6 AND RIB SIZE = 3mm
Base Pressure, Pb/Pa
1.00
0.90
0.80
0.70
0.60
0.50
0.40
1.5
2
2.5
3
3.5
4
4.5
5
Nozzle Pressure Ratio, NPR
No Rib
Rib Location = 0.5D
Rib Location = 1D
Rib Location = 1.5D
Rib Location = 2D
Rib Location = 3D

(a)

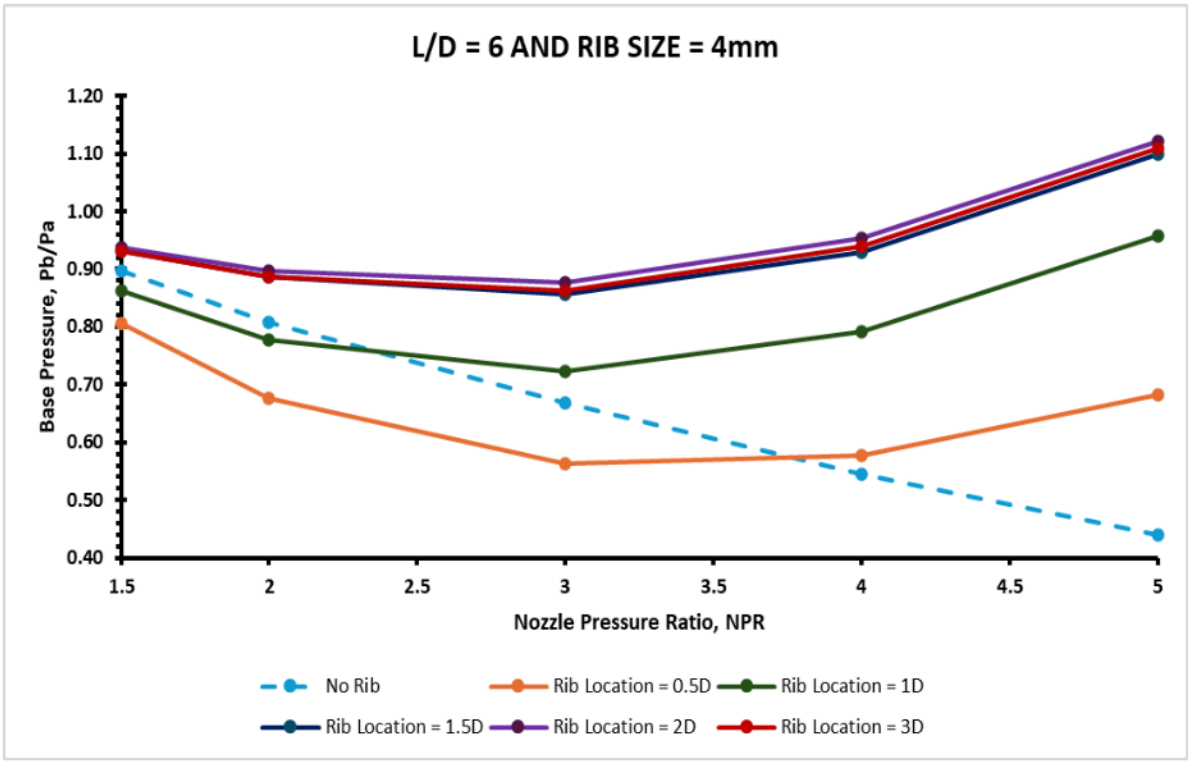
L/D = 6 AND RIB SIZE = 4mm
Base Pressure, Pb/Pa
1.20
1.10
1.00
0.90
0.80
0.70
0.60
0.50
0.40
1.5
2
2.5
3
3.5
4
4.5
5
Nozzle Pressure Ratio, NPR
No Rib
Rib Location = 0.5D
Rib Location = 1D
Rib Location = 1.5D
Rib Location = 2D
Rib Location = 3D

(b)

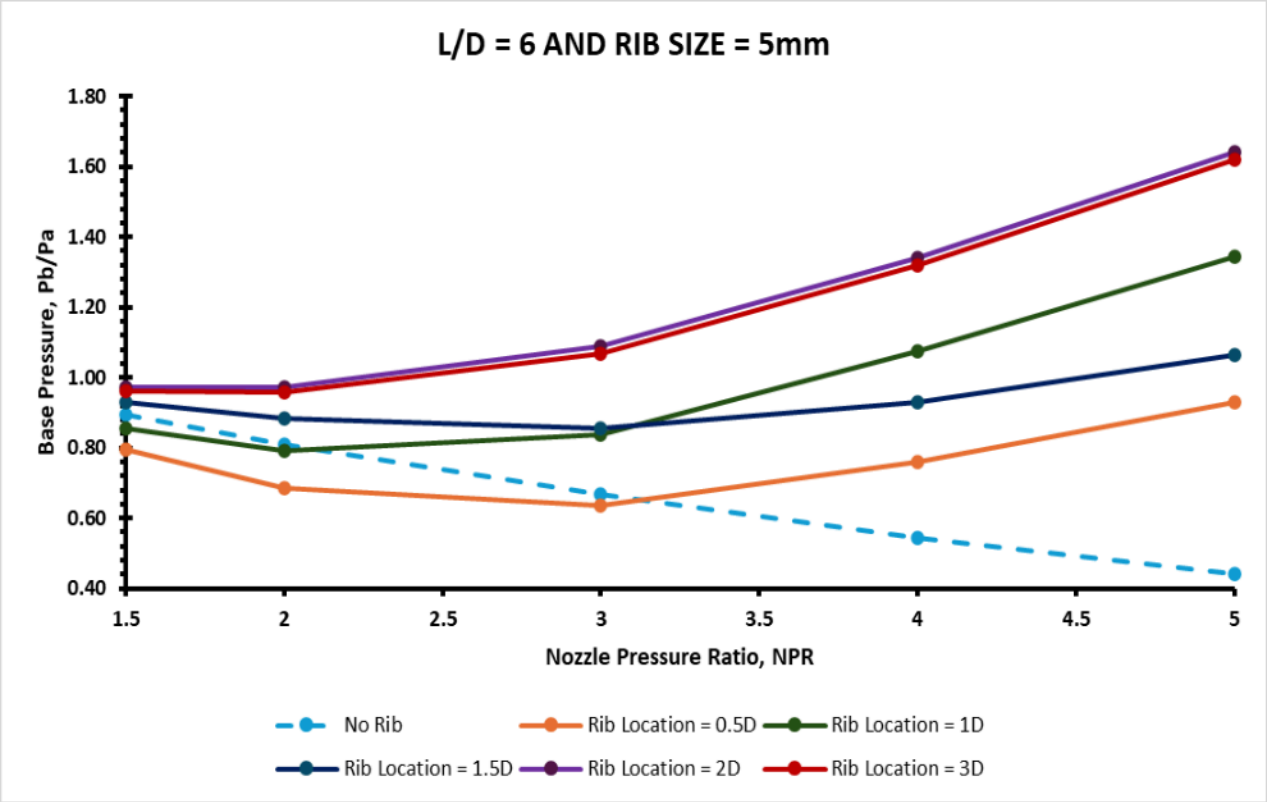

(c)

Fig. 22. Base pressure vs. NPR for various rib locations for duct length L = 6D

4.5 Sample of Contours

In this chapter, only a few samples of contour are discussed. Other contours were not considered for discussion in this paper as they exhibit a similar trend to the contour discussed below.

4.5.1 Velocity contours for rib orientation 1

Figure 23 shows the velocity contour of fluid flow along a converging expansion into a circular duct with a rib size of 3 mm at the nearest location from the base wall. The contour plots' colours represent the magnitude of the fluid flow's velocity. Blue indicates the low-velocity region, green and yellow represent the moderate-velocity region, and red indicates the high-velocity region. At lower NPR, the flow is relatively slow throughout the duct. The high-velocity region is concentrated downstream of the nozzle exit, gradually expanding into a lower-velocity field. Starting from NPR 3, the effect of the rib becomes noticeable, and the recirculation zone at the rib downstream is more defined. At the highest NPR 5, the recirculation and wake region behind the rib is very prominent and shows strong interaction with a high-velocity jet. As the NPR increases, the velocity of the flow also increases. The rib causes flow separation at higher NPR and creates a wake region. Higher NPR produced a stronger jet with less spreading compared to lower NPR. The presence of ribs modifies the flow field in terms of velocity due to the obstruction created towards the flow reattachment downstream.

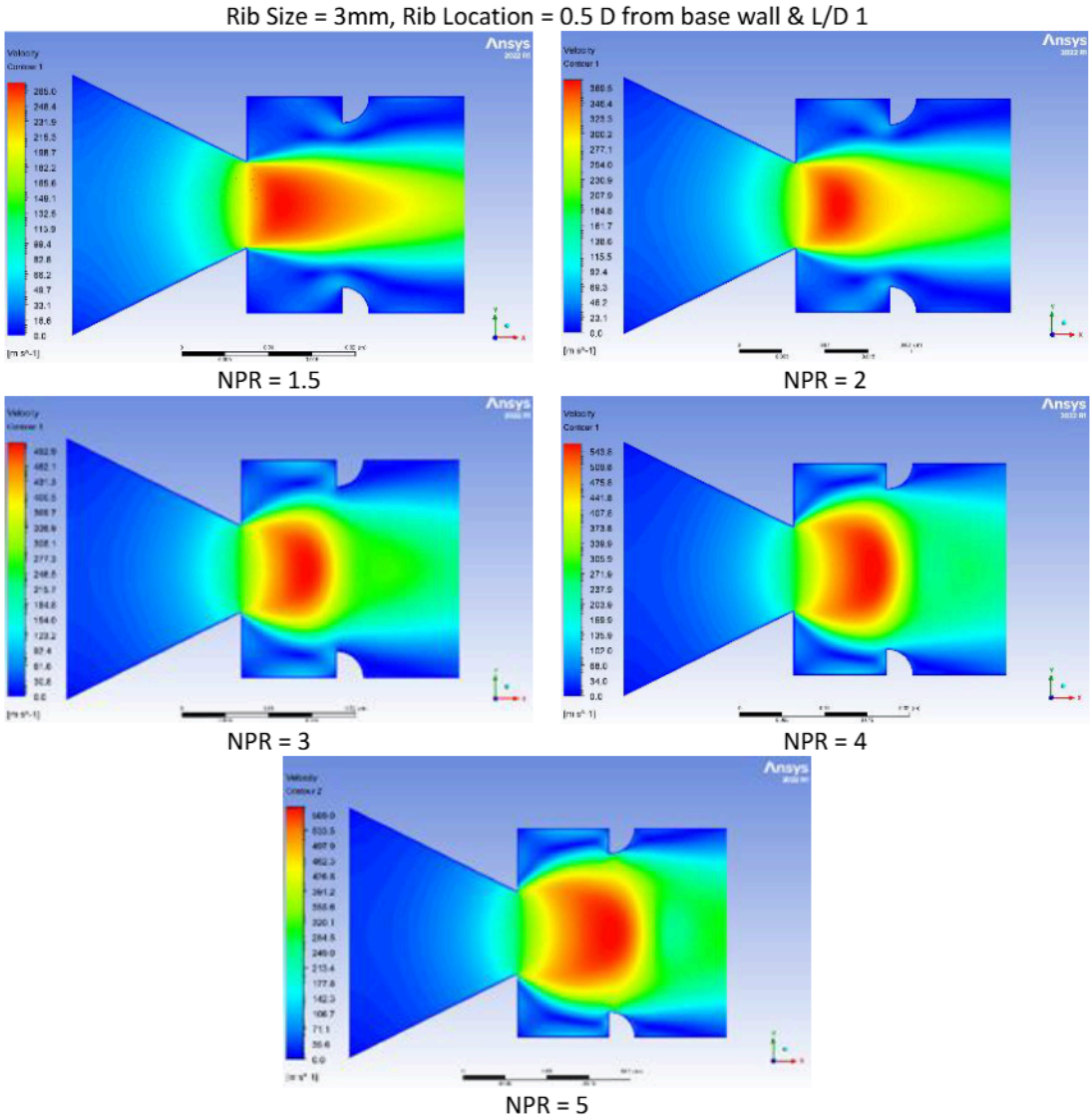

Fig. 23. Velocity contours for the model with a 3 mm rib at orientation one and 1D location

Figure 24 is the same model but with a bigger rib size of 5 mm. As the NPR increases, the flow accelerates more significantly. The rib does influence the velocity distribution even at the lowest NPR. The flow is forced to accelerate due to the reduced cross-sectional area between the ribs. As the NPR increases, the velocity is highly energized and distributed across the duct. The velocity further increases, and the high-velocity region extends downstream even further. Starting from NPR 3, the contour shows more uniform areas and has better mixing. This phenomenon shows less flow separation and recirculation.

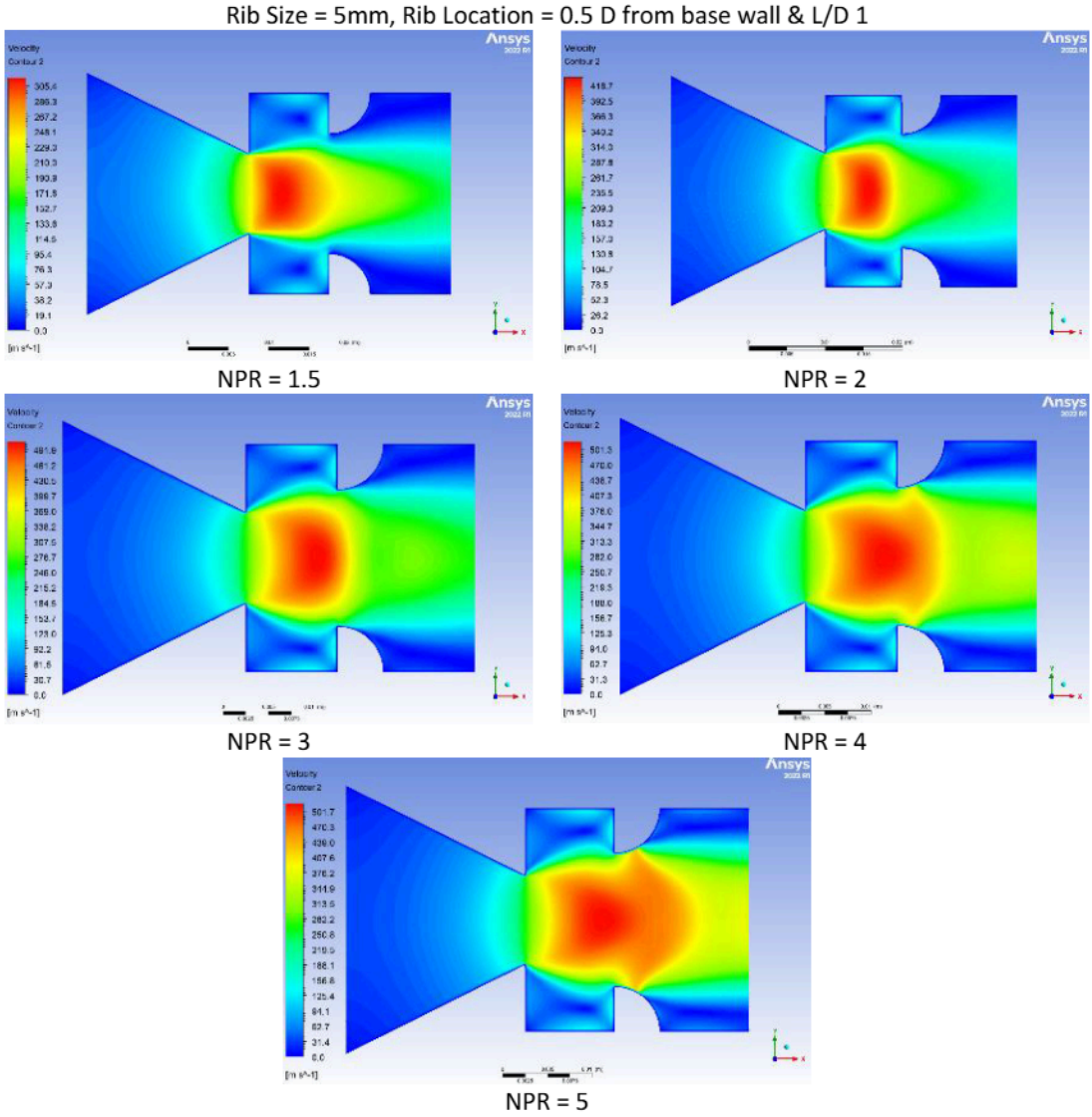

Fig. 24. Velocity contours for the model with a 5mm rib at orientation one and 1D location

Figure 25 shows the model with a 3 mm rib at the furthest location from the base wall. As the NPR increases from 1.5 to 5, the velocity in the duct also increases. The expansion of the high-velocity regions can be seen through colour changes from yellow to red. The flow pattern remains similar across different NPRs, with the primary difference being the magnitude in the high-velocity regions. Higher NPR values indicate more efficient pressure conversion into kinetic energy, resulting in the high-velocity areas.

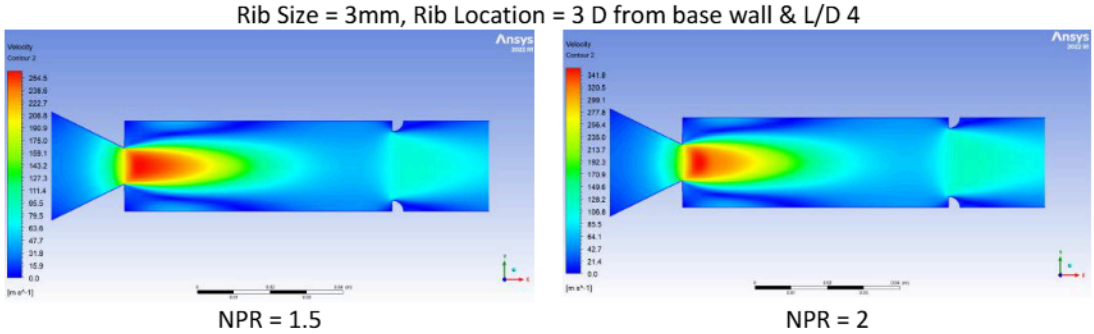

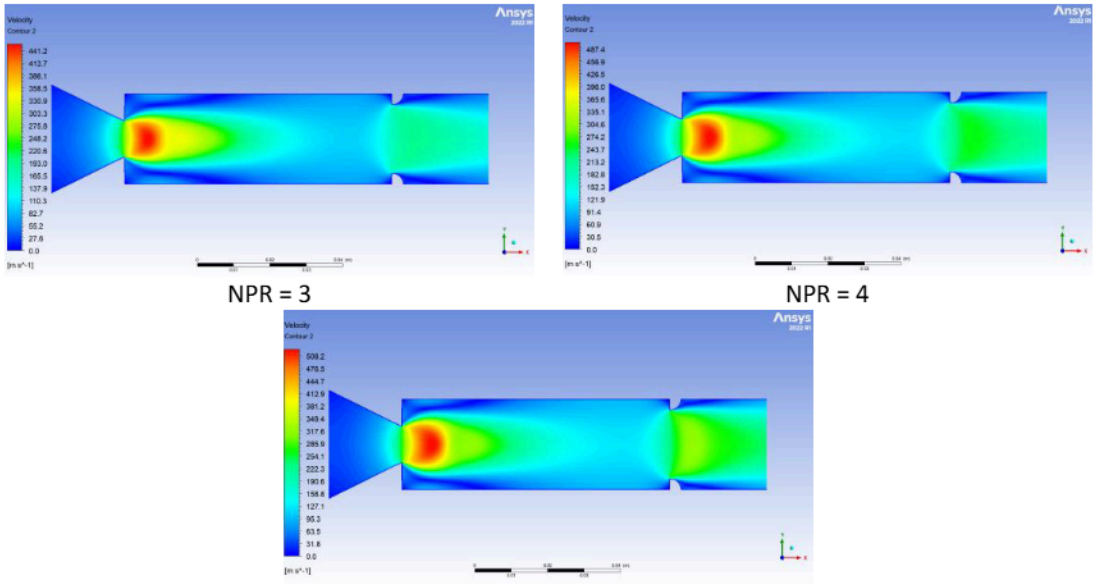

Fig. 25. Velocity contours for the model with a 3mm rib at orientation one and 4D location

Figure 26 shows the model with the most significant rib size (5 mm) and the furthest location from the base wall. For NPR 1.5, the flow is subsonic as the flow decelerates downstream of the rib. At NPR 2 and 3, the flow expansion becomes more pronounced, and the pressure drop becomes significant downstream of the rib. The flow becomes supersonic for NPR values of 4 and above, exhibiting more substantial expansion and higher velocities downstream of the rib. The flow dynamics differ for subsonic and supersonic flows.

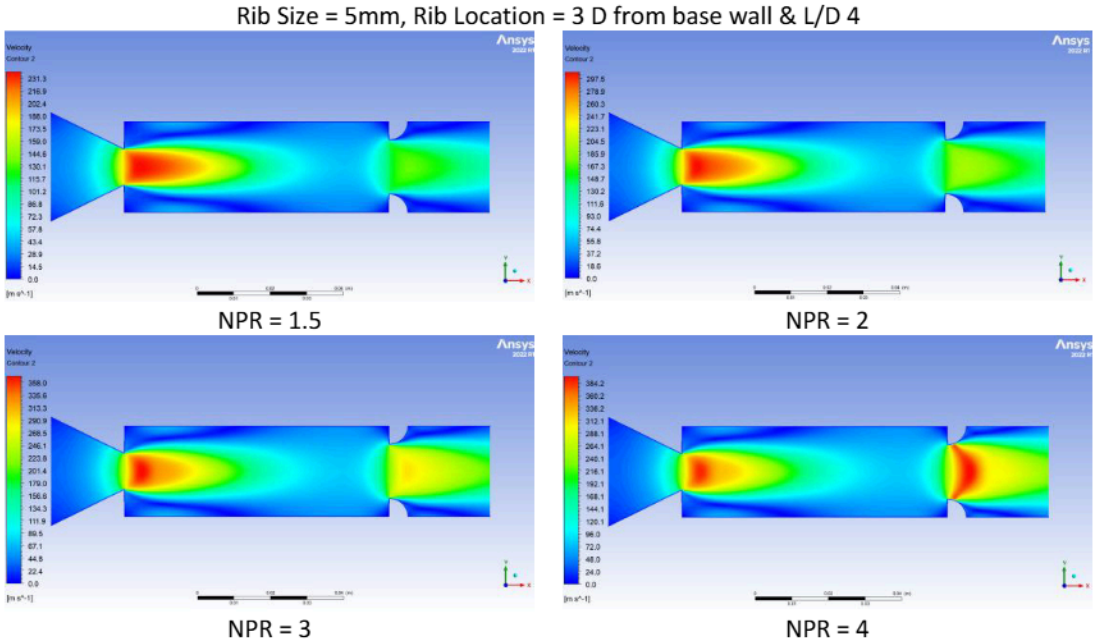

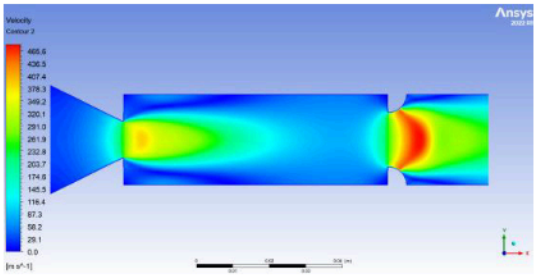

NPR = 5

Fig. 26. Velocity contours for the model with a 5mm rib at orientation one and 4D location

4.5.2 Pressure contours for rib orientation 1

Figures 27 to 30 show the pressure contours for the model with different rib sizes and locations. The red regions represent areas of higher pressure, while the blue areas represent areas of lower pressure. The presence of the rib can cause flow separation and reattachment, which in turn influence the pressure distribution and jet formation. The larger the rib size, the more the flow reattachment point and pressure downstream of the rib will be affected. Then, the further the rib location, the higher the pressure value before the rib placement will be than the rib placement nearer to the base wall.

Rib Size = 3mm, Rib Location = 0.5 D from base wall & L/D 1

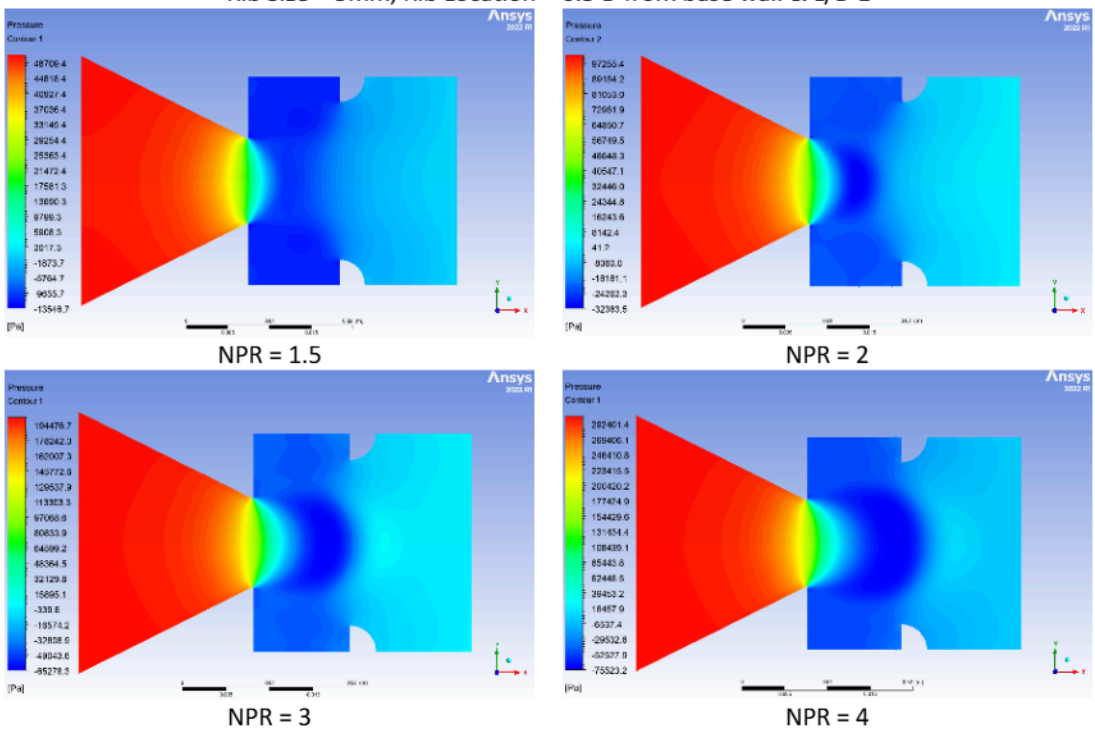

NPR = 1.5 NPR = 2

NPR = 3 NPR = 4

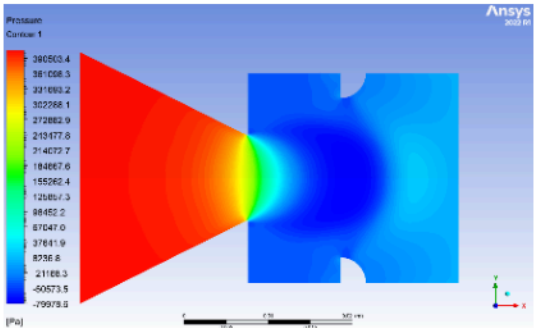

NPR = 5

Fig. 27. Pressure contours for the model with a 3mm rib at orientation one and 1D location

Rib Size = 5mm, Rib Location = 0.5 D from base wall & L/D 1

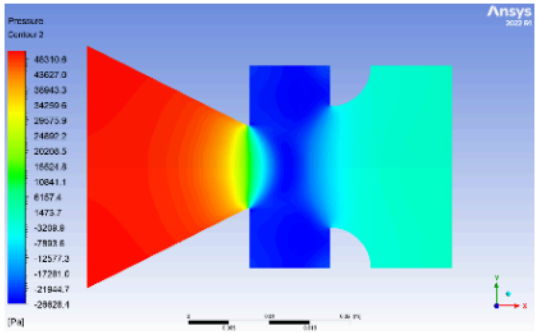

NPR = 1.5

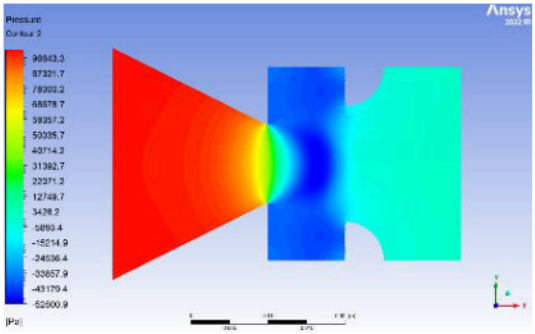

NPR = 2

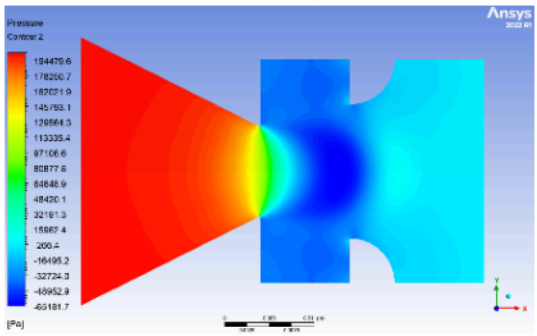

NPR = 3

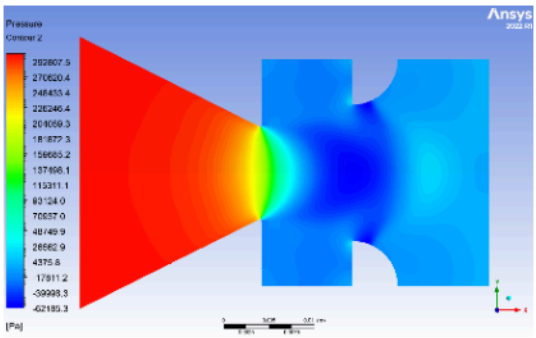

NPR = 4

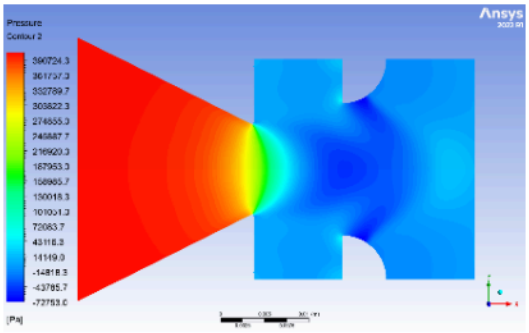

NPR = 5

Fig. 28. Pressure contours for the model with a 5mm rib at orientation one and 1D location

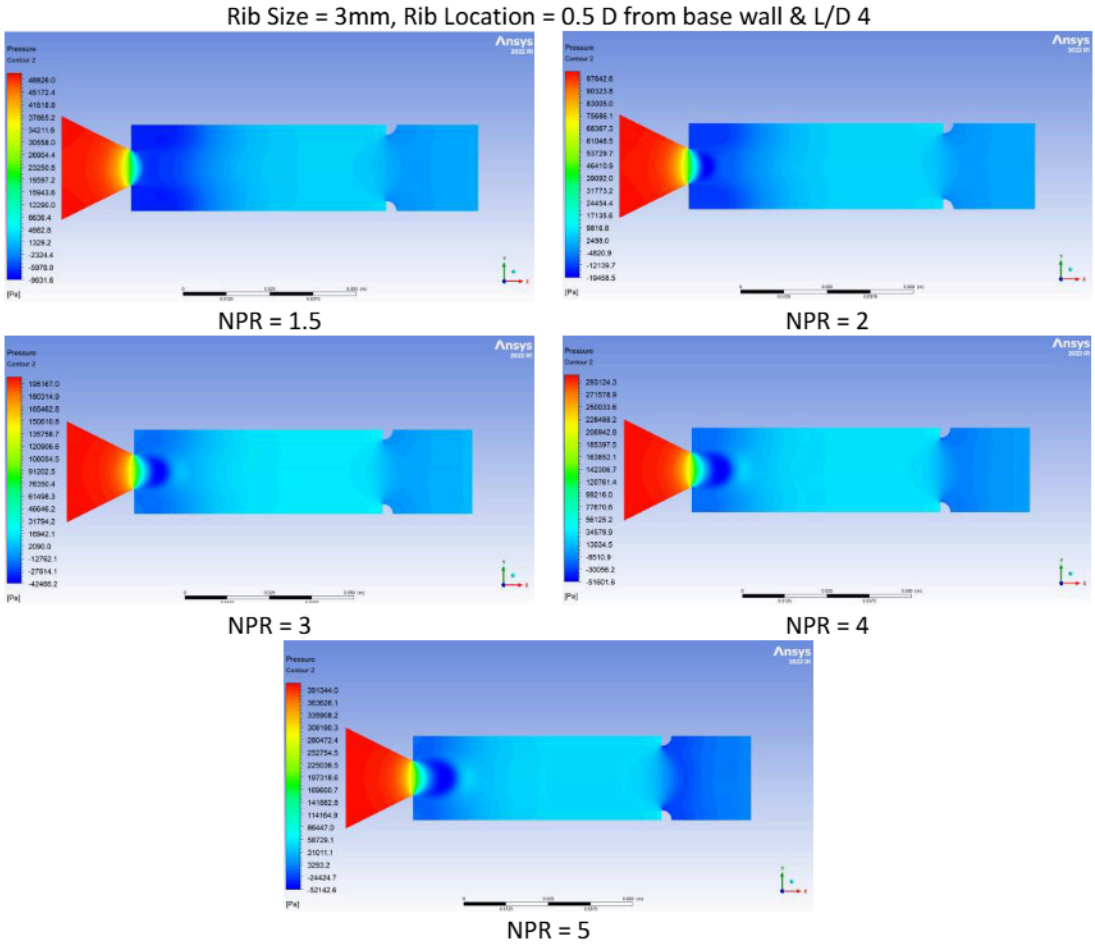

Fig. 29. Pressure contours for the model with a 3mm rib at orientation one and 4D location

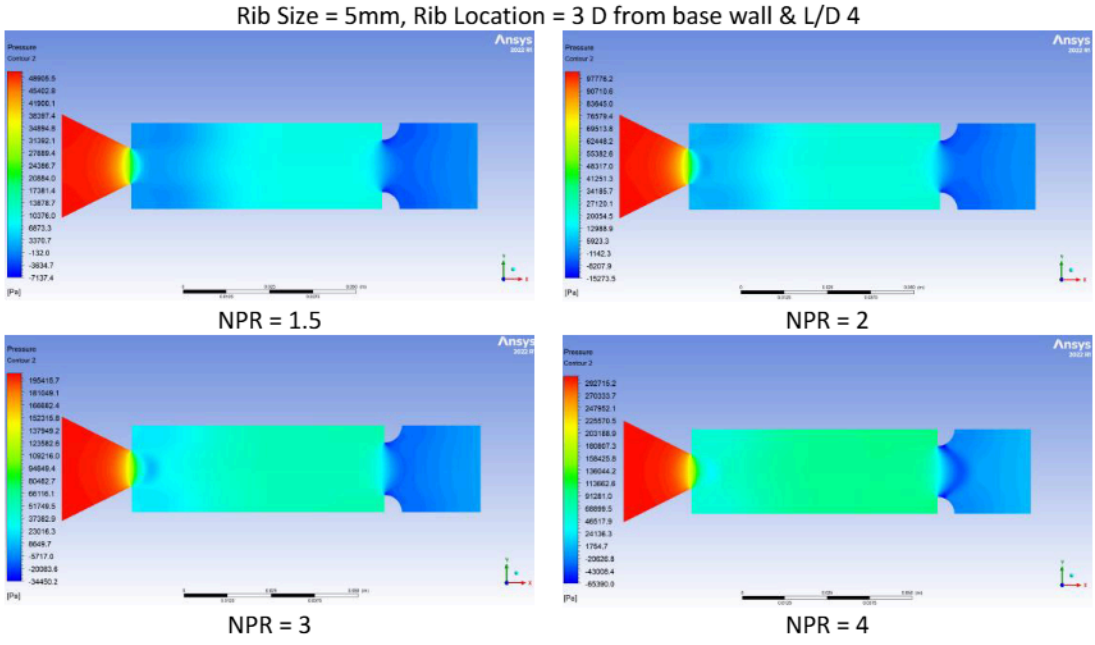

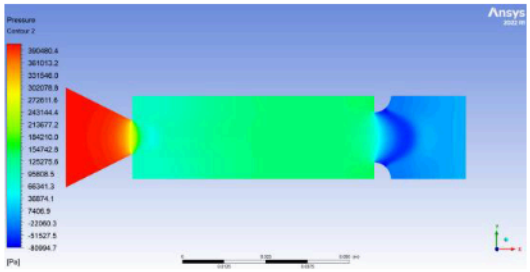

NPR = 5

Fig. 30. Pressure contours for the model with a 5mm rib at orientation one and 4D location

4.5.3 Streamline for rib orientation 1

Figures 31 to 34 show the streamline pattern of the model. The streamlines indicate the velocity flow. The explanation is the same as discussed earlier.

Rib Size = 3mm, Rib Location = 0.5 D from base wall & L/D 1

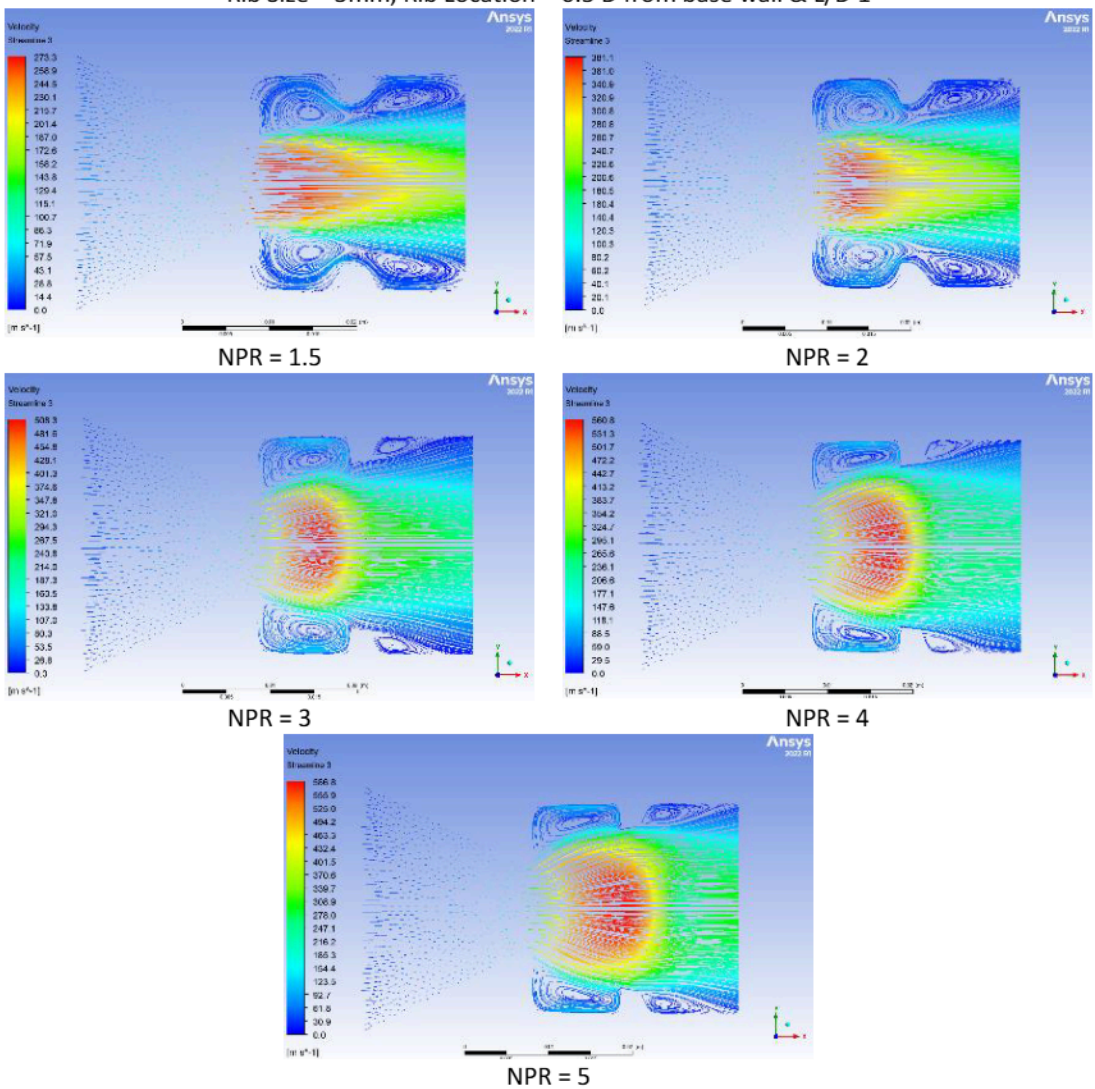

NPR = 1.5 NPR = 2

NPR = 3 NPR = 4

NPR = 5

Fig. 31. Streamlines for the model with a 3mm rib at orientation one and 1D location

Rib Size = 5mm, Rib Location = 0.5 D from base wall & L/D 1

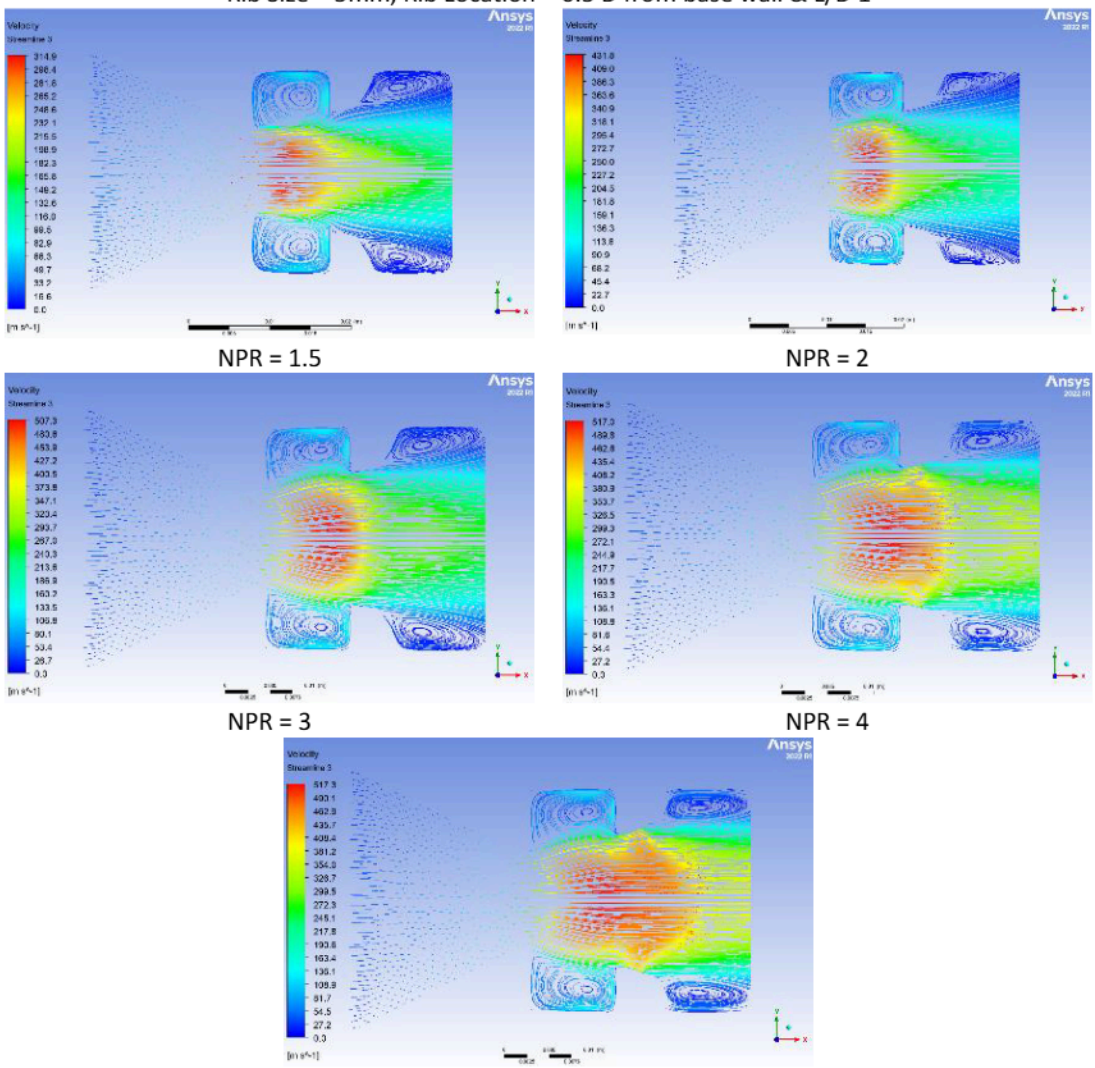

NPR = 1.5 NPR = 2

NPR = 3 NPR = 4

NPR = 5

Fig. 32. Streamline for the model with a 5mm rib at orientation one and 1D location

Rib Size = 3mm, Rib Location = 0.5 D from base wall & L/D 4

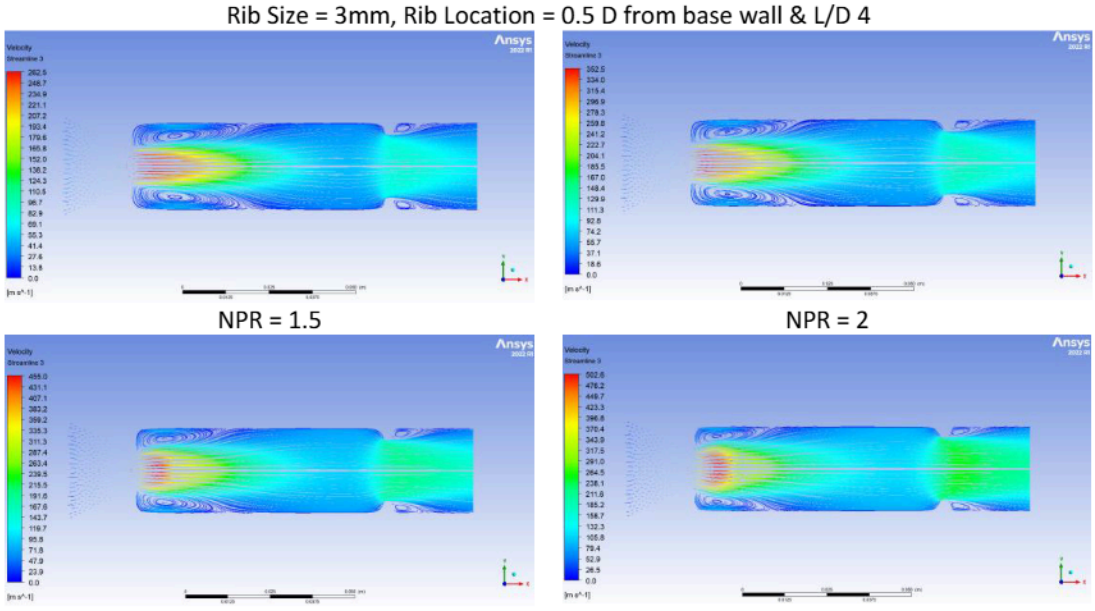

NPR = 1.5 NPR = 2

NPR = 3 NPR = 4

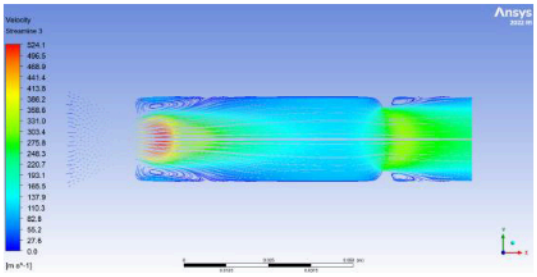

NPR = 5

Fig. 33. Streamlines for the model with a 3mm rib at orientation one and 4D location

Rib Size = 5mm, Rib Location = 3 D from base wall & L/D 4

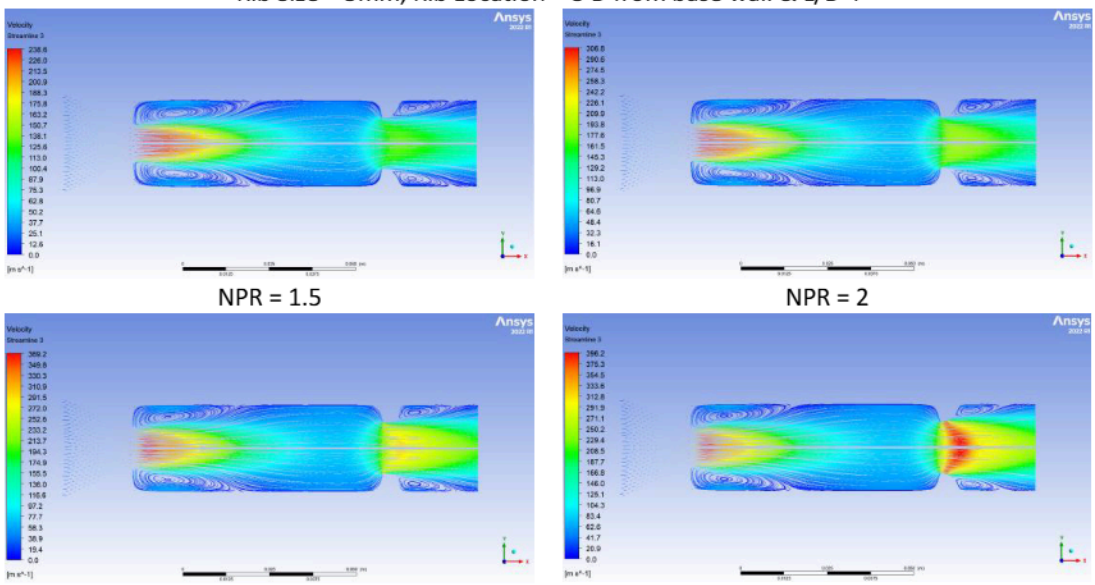

NPR = 1.5 NPR = 2

NPR = 3 NPR = 4

NPR = 5

Fig. 34. Streamlines for the model with a 5mm rib at orientation one and 4D location

4.5.4 Velocity contours for rib orientation 2

Figures 35 and 36 show the velocity contour for a model with different rib sizes at the nearest location from the base wall.

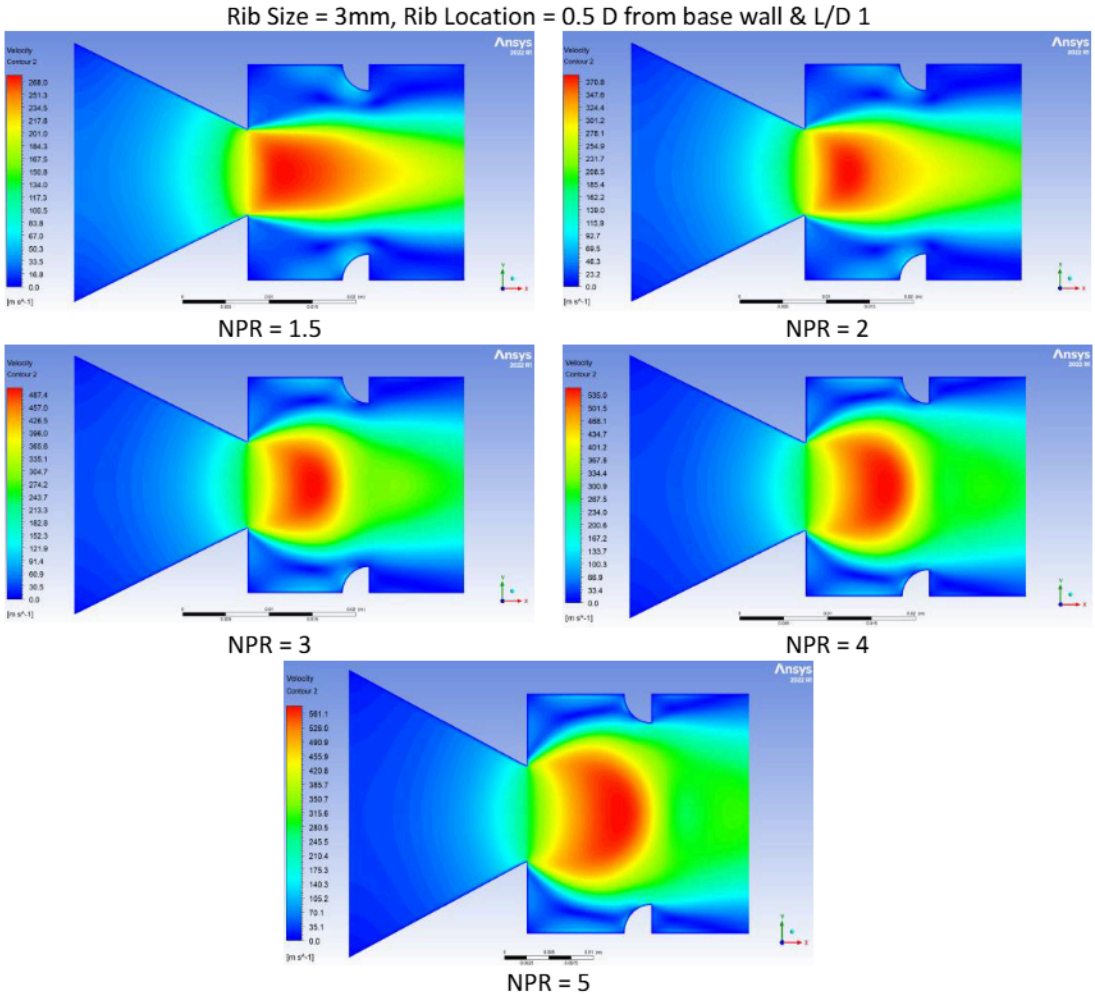

Fig. 35. Velocity contours for the model with a 3mm rib at orientation two and 1D location

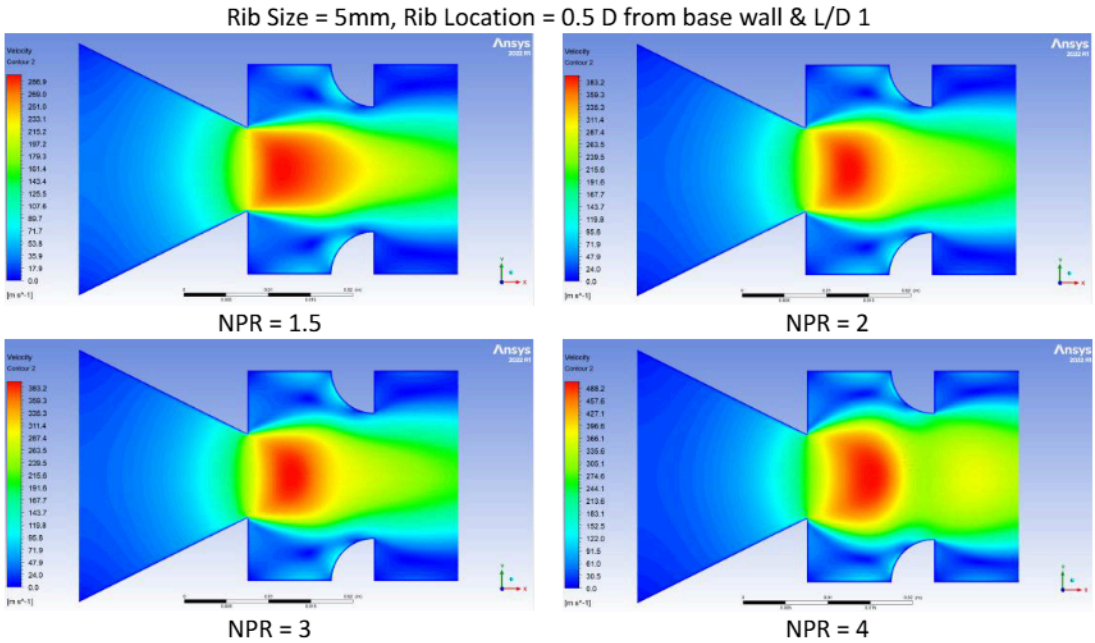

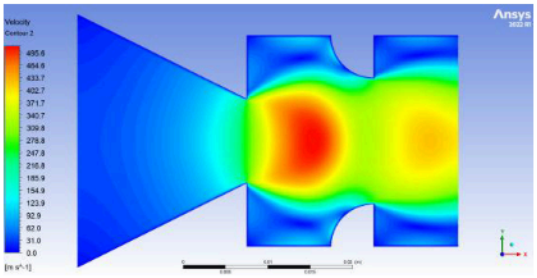

NPR = 5

Fig. 36. Velocity contours for the model with a 5mm rib at orientation two and 1D Location

Figure 37 and Figure 38 show the rib location at the furthest location from the base wall. The difference between these figures and previous figures is only in rib orientation. As the NPR increases, the high-velocity region within the nozzle expands. The velocity gradient also becomes steeper as it approaches the base wall. The presence of rib curvature influences the flow distribution and alters the velocity contours as the NPR varies.

Rib Size = 3mm, Rib Location = 3D from base wall & L/D 4

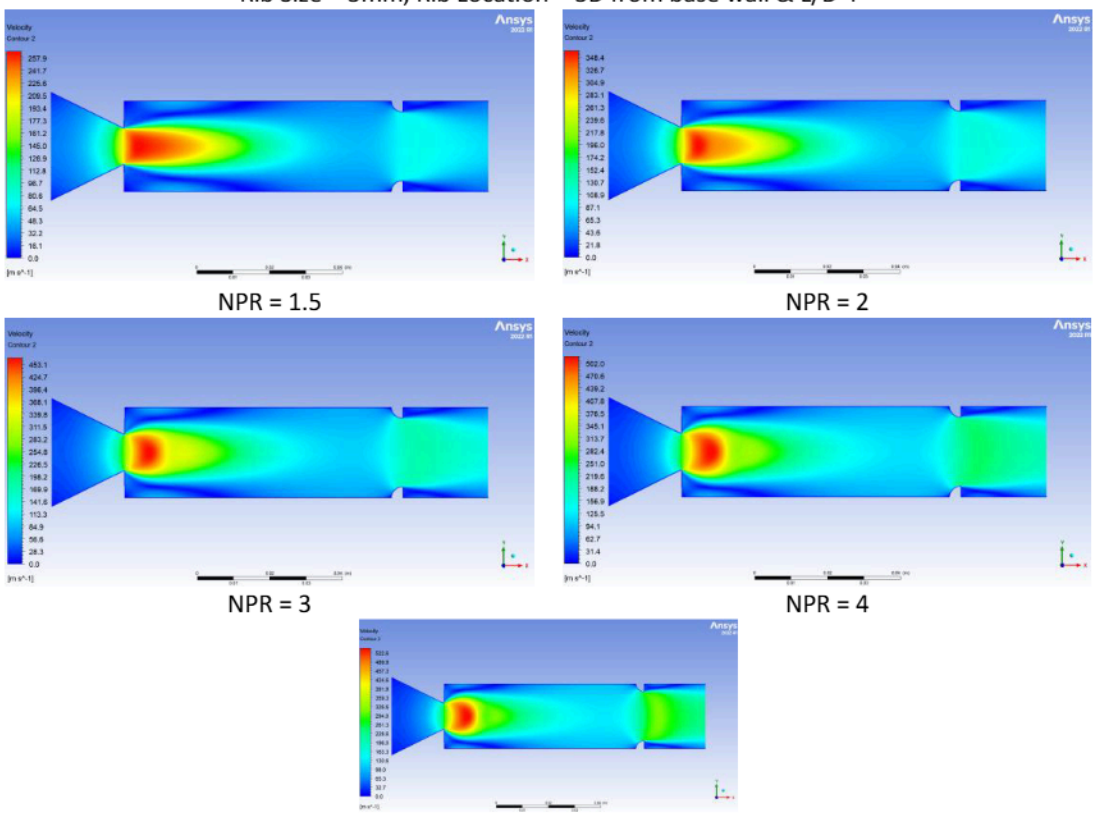

NPR = 1.5 NPR = 2

NPR = 3 NPR = 4

NPR = 5

Fig. 37. Velocity contours for the model with a 3mm rib at orientation two and 4D location

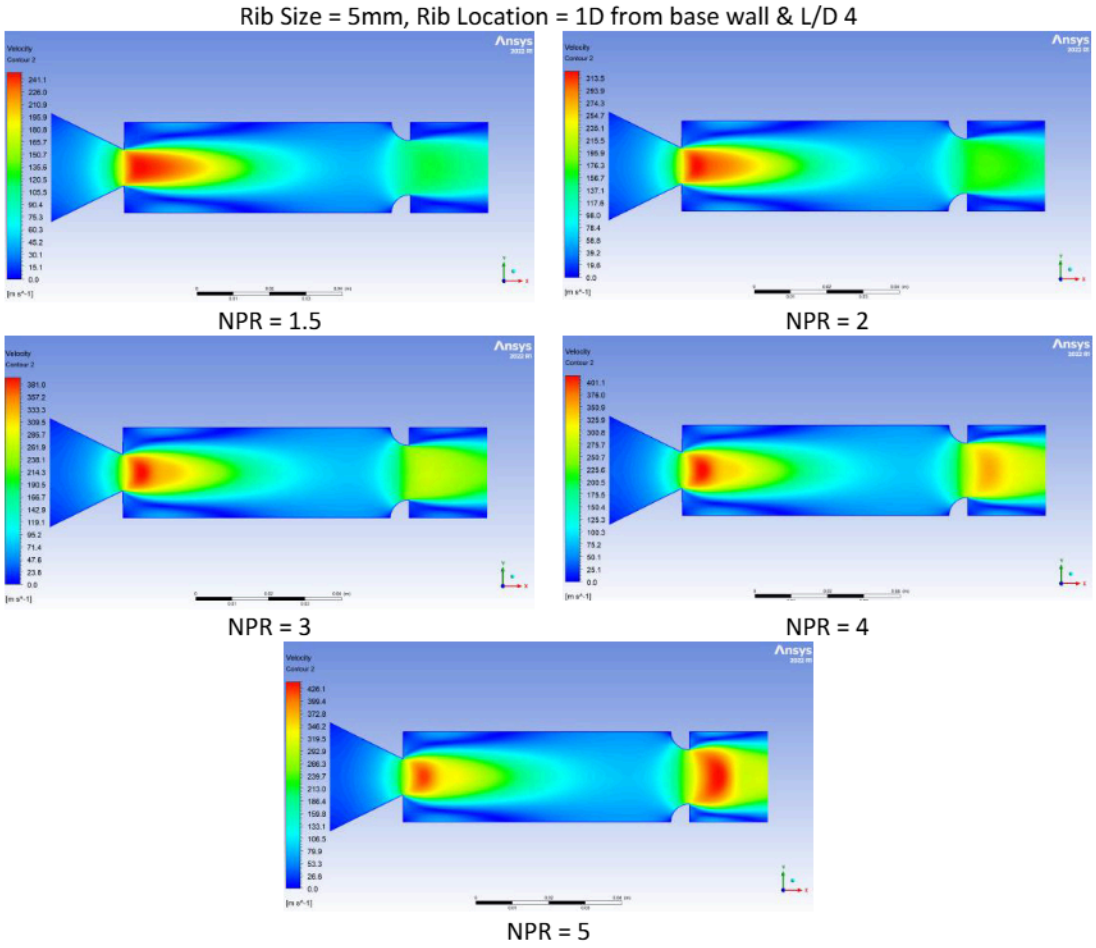

Fig. 38. Velocity contours for the model with a 5mm rib at orientation two and 4D location

4.5.5 Pressure contours for rib orientation 2

Figures 39 to 42 show the pressure contours for various NPRs with a 5 mm rib radius. The contour shows a high-pressure zone closer to the nozzle exit at lower NPR values. The high-pressure zones, indicated by steeper pressure gradients, show less jet expansion. For higher NPR, the higher-pressure zones extend further from the nozzle—a gradual transition from high to low pressure results in a more significant jet expansion.

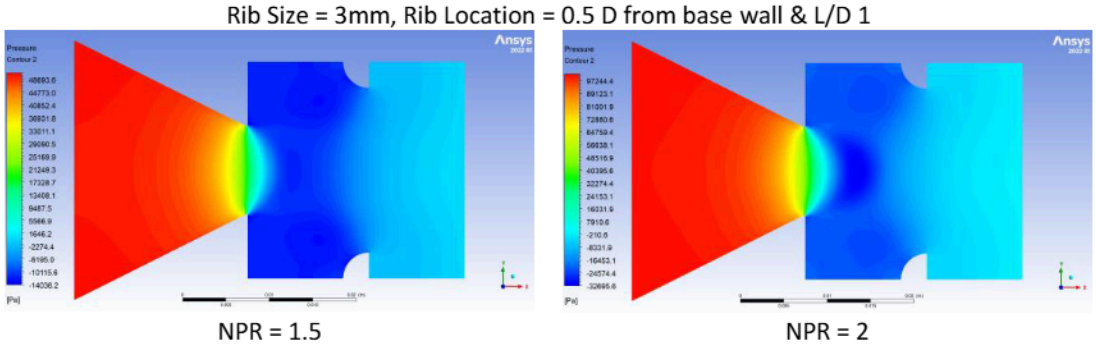

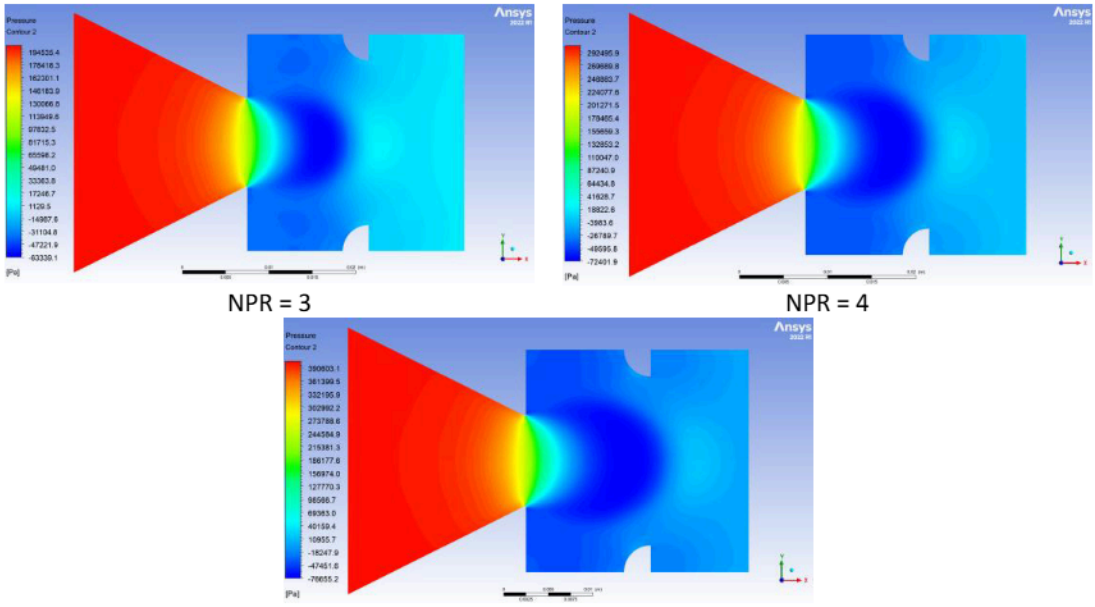

Fig. 39. Pressure contours for the model with a 3mm rib at orientation two and 1D Location

Rib Size = 5mm, Rib Location = 0.5D from base wall & L/D 1

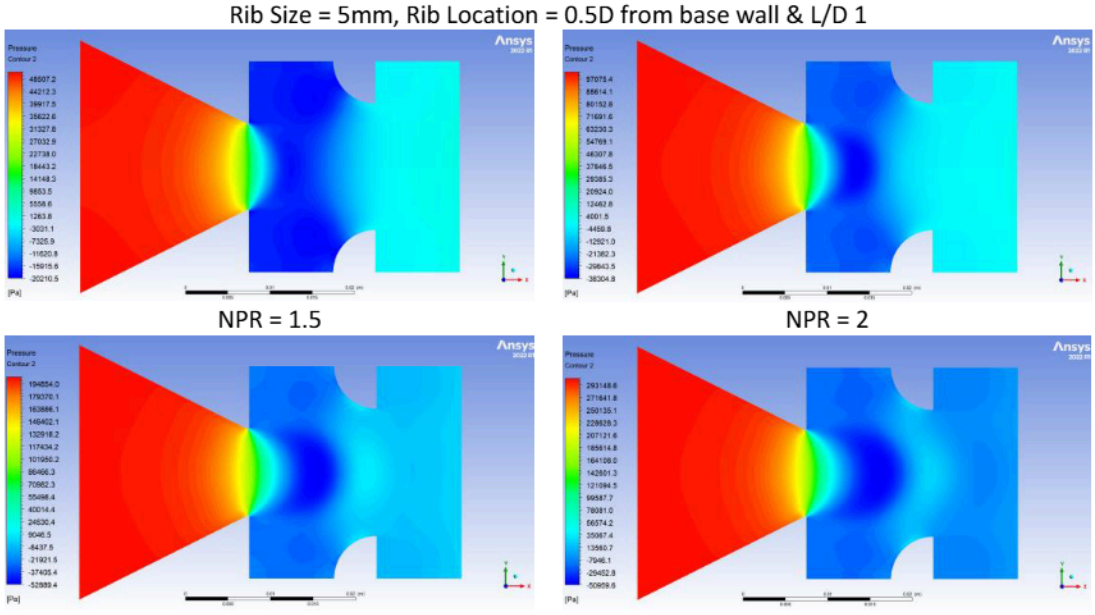

Fig. 40. Pressure contours for the model with a 5mm rib at orientation two and 1D location

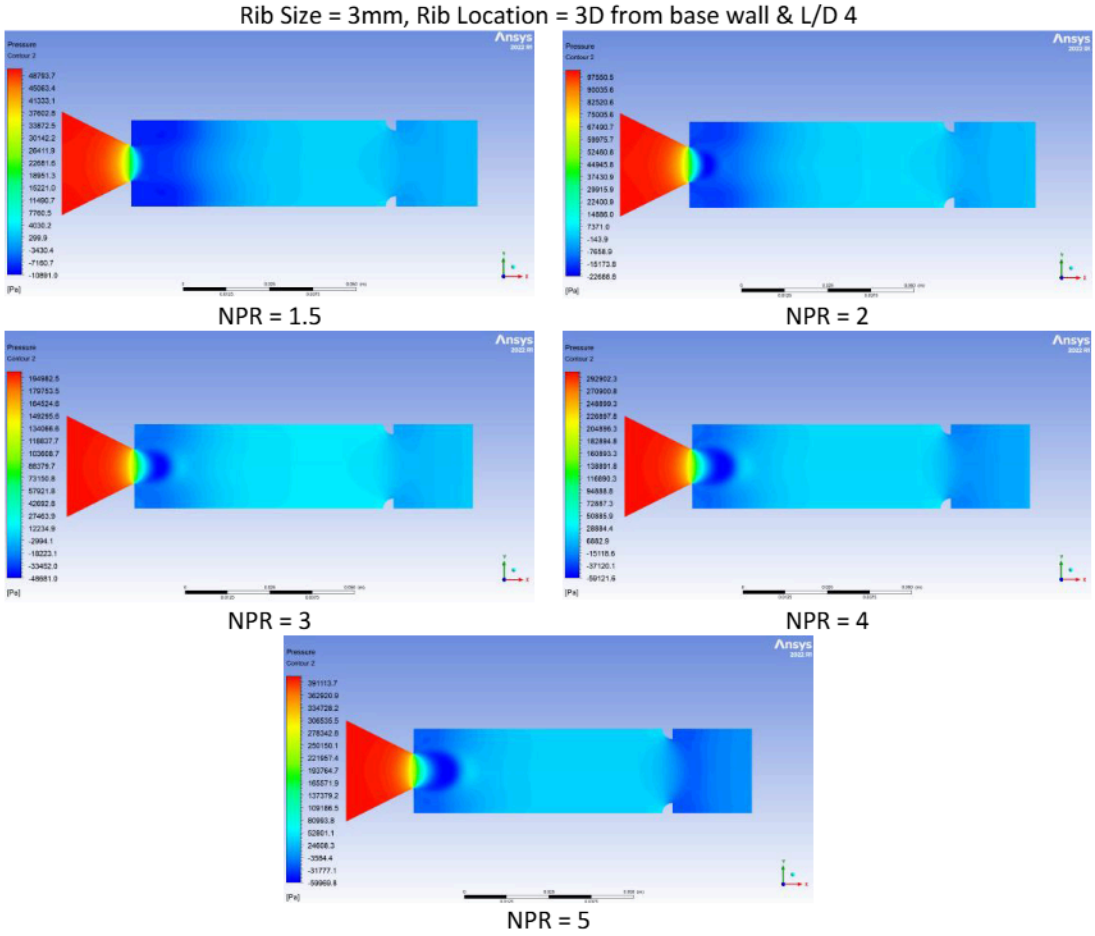

Fig. 41. Pressure contours for the model with a 3mm rib at orientation two and 4D location

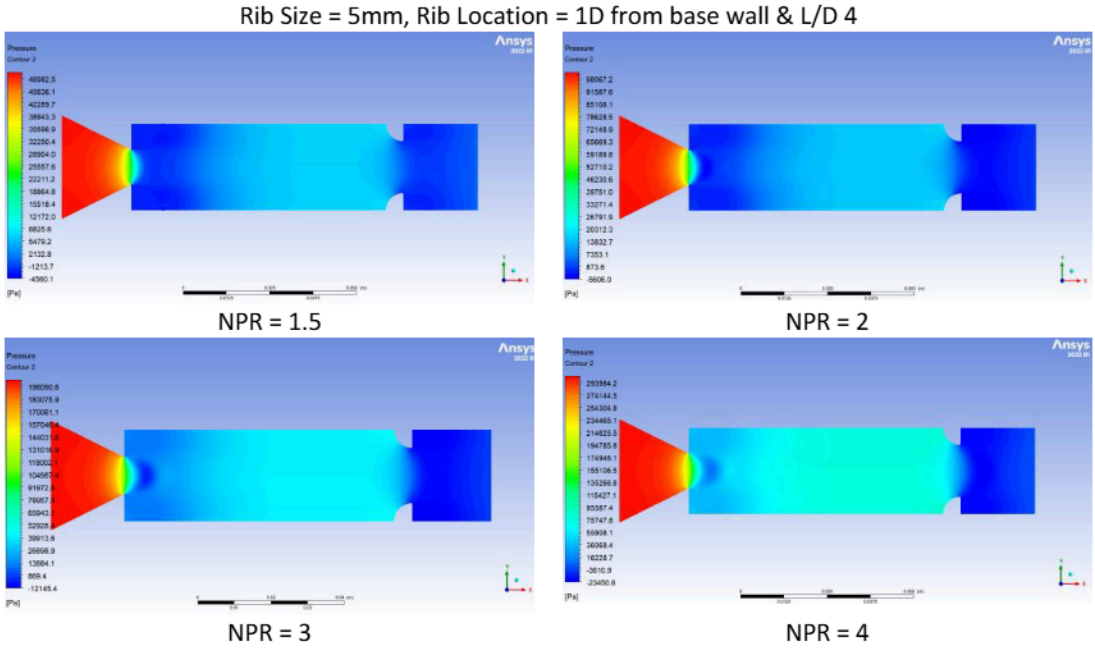

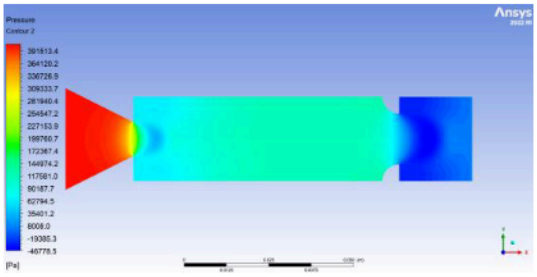

NPR = 5

Fig. 42. Pressure contours for the model with a 5 mm rib at orientation two and 4D location

4.5.6 Streamline for rib orientation 2

Figures 43 to 46 represent the same variable, the velocity of a fluid, but they illustrate it differently in terms of flow and streamlines.

Rib Size = 3mm, Rib Location = 0.5 D from base wall & L/D 1

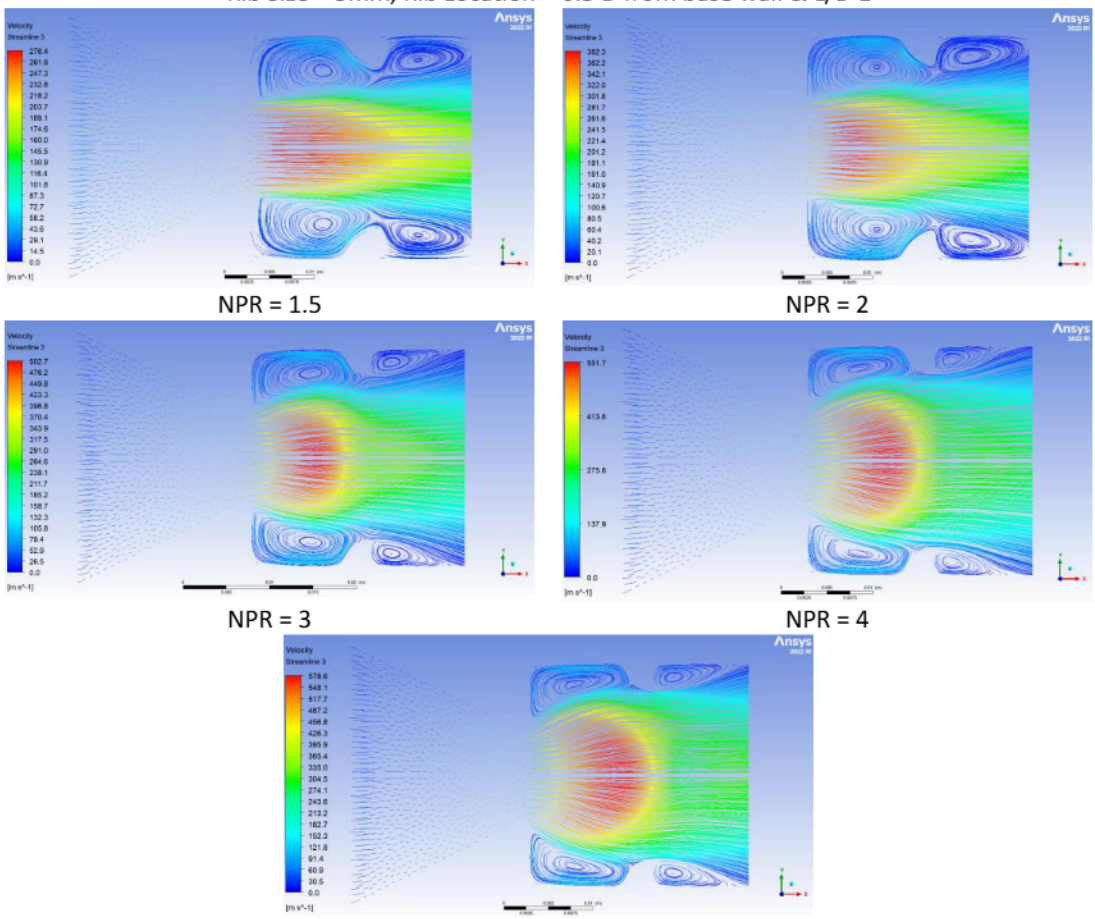

NPR = 1.5 NPR = 2

NPR = 3 NPR = 4

NPR = 5

Fig. 43. Streamline for the model with a 3mm rib at orientation two and 1D location

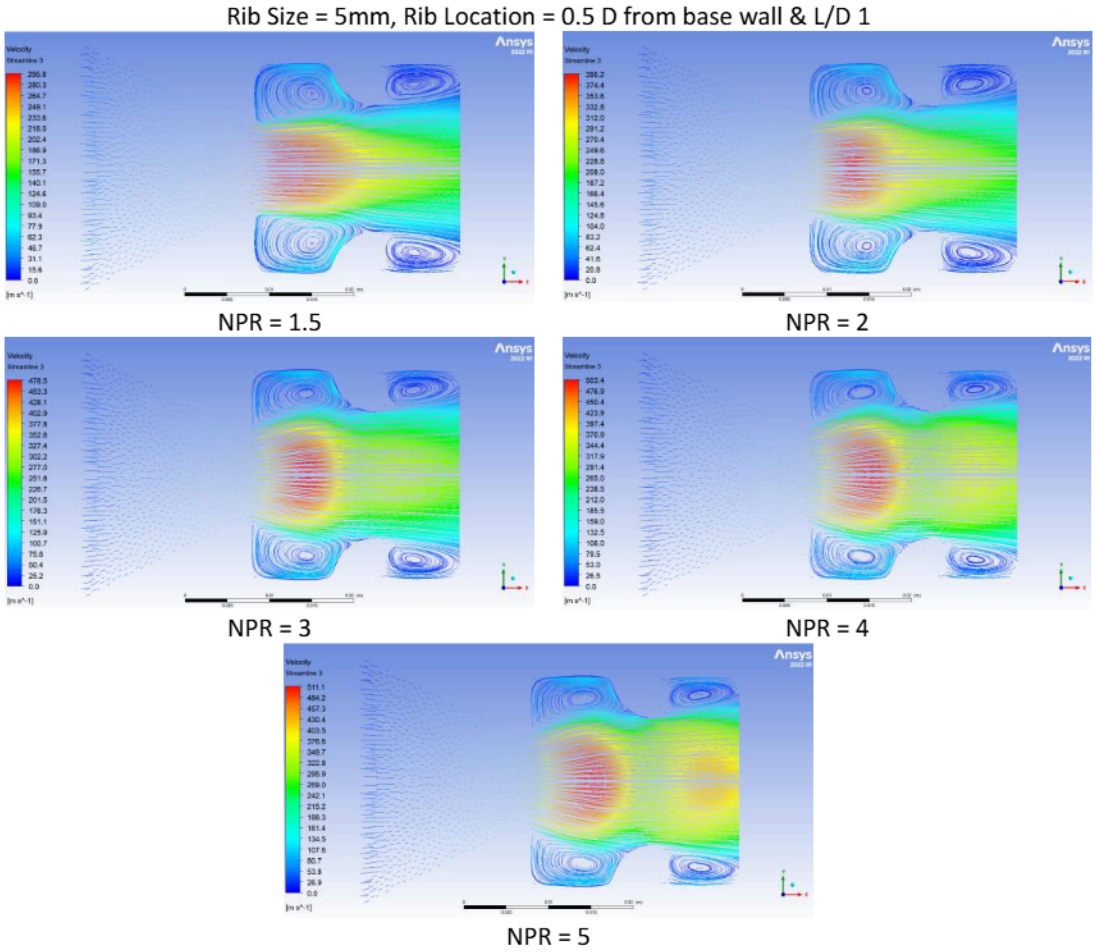

Fig. 44. Streamline for the model with a 5mm rib at orientation two and 1D location

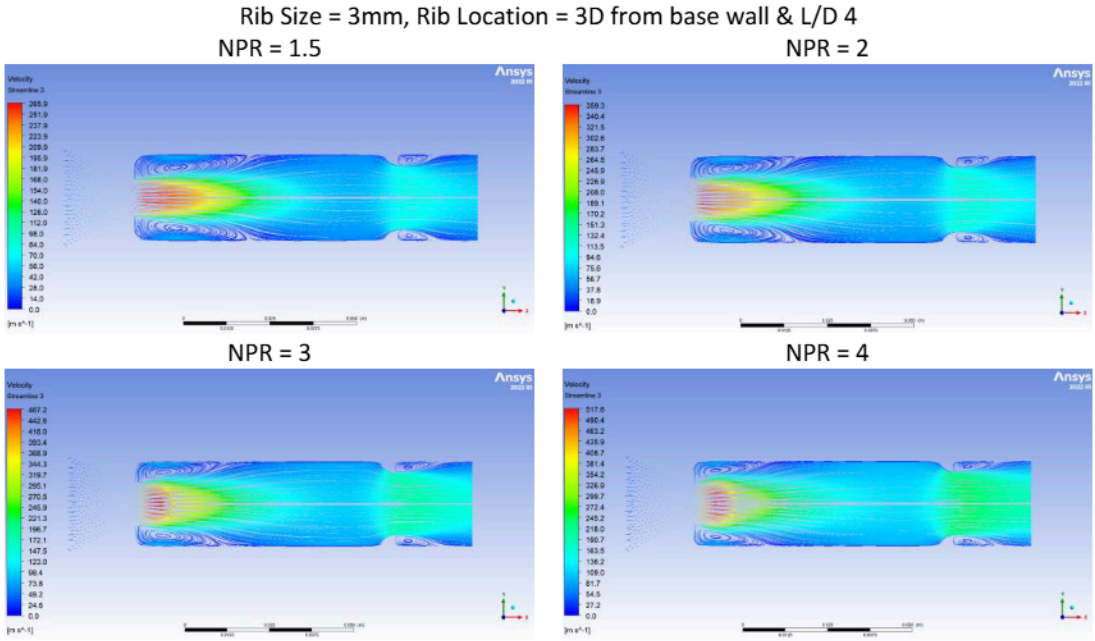

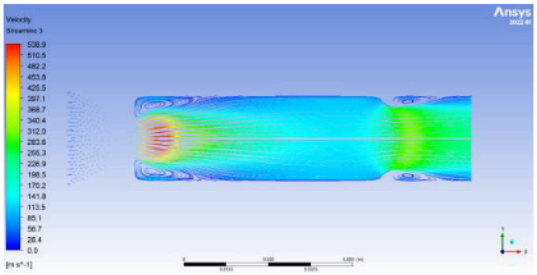

NPR = 5

Fig. 45. Streamline for the model with a 3mm rib at orientation two and 4D location

Rib Size = 5mm, Rib Location = 1D from base wall & L/D 4

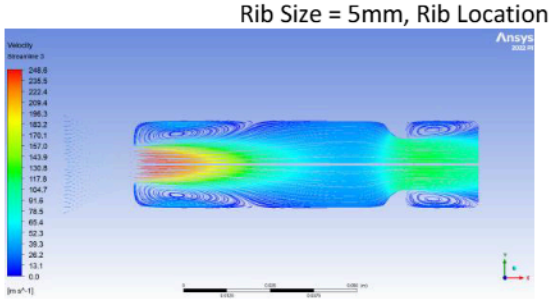

NPR = 1.5

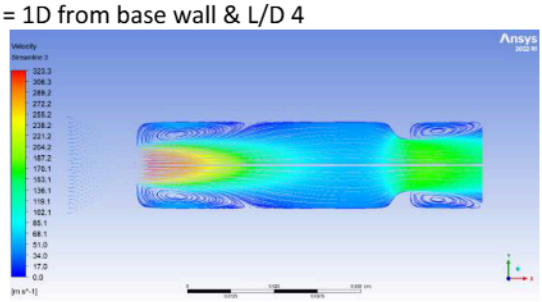

NPR = 2

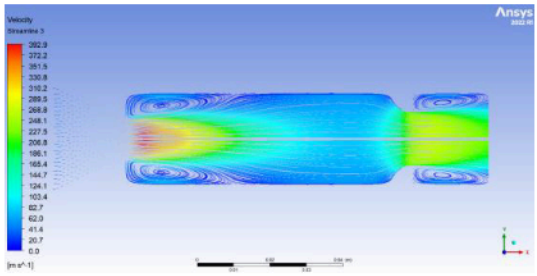

NPR = 3

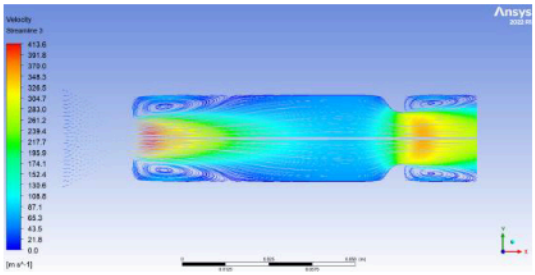

NPR = 4

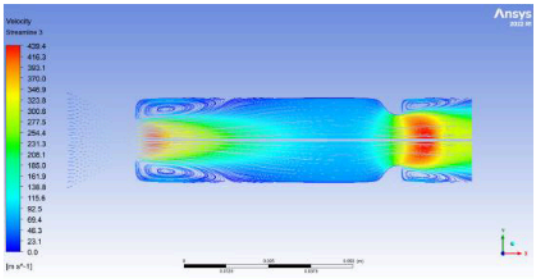

NPR = 5

Fig. 46. Streamline for the model with a 5mm rib at orientation two and 4D location.

5. Conclusion

In conclusion, the rib radii affect the strength of the vortex and shock wave. The interaction of the shear layer with the curved wall of ribs, where slopes change gradually, results in modest vortex strength, leading to a lower impact on base pressure compared to other orientations in which the flat wall faces the base wall. For ribs with lower radii, the rib curvature has a significant influence on the efficacy of passive control at NPRs 2.5, 3, and 4. Ribs with flat surfaces facing the base wall resulted in a consistent increase in base pressure. These results across various duct lengths suggest limited Mach wave formation and minimizing variations in base pressure. The rib design characteristics, especially curvature, are essential in optimizing flow control within duct systems. The rib orientation affects shear layer interaction, which is crucial for designing effective control

measures to manipulate base pressure. Then, comparing the rib location from the base wall reveals significant insights into flow control mechanisms and aerodynamic behavior by examining the influence of rib size, placement, and duct length on base pressure in the flow system. The more prominent ribs generally lead to increased base pressure, with this effect becoming more pronounced as the rib radius increases. The location of ribs relative to the base region and the nozzle exit plays a crucial role in determining their effectiveness in altering base pressure. The presence of ribs can also reverse the declining trend in base pressure at specific NPRs. Optimizing rib design and placement for desired base pressure modifications is essential for enhancing the performance and efficiency of various engineering application systems.

6. Scope for Future Work

Based on this study, it is recommended that future studies focus on lower area ratios. It is expected that at lower area ratios, the passive control will be more effective. Also, one can study at supersonic Mach numbers. It is also suggested that one study used a hybrid regulation of the base pressure and combined two passive controls, such as ribs and cavities.

Acknowledgement
This research was not funded by any grant.

References
[1] Rathakrishnan, E. 2001. "Effect of Ribs on Suddenly Expanded Flows." AIAA Journal 39 (7): 1402–1404.
[2] Rathakrishnan, E. 1999. "Effect of Splitter Plate on Bluff Body Drag." AIAA Journal 37 (9): 1125–1126. https://doi.org/10.2514/2.823.
[3] Baig, M. A. A., S. A. Khan, Al-Mufadi, Fahad, and E. Rathakrishnan. 2011. "Control of Base Flows with Microjets." International Journal of Turbo Jet Engines 28 (1): 59–69. https://doi.org/10.1515/TJJ.2011.009.
[4] Rathakrishnan, E. 2015. "Base Pressure Control by Using Ribs in Subsonic and Sonic Suddenly Expanded Flows." AIAA Conference Proceedings.
[5] Vijayaraja, K., C. Senthilkumar, S. Elangovan, and E. Rathakrishnan. 2014. "Base Pressure Control with Annular Ribs." International Journal of Turbo Jet Engines 31 (2): 111–118. https://doi.org/10.1515/tjj-2013-0037.
[6] Sethuraman, V., P. Rajendran, S. A. Khan, A. Aabid, and M. Baig. 2024. "Control of Nozzle Flow Using Rectangular Ribs at Sonic and Supersonic Mach Numbers." Fluid Dynamics and Materials Processing. https://doi.org/10.32604/fdmp.2024.049441.
[7] Sethuraman, V., P. Rajendran, and S. A. Khan. 2020. "Base and Wall Pressure Control Using Cavities and Ribs in Suddenly Expanded Flows – An Overview." Journal of Advanced Research in Fluid Mechanics and Thermal Science 66 (1): 120–134.
[8] Khan, A., S. A. Khan, V. Raja, A. Aabid, and M. Baig. 2024. "Effect of Ribs in a Suddenly Expanded Flow at Sonic Mach Number." Heliyon 10 (9): e30313. https://doi.org/10.1016/j.heliyon.2024.e30313.
[9] Khan, A., A. Aabid, M. N. Akhtar, S. A. Khan, and M. Baig. 2025. "Supersonic Flow Control with Quarter Rib in a Duct: An Extensive CFD Study." International Journal of Thermofluids 26: 101060. https://doi.org/10.1016/j.ijft.2025.101060.
[10] Azami, M. H., M. Faheem, A. Aabid, I. Mokashi, and S. A. Khan. 2019. "Inspection of Supersonic Flows in a CD Nozzle Using an Experimental Method." International Journal of Recent Technology and Engineering 8 (2S3): 996–999.
[11] Pathan, K. A., P. S. Dabeer, and S. A. Khan. 2020. "Enlarge Duct Length Optimization for Suddenly Expanded Flows." Advances in Aircraft and Spacecraft Science 7 (3): 203–214.
[12] Khan, A., A. Aabid, S. A. Khan, M. N. Akhtar, and M. Baig. 2024. "Comprehensive CFD Analysis of Base Pressure Control Using Quarter Ribs in Sudden Expansion Duct at Sonic Mach Numbers." International Journal of Thermofluids 24 (October): 100908. https://doi.org/10.1016/j.ijft.2024.100908.
[13] Khan, A., S. A. Khan, M. N. Akhtar, A. Aabid, and M. Baig. 2024. "Base Pressure Control with Semi-Circular Ribs at Critical Mach Number." Fluid Dynamics and Materials Processing 22. https://doi.org/10.32604/fdmp.2024.049368.
[14] Khan, A., N. M. Mazlan, and E. Sulaeman. 2022. "Effect of Ribs as Passive Control on Base Pressure at Sonic Mach Numbers." CFD Letters 14 (1): 140–151. https://doi.org/10.37934/cfdl.14.1.140151.

[15] Hai-bo, and W.-q. Liu. 2012. "Influence of Cavity Length on Forward-Facing Cavity and Opposing Jet Combined Thermal Protection System Cooling Efficiency." International Journal of Aerospace and Mechanical Engineering.
[16] Heubner, L. D., and L. J. Utreja. 1993. "Mach 10 Bow Shock Behaviour of Forward-Facing Nose Cavity." Journal of Spacecraft and Rockets 30: 291–297. https://doi.org/10.2514/3.25513.
[17] Lorite, M., et al. 2017. "Drag Reduction of Slender Blunt-Based Bodies Using Optimized Rear Cavities." Journal of Fluids and Structures. https://doi.org/10.1016/j.jfluidstructs.2017.07.011.
[18] Sanmiguel, E., and M.-A. Alcantara. 2014. "Drag Reduction Induced by the Addition of a Multi-Cavity at the Base of a Bluff Body." Journal of Fluids and Structures. https://doi.org/10.1016/j.jfluidstructs.2014.03.013.
[19] Kavimandan, M., and B. Chandrasheker. 2020. "Aerothermodynamic Analysis of a Blunt Body with Forward-Facing Cavity and Opposing Jet Combination." International Journal of Engineering Research and Technology (IJERT).
[20] Saravanan, G., G. Jagadeesh, and K. P. J. Reddy. 2009. "Investigation of the Missile-Shaped Body with Forward-Facing Cavity at Mach 8." Journal of Spacecraft and Rockets 46: 577–591. https://doi.org/10.2514/1.38914.
[21] Sudarshan, S., and S. M. V. Rao. 2021. "Effect of the Axial Cavity with an Opposing High-Pressure Jet Combination in a Mach 6 Flow Condition." Acta Astronautica. https://doi.org/10.1016/j.actaastro.2020.09.021.
[22] Mohandas, S., and B. John. 2019. "Reduction of Wave Drag on Parameterized Blunt Bodies Using Spikes with Varied Tip Geometries." Acta Astronautica. https://doi.org/10.1016/j.actaastro.2019.04.017.
[23] Engblom, W. A., B. Yuceil, D. B. Goldstein, and D. S. Dolling. 1995. "Hypersonic Forward-Facing Cavity Flow: An Experimental and Numerical Study." AIAA Paper 95-0293. https://doi.org/10.2514/6.1995-293.
[24] Huang, W., and Z.-t. Zhao. 2017. "Parametric Study on the Drag and Heat Flux Reduction Mechanism of a Forward-Facing Cavity on a Blunt Body in Supersonic Flows." Aerosp. Science and Technology. https://doi.org/10.1016/j.ast.2017.10.017.
[25] Santos, W. F. N. 2007. "Simulation of Blunt Leading Edge Aerothermodynamics in Rarefied Hypersonic Flow." Journal of the Brazilian Society of Mechanical Sciences and Engineering 29 (2): 39–51. https://doi.org/10.1590/S1678-58782007000200001.
[26] Khan, S. A., Asadullah, M., Fharukh Ahmed, G.M., Jalaluddeen, Ahmed, Ali Baig, Maughal Ahmed. 2018. "Passive Control of Base Drag in Compressible Subsonic Flow Using Multiple Cavities." International Journal of Mechanical and Production Engineering Research and Development 8 (4): 39–4431.
[27] Khan, S. A., Asadullah, M., Sadiq, J. 2018. "Passive Control of Base Drag Employing Dimple in Subsonic Suddenly Expanded Flow." International Journal of Mechanical and Mechatronics Engineering 18 (3): 69–74.
[28] Sajali, M. F. M., Aabid, A., Khan, S. A., Mehaboobali, F. A. G., Sulaeman, E. 2019. "Numerical Investigation of the Flow Field of a Non-Circular Cylinder." CFD Letters 11 (5): 37–49.
[29] Khan, S. A., and E. Rathakrishnan. 2006. "Nozzle Expansion Level Effect on Suddenly Expanded Flow." International Journal of Turbo Jet Engines 23 (4): 233–257
[30] Khan, S. A., and E. Rathakrishnan. 2005. "Active Control of Suddenly Expanded Flow from Under-Expanded Nozzles—Part II." International Journal of Turbo Jet Engines 22 (3): 163–183. https://doi.org/10.1515/TJJ.2005.22.3.163.